IDO-17140

MASTER

# NUCLEAR TECHNOLOGY BRANCHES QUARTERLY REPORT

April 1 - June 30, 1965

PHILLIPS
PETROLEUM
COMPANY

PHILLIPS 66

ATOMIC ENERGY DIVISION

NATIONAL REACTOR TESTING STATION
US ATOMIC ENERGY COMMISSION

# DISCLAIMER

PRINTED IN USA. PRICE $2.00. AVAILABLE FROM THE CLEARINGHOUSE FOR FEDERAL
SCIENTIFIC AND TECHNICAL INFORMATION, NATIONAL BUREAU OF STANDARDS
U. S. DEPARTMENT OF COMMERCE, SPRINGFIELD, VIRGINIA

IDO-17140
AEC Research and Development Report
Reactor Technology
TID-4500
Issued: March 1966

# NUCLEAR TECHNOLOGY BRANCHES QUARTERLY REPORT

FORMERLY -- MATERIALS TESTING REACTOR-ENGINEERING TEST REACTOR TECHNICAL BRANCHES QUARTERLY REPORT

## APRIL 1 - JUNE 30, 1965

**D. R. deBoisblanc**
ASSISTANT MANAGER
ATOMIC ENERGY DIVISION

**W. C. Francis**
MANAGER,
REACTOR ENGINEERING

**R. G. Fluharty**
MANAGER,
NUCLEAR TECHNOLOGY

**M. E. Thomas**
MANAGER,
INSTRUMENT DEVELOPMENT &
TECHNICAL SERVICES

PHILLIPS
PETROLEUM
COMPANY

Atomic Energy Division
Contract AT(10-1)-205
Idaho Operations Office
U. S. ATOMIC ENERGY COMMISSION

## Previous Quarterly Reports in the MTR-ETR Series

| Quarter | Number | Quarter | Number |
|---|---|---|---|
| **1959** | | **1960** | |
| 1 | IDO-16543 | 1 | IDO-16633 |
| 2 | IDO-16561 | 2 | IDO-16648 |
| 3 | IDO-16580 | 3 | IDO-16658 |
| 4 | IDO-16620 | 4 | IDO-16665 |
| **1961** | | **1962** | |
| 1 | IDO-16695 | 1 | IDO-16781 |
| 2 | IDO-16710 | 2 | IDO-16805 |
| 3 | IDO-16733 | 3 | IDO-16827 |
| 4 | IDO-16760 | 4 | IDO-16857 |
| **1963** | | **1964** | |
| 1 | IDO-16898 | 1 | IDO-16994 |
| 2 | IDO-16917 | 2 | IDO-17042 |
| 3 | IDO-16932 | 3 | IDO-17052 |
| 4 | IDO-16977 | 4 | IDO-17081 |
| **1965** | | | |
| 1 | IDO-17104 | | |

# SUMMARY

Power, thermal flux, and fast flux distributions have been measured in the ATRC with shims in a configuration to give equal power generation in each of the five lobes. The void coefficient of reactivity in the fuel annulus is positive in coolant channel 20, zero in channel 19, and strongly negative in the center channels. The reactivity worth of outer shims in the ATRC was found to vary significantly with changes in flux trap composition. The shutdown worth of ATR hafnium safety rods is about 10$, which is at least 30 percent more than the worth of the ATRC cadmium safety rods.

A metallographic comparison between three identical $UO_2$-Al fuel plates, one as-fabricated, one heated out-of-pile for 45 days at 205°C, and a third one irradiated for 45 days at 205°C, showed that the fuel material in the plate heated out-of-pile did not react while the fuel in the irradiated plate was fully reacted.

By utilizing the electron microscope, evidence was found which indicated that $UAl_4$ retains fission gas within the lattice to a greater extent than does $UAl_3$, for a given burnup and irradiation temperature.

A special thermocouple assembly to allow fuel plate temperature measurements subsequent to operation in ETR is described.

Preliminary results are reported on the decay of Eu-148. Over one-hundred transitions have been identified as arising from this decay. On the basis of coincidence studies and energy and intensity determinations, approximately 50 percent of these transitions have been fit into a tentative decay scheme.

Investigations have been made of the operating characteristics of the electronic system used in the Ge(Li) spectrometers. Following a careful analysis of these characteristics, a procedure has been developed which will permit the measuring of gamma-ray energies with a precision, in most instances, of about 0.2 keV.

A description of the program for computation of potential radiological hazards is described herein.

A number of computer programs have been completed during the quarter. They include a program for cataloging all computer codes which are on file at the NRTS Computing Center, a number of personnel programs for use with the personnel master tape, an internal sort subroutine, and a program for analyzing data collected at the ETRC facility. This last program was written in a general fashion to facilitate its application to the analysis of general data.

# CONTENTS

## FIGURES

## TABLES

# I. REACTOR ENGINEERING

## 1. CRITICAL FACILITIES

### (E. E. Burdick)

1.1 Power and Flux Measurements in ATRC (J. L. Durney, J. W. Henscheid)

The shim configuration necessary to obtain a flat or so-called nominal 50-50-50 power distribution in the ATR has been determined in the ATRC. Since the experiment loading and shim pattern for these measurements provided quarter-core symmetry as illustrated in Figure I-1, power generation measurements were required in only one-fourth of the core. The figure shows the power generated in each fuel element of the core normalized to a total core power of 250 MW. This total power is generated in the five lobes (each lobe containing eight fuel elements as follows: 48.7 MW in both the NW and SE lobes, 51.0 MW in both the NE and SW lobes, and 50.6 MW in the center lobe. The maximum, or hot-spot, fission rate in this power distribution is 7.7 x $10^{14}$ fissions/g-sec (≈ 24 kW/g) and occurs in positions 19 and 39, the same positions in which the hot spots occur in the 40-50-60 power distribution

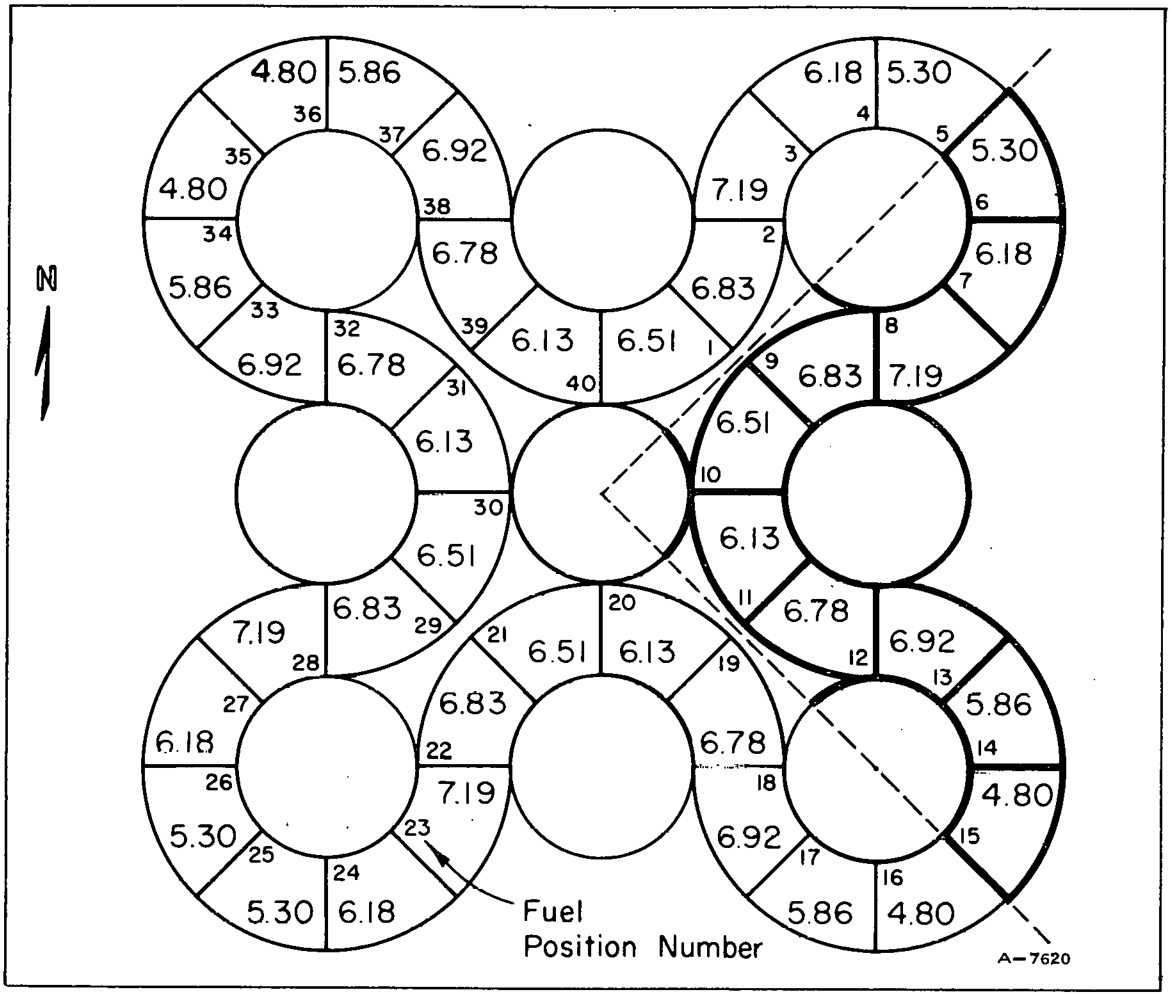

Fig. I 1 ATR power (in MW) generated in each element as determined from ATRC measurements. Values within bold lines are measured; others are inferred from symmetry.

[1]. The core used in measuring this 50-50-50 power distribution was the TURBO mock-up [2] with the exception of the fixed shims. The fixed shims were ATR H-hole hafnium sections in aluminum liners in H-holes 1, 5, 7, 9, 13, and 15. The neck shims were fully inserted, and the outer shims were withdrawn to 80.2 deg (N3-4, E1-2, S3-4, W1-2) and 85.2 deg (N1-2, E3-4, S1-2, W3-4). The difference in outer shim position was the result of a difference in flux trap experiment loading.

Several fission rate measurements and thermal neutron flux measurements were made in experimental positions using a shim configuration approximately the same as that described above. The results of these measurements are summarized in Tables I-1 and -2. The values in Table I-1 were obtained with one-quarter-inch U-Al wires in the center of an unfueled KAPL experiment mock-up. This mock-up was a train of KAPL aluminum spacers with aluminum strips to simulate fuel strips. The thermal neutron flux values listed in Table I-1 were obtained by applying a cadmium ratio correction and flux conversion factor to the activities obtained from the U-Al wires. Figure I-2 shows a typical vertical fission rate profile fitted in a least-squares fashion to a cosine function. The shape of the curve is typical of vertical profiles obtained in the ATRC.

TABLE I-1

FLUX TRAP FISSION RATES AT REACTOR RADIAL MIDPLANE
(Normalized to 50 MW Lobe Power)

| Flux Trap | Flux Trap Composition | Fission Rate ($10^{14}$ fission/g-sec) | Thermal Neutron Flux ($10^{14}$ n/cm$^2$-sec) |
|---|---|---|---|
| NE | Dummy flux trap filler, stainless steel retainer tube, and KAPL mock-up. | 5.39 | 3.31 |
| NE | Dummy flux trap filler, HF retainer tube, and KAPL mock-up. | 2.00 | 1.13 |
| NE | Dummy safety rod guide tube, HF retainer tube, and KAPL mock up. | 2.30 | 1.38 |
| NE | Dummy safety rod guide tube, stainless steel retainer tube, and KAPL mock-up. | 6.19 | 3.91 |
| East | Dummy flux trap filler, stainless steel retainer tube, and KAPL mock-up. | 5.98 | 3.73 |
| Center | SS retainer tube and KAPL mock-up. | 5.03 | 3.07 |

Table I-2 summarizes the neutron flux measurements made to date in the ATRC. It includes previously reported fast flux values [3] measured in a 40-50-60 power split [1], thermal flux values obtained in the 50-50-50 power split described above, and, for comparison, thermal flux values from the TURBO calculations for a 40-50-60 power split[4]. Differences between the measured and calculated

## TABLE I-2

### REACTOR MIDPLANE NEUTRON FLUX NORMALIZED TO 250 MW ($10^{14}$ n/cm$^2$-sec)

| Reactor Position | Experiment Composition | TURBO Calculated | ATRC Measured | |
|---|---|---|---|---|
| | | $\phi_{th}$ (2200 m/sec) | $\phi_{th}$[a] (2200 m/sec) | $\phi > 1$ MeV |
| I-19 | Al filler | 0.73 | 0.59 | ---- |
| I-20 | Al filler | 0.59 | 0.78 | ---- |
| I-1 | Al filler | 0.96 | 1.65 | ---- |
| I-2 | Al filler | 0.75 | 0.84 | ---- |
| I-3 | Al filler | 0.78 | 0.64 | ---- |
| A-1 | SS filler | 2.90 | ---- | 3.50 |
| A-8 | SS filler | 2.90 | ---- | 3.60 |
| A-9 | SS filler | 3.10 | 2.79 | 3.70 |
| A-12 | SS filler | 4.30 | ---- | 4.10 |
| B-1 | SS filler | 6.40 | 4.81 | 1.80 |
| B-8 | SS filler | 6.40 | 4.84 | 2.50 |
| H-2 | Water | 4.60 | 4.16 | 3.20 |
| H-15 | Water | 5.30 | ---- | 3.50 |
| H-16 | Water | 4.70 | ---- | 2.90 |

---

[a] These values were obtained in a core having nearly a 50-50-50 power split. All others were obtained in the 40-50-60 power split.

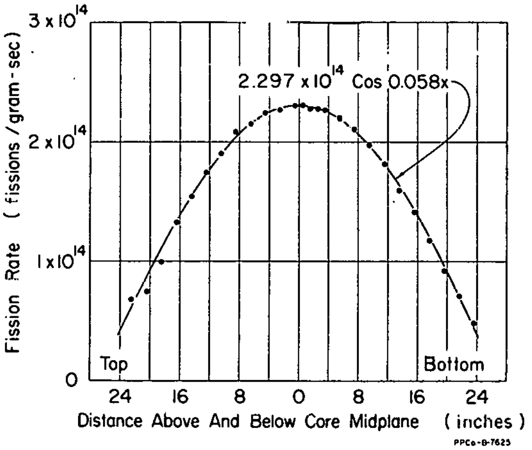

Fig. I-2 Vertical fission-rate profile for the NE flux trap in ATRC normalized to 50 MW lobe power. The flux trap contains the guide tube mock-up, hafnium retainer tube, and KAPL unfueled experiment mock-up.

values are attributed primarily to nuclear differences between the experimental and calculational models and only partially to the difference in core power distributions.

During normal operation of the ATR and ATRC, the lower ends of the safety rod neutron absorber plates (four on each safety rod which are cadmium in the ATRC and hafnium in the ATR) extend three inches into the reactor core. The effect of this poison on the fission rate in a flux trap containing a safety rod has been determined by measuring the fission rate in two flux traps that differed only by the presence of the ends of these absorber plates.

Figure I-3 is a comparison of the vertical fission rate profiles in a flux trap with a safety rod and in one without a safety rod. The difference in the fission rates for these two flux traps is about 35 percent at the core top, but it is only 14 percent at a distance of four inches into the active core and is negligible at nine inches. The difference between the perturbations caused by cadmium and hafnium is not expected to be significant. The measurement was made with two identical unfueled KAPL experiment mock-ups in the flux traps. The shim configuration was nearly that described above for the 50-50-50 power distribution.

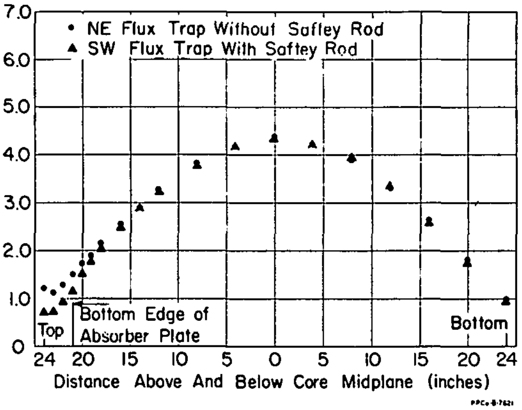

Fig. I-3 Vertical fission rate profiles in ATRC flux traps showing the perturbation caused by the poison plates of a safety rod.

## 1.2 ATRC Fuel Annulus Void Coefficients of Reactivity (N. C. Kaufman)

The reactivity effect of localized void formation within the ATRC fuel annulus has been measured. Teflon strips running the full vertical length of the fuel elements were used to simulate voids, and the resulting reactivity changes were measured under two shim configurations: (a) that necessary for an ATR 40-50-60 MW power split and (b) that necessary for an ATR 50-50-50 MW power split. The measured values in each of these shim configurations have been converted to void coefficients, and the results are depicted in Figure I-4. Also shown in this figure are values obtained by Babcock and Wilcox in the ATR Critical Experiment [5].

The following results verify the general trends observed in the ATR Critical Experiment: a positive void coefficient in channel 20, an essentially zero void coefficient in channel 19, and a strongly negative void coefficient at the radial center of the fuel element. The increased fuel loading from the 26 kg core used in the ATR Critical Experiment to the present 35 kg core evidently produced a slightly smaller average void coefficient. Changing from a 40-50-60 MW to a 50-50-50 MW power split apparently produces the same effect. It was also observed experimentally that although nearly zero, the void coefficient changes from positive to negative moving azimuthally in the channel from the side plate toward the center of the element.

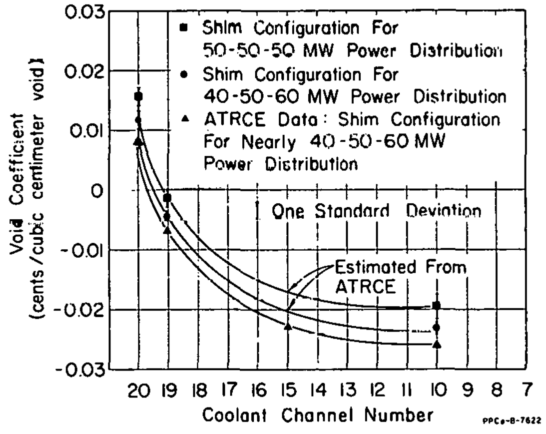

Fig. I-4 Void coefficients of reactivity in ATRC hot-spot fuel elements.

Prior to making these measurements, an experiment was done to assess the degree to which Teflon would simulate air. A bundle of Teflon strips was removed from the in-core portion of an air-filled tube located in an inner flux trap with a flux trap filler when the reactor was just critical. A reactivity change of -0.93 x $10^{-6}$ dollars per cubic centimeter of Teflon was deduced from the resulting negative period. This corresponds to a 3.5 percent increase in the previously measured air-void coefficient in this position and implies that 1.0

cubic centimeter of Teflon is equivalent to 1.035 cubic centimeters of air. Although the neutron density and spectrum within the fuel annulus will be different from that in this flux trap, it was felt that this measured relationship will not change significantly in the fuel annulus. Consequently, it was used to provide a slight correction to the measured values in calculating the values shown in Figure I-4.

The technique used to obtain these data was to load Teflon strips into the elements and to deduce the subsequent reactivity change from the change in critical shim positions relative to those for the core with no strips added. Two strips were placed edge to edge in the desired channel in each of four fuel elements. These four elements were in all cases the hot-spot elements in a 40-50-60 MW power split. The two strips in each element were positioned in the channel as near to the hot-spot as possible.

### 1.3 Interaction Between Outer Shims and Inner Flux Trap in ATRC (N.C. Kaufman)

While measuring the reactivity effects due to voiding an inner flux trap of the ATRC, it became apparent that the worth of the outer shims nearest a particular flux trap was strongly dependent on the composition in that trap. Accordingly, a series of measurements was made in which the total worth of an outer shim pair as a function of the flux trap annulus metal-to-water ratio and of the U-235 content of the flow tube in the adjacent inner flux trap was determined. The results of these measurements are shown in Figure I-5 with three fuel concentrations for each of three flux trap annulus metal-to-water ratios.

These results indicated significant interaction between the outer shims and the composition of the adjacent inner flux trap. The interaction was found to be greater for metal-to-water ratio variations than for fuel variations. These results imply that an ATR shim withdrawal program may need to be altered between cycles if large changes are made in the flux trap compositions during shutdown.

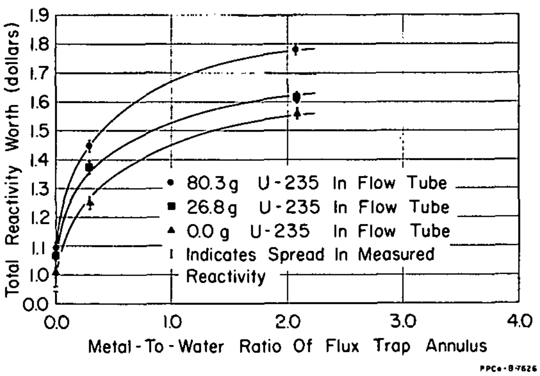

Fig. I-5 Total worth of a single outer shim pair in ATRC versus adjacent inner flux trap composition.

A detailed integral worth calibration curve was constructed for an outer shim pair from a series of period measurements for three compositions representing the extremes of the fuel and metal-to-water ratios examined. These three compositions were:

(1) Annulus metal-to-water ratios of 0.0 and 0.0 g U-235 in the flow tube

(2) Annulus metal-to-water ratios of 2.1 and 0.0 g U-235 in the flow tube

(3) Annulus metal-to-water ratios of 2.1 and 80.3 g U-235 in the flow tube.

When all three calibrations curves were normalized to the same total worth, it was found that they coincided. That is, there was no shape change evident due to composition changes in the flux trap. The resulting curve, normalized to 1.0 at maximum worth, is shown in Figure I-6.

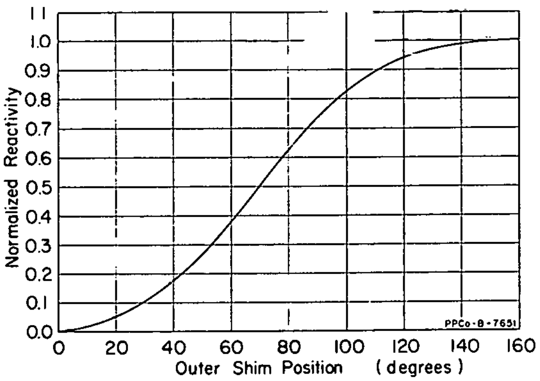

Fig. I-6 Normalized calibration curve for an outer shim pair with the 18 outermost neck shims out and all other neck shims and outer shims inserted.

An additional result of these measurements was the comparison of the worth of a ganged set of two adjacent outer shim pairs with the sum of their individual worths. The individual worth in each case was measured with the adjacent outer shim pair fully inserted. The resulting curves are shown in Figure I-7. The fact that the worth of the ganged set is greater than the sum of the individual worths is consistent with the idea of rod shadowing. That is, the worth of an individual outer shim pair is depressed by the presence of a fully inserted adjacent outer shim pair.

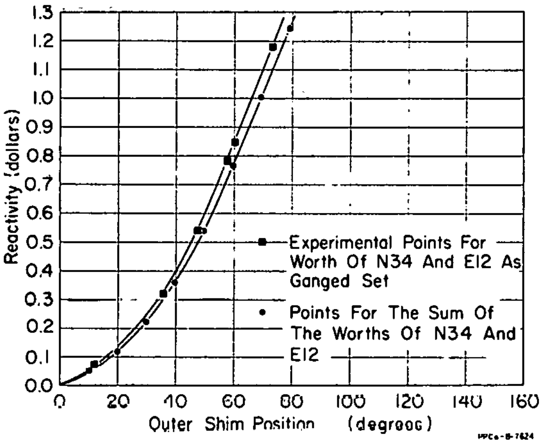

Fig. I-7 Integral worth of the outer shims around the NE flux trap with the 18 outermost neck shims out and all other neck shims and outer shims inserted.

## 1.4 ATR-ATRC Safety Rod Worths

(W. L. Schrader, J. W. Henscheid)

Measurements were made in the ATRC to predict the shutdown margin in the ATR safety rods and to investigate the effects of flux trap changes on the worths of ATR and ATRC safety rods. The ATR hafnium safety rods were found to be 30 to 40 percent more effective than the ATRC cadmium safety rods. Earlier measurements in the ATR Critical Experiment indicated that a hafnium safety rod was worth as much as 24 percent more than a cadmium safety rod [6].

The worth of the ATR safety rods is estimated to be 10$ in a nominal 50-50-50 power distribution and 11$ in a nominal 40-50-60 power distribution. Corresponding safety rod worths in the ATRC are 7.6 and 8.4$, respectively. These values are for water in the flux trap flow tube and with flux trap fillers on three of the five safety rods. Previous measurements with TURBO mock-up experiments in the flux traps indicated that the ATRC safety rod worths were 9.1 and 10.0$, respectively [7].

Flux trap changes also affect the safety rod worths since the flux trap composition alters the neutron spectrum in the immediate vicinity of the safety rods. The most significant effects noted were as follows:

(1) The worth of a safety rod increases as the fuel content of the experiment in the flux trap increases; the rate is approximately 0.22 percent of rod worth per gram of U-235.

(2) When a typical hafnium shroud is added to a fueled experiment, the safety rod worth in that flux trap decreases to the worth of a safety rod in a flux trap without a fueled experiment.

(3) A safety rod without a flux trap filler attached is worth about 25 percent less than a rod with a filler.

(4) A safety rod in an outer flux trap is worth about 10 percent more than a rod in an inner flux trap. Earlier measurements in the ATR Critical Experiment indicated about 26 percent more [6].

All measurements were made in the 35-kg ATRC core containing TURBO mock-up experiments except when a typical KAPL experiment mock-up [a] was inserted in the flux trap of interest. All neck shims were inserted, and all outer shims were balanced between 80 and 105 deg. The safety rod worths were deduced from critical positions of the ganged outer shims, and calibration curves were obtained from asymptotic period measurements.

## 2. MATERIALS RESEARCH

(J. M. Beeston)

### 2.1 Relative Fission Gas Behavior In $UAl_3$ and $UAl_4$ (R. A. Moen)

Recent studies with the electron microscope have indicated that gas bubbles form in $UAl_3$ to a greater extent than in the surrounding $UAl_4$. This phenomenon was noted on specimens from two plates fabricated of 50 weight percent $UAl_3$ dispersed in aluminum and irradiated to 60 percent burnup in lattice position L-51 of the MTR. The absence of visible agglomerates of gas in the $UAl_4$ may be due to its defect structure.

The uranium-aluminum intermetallic compound, $UAl_4$, has been studied extensively and found to contain a lattice defect structure containing from 64.2 to 66.3 percent uranium by weight [8]. It was postulated that the $UAl_4$ structure either contained some uranium sites which were vacant or contained aluminum atoms.

A cross section of one of the irradiated fuel plates is shown first in the as-polished condition and second in the as-etched condition (Figures I-8 and -9, respectively). The etchant used was a solution of 80 parts water, 20 parts nitric acid, and 1 part hydrofluoric acid. This etchant is a standard etchant used to delineate the phase boundary between $UAl_3$ and $UAl_4$. Since the fuel particles were fabricated as $UAl_3$, the outer peripheral zone of the irradiated particle would be expected to be the reaction product, $UAl_4$, resulting from the $UAl_3$ plus aluminum solid-solid reaction.

---

[a] The KAPL experiment mock-up contained 90 g U-235 in plates held in aluminum holders. The tubular hafnium shroud extended the entire height of the core and was used in place of the stainless steel retainer tube.

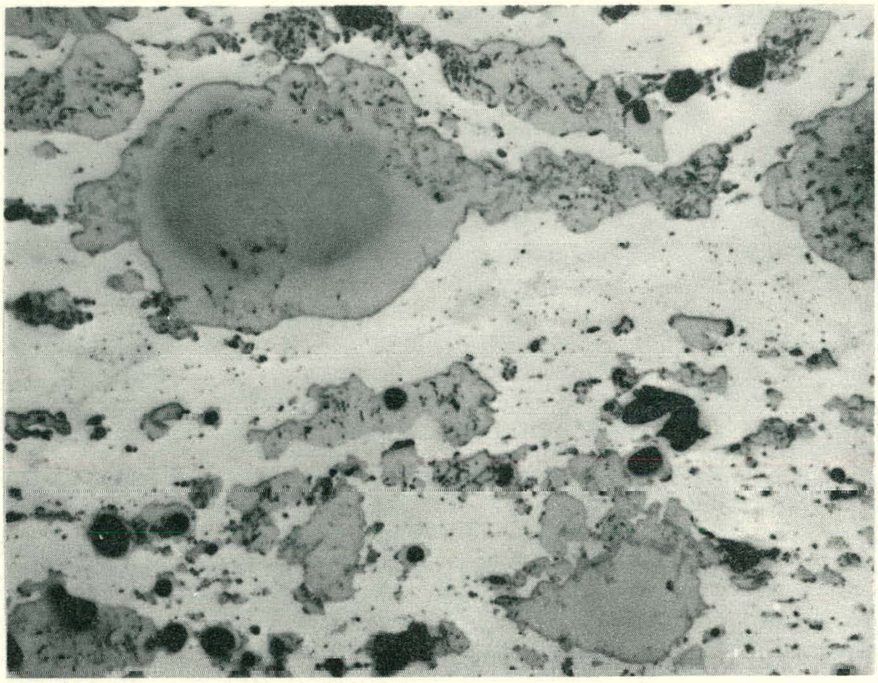

Fig. I-8 Polished cross-section as-polished of 50 wt% of $UAl_3$-Al fuel plates.

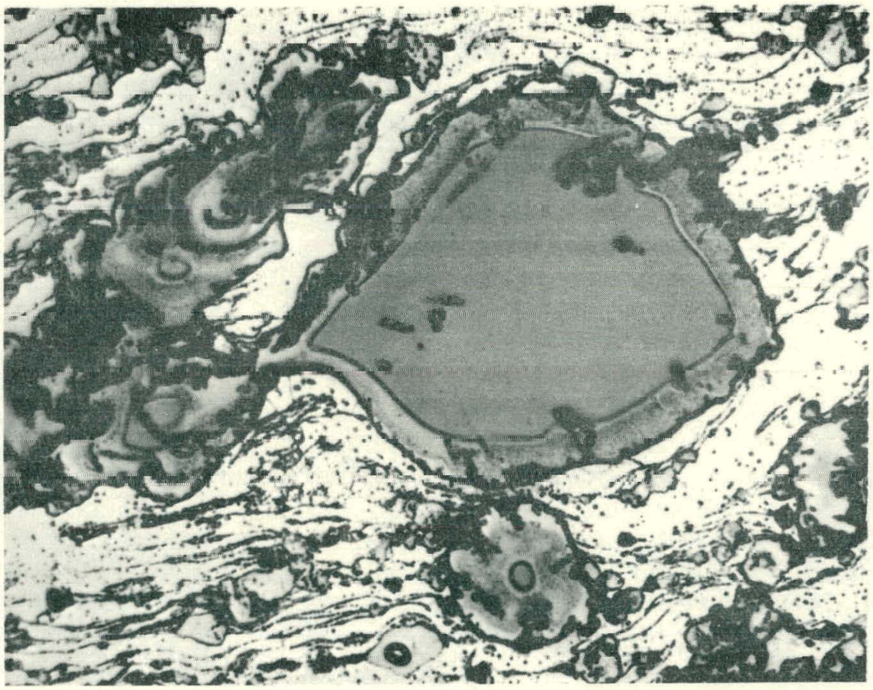

Fig. I-9 Polished cross-section as-etched of 50 wt% of $UAl_3$-Al fuel plates.

Replicas of the polished surfaces of the irradiated samples were made by applying cellulose acetate softened with acetone on the surface previously wet with a cellulose acetate-acetone mixture. The surface replicas were then shadowed with paladium and coated with a film of carbon. The film was scored, and the cellulose acetate dissolved away. The small sections of films were washed in acetone and caught on microscope screens preparatory to microscopic examination.

Examination of the replicas in the electron microscope indicated the same two-phase structure as observed with a light microscope. However, the center portion of the partially reacted particles stood out in relief and contained gas bubbles. Gas bubbles could not be detected in the reacted particles. Figure I-10 shows the partially reacted $UAl_3$ particles, and fully reacted particles are shown in Figure I-11.

Electron microscope examinations of other $UAl_3$ and $UAl_4$ particle replicas from fuel plates irradiated to lower burnups (≈20 percent) show a lesser amount of $UAl_3$ relief, and there is no indication of any fission gas agglomeration in the $UAl_3$.

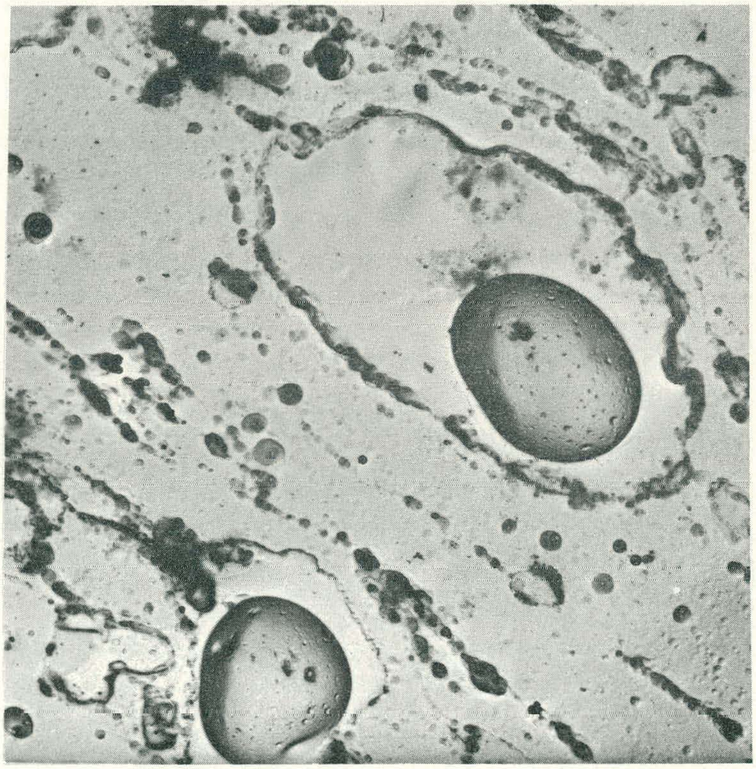

Fig. I-10 Partially reacted $UAl_3$ fuel particles.

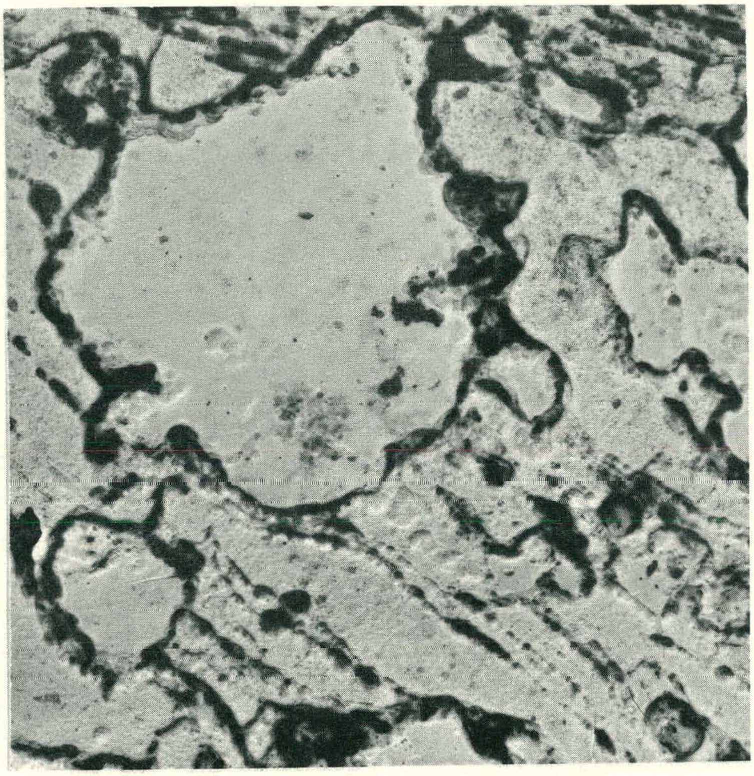

Fig. I-11 Fully reacted fuel particles, now $UAl_4$.

## 2.2 Low-Temperature Reaction Between Uranium Dioxide and Aluminum

Previous post-irradiation examination indicated complete reaction between $UO_2$ and aluminum in-pile at 205°C [9]. An identical fuel plate was held at 205°C out-of-pile for the same length of time (45 days) and then examined on the electron microprobe for evidence of a fuel particle-matrix reaction. Figures I-12, -13, and -14 are included to show the identical fuel plate composition, as-fabricated, heated at 205°C out-of-pile for 45 days, and in-pile at 205°C for 45 days, respectively. No evidence of reaction was found in the fuel plate heated out-of-pile, once more verifying the role of neutron flux on in-pile, solid-solid reactions.

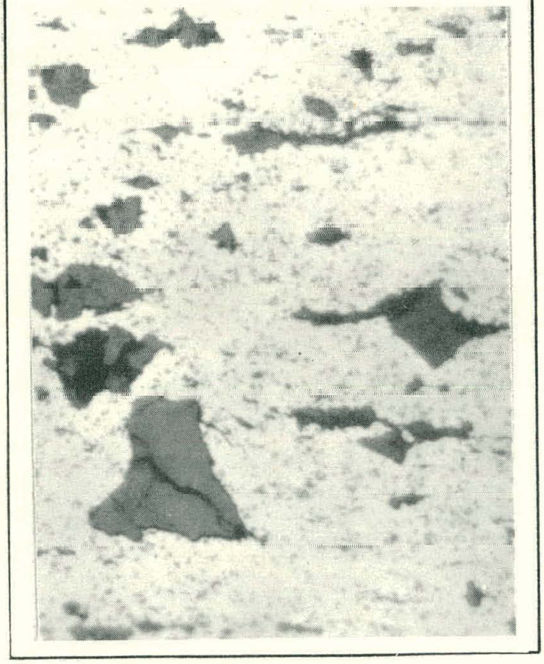

Fig. I-12 $UO_2$ + Al as-fabricated.

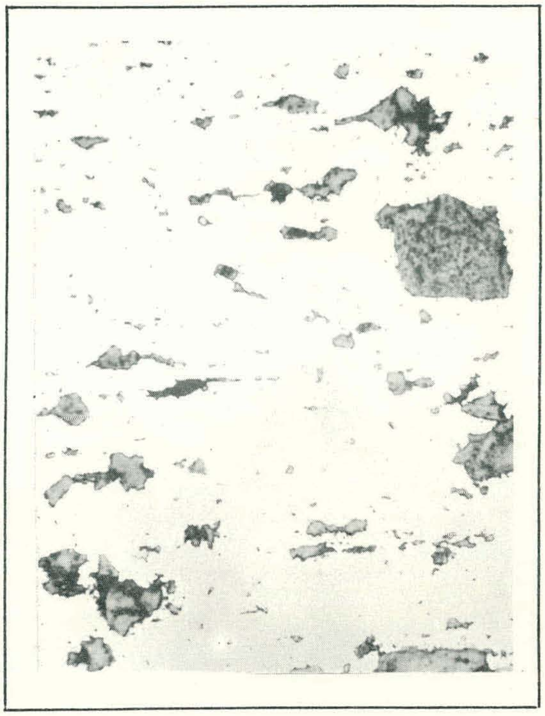

Fig. I-13 $UO_2$ + Al heated 45 days at 205°C out-of-pile.

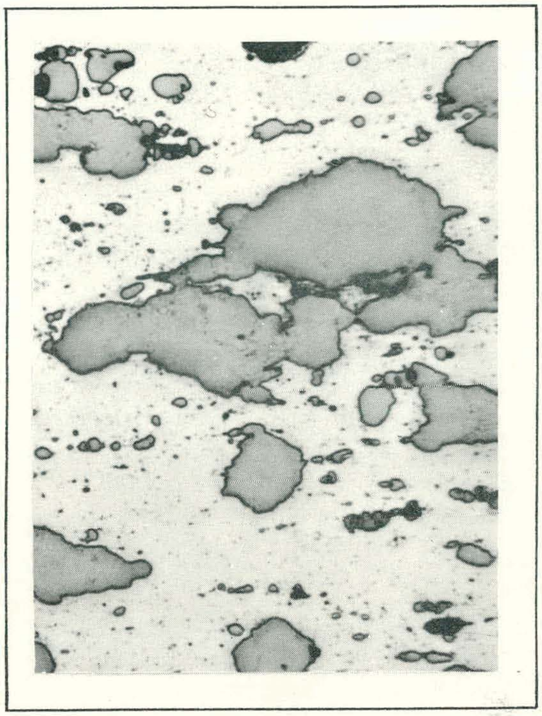

Fig. I-14 $UO_2$ + Al Irradiated 45 days at 205°C.

## 3. ENGINEERING EXPERIMENTS

(V. A. Walker)

ATR Fuel and Materials Development (E. H. Porter)

An experiment is planned to obtain verification of calculations predicting the maximum plate surface temperature with an ETR fuel element in an underwater horizontal position. The results will be extended to ATR fuel element conditions in conjunction with the development of the operating conditions for ATR.

The TC hot junctions were designed and fabricated using Kovar metal/glass junctions, and the leads will permit 90 deg reorientation of the hot-junction harness assembly as the element is moved from a vertical to a horizontal position.

The TC assembly and hot-junction detail are shown in Figures I-15 and -16.

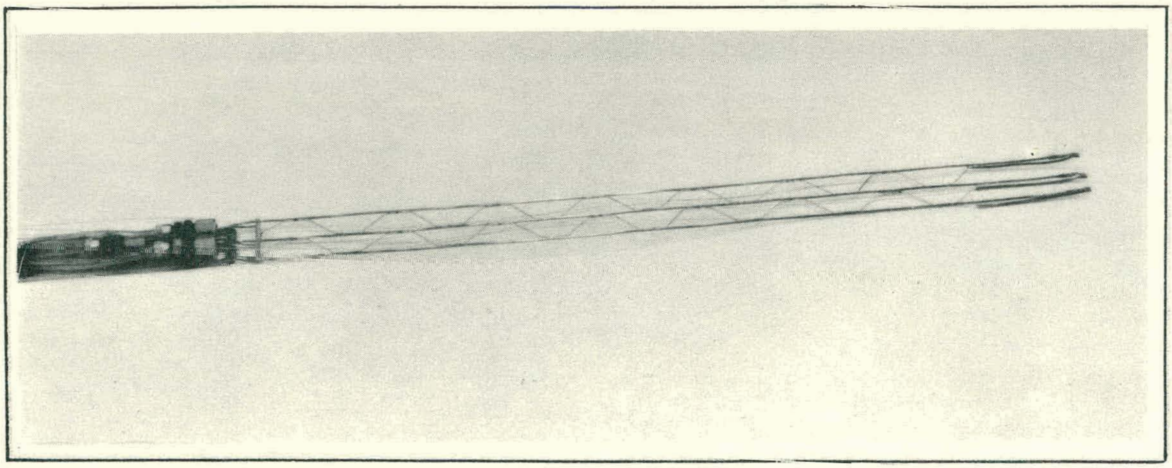

Fig. I-15 Lower TC harness assembly.

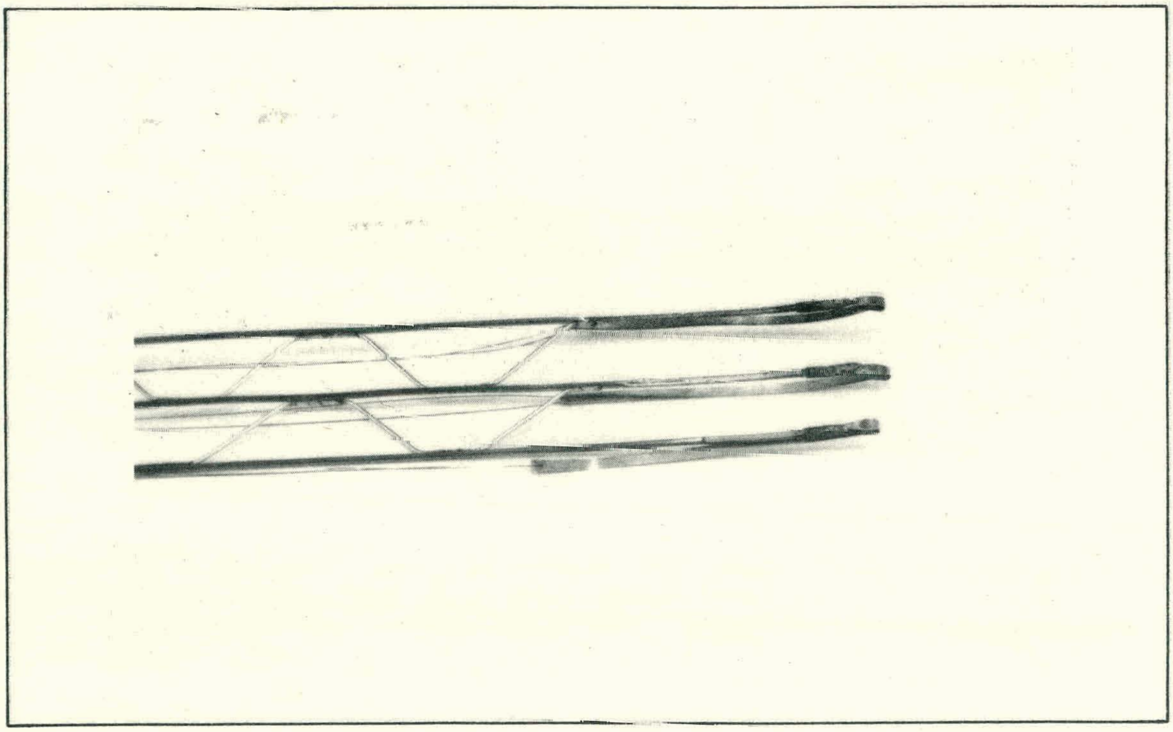

Fig. I-16 Hot-junction detail.

## 4. REFERENCES

1. L. C. Richardson and J. W. Henscheid, "ATR Power Calibration", Nuclear Technology Branches Quarterly Report, October 1 - December 31, 1964, IDO-17081 (1964) pp 2-5.

2. N. C. Kaufman and J. W. Henscheid, "Reactivity Measurements in the ATRC", Nuclear Technology Branches Quarterly Report, October 1 - December 31, 1964, IDO-17081 (1964) p 1.

3. J. L. Durney, "Fast Neutron Flux in the ATRC", Nuclear Technology Branches Quarterly Report, January 1 - March 31, 1965, IDO-17104.

4. R. A. Turner, Advanced Test Reactor Turbo Report, IDO-24459 (January 1964).

5. A. L. MacKinney et al, Advanced Test Reactor Critical Experiments Final Report, TID-19421 Section 7 (August 1963).

6. A. L. MacKinney et al, Advanced Test Reactor Critical Experiments Final Report, TID-19421 Section 5 (August 1963).

7. W. L. Schrader and J. L. Durney, "ATRC Safety Rod Calibrations", Nuclear Technology Branches Quarterly Report, October 1 - December 31, 1964, IDO-17081 (1964) pp 10-11.

8. B. S. Borie, Jr., Journals of Metals, 3 (September 1951) p 800.

9. W. F. Zelezny, "Microprobe Investigation of Irradiated and Unirradiated Fuel Materials", Nuclear Technology Branches Quarterly Report, January 1 - March 31, 1965, IDO-17104.

# II. NUCLEAR TECHNOLOGY

## 1. INELASTIC SCATTERING

(R. M. Brugger)

### 1.1 Liquid and Solid Argon (P. D. Randolph)

Analysis of the slow-neutron inelastic scattering data taken for argon, just below and just above the melting point, has been completed, and the scattering law has been obtained over a wide region of energy and momentum transfer. Momentum dependent structure at fixed energy transfer has been observed in the scattering law for both the liquid and solid states. Similar structure has been observed in powdered aluminum [1], powdered beryllium [2], and liquid sodium [3]. A measurement of the frequency spectrum of normal modes of vibration has been made for the solid argon sample. The result is shown in Figure II-1. In this figure, the Debye frequency spectrum and one based on a Born - von Karman model are compared with the spectrum obtained from the experiment. The experimental spectrum has a shape roughly similar to the Born - von Karman shape though the high-energy peak lies at a slightly lower energy. It has more low-frequency contributions than either of the models and less higher frequency contributions.

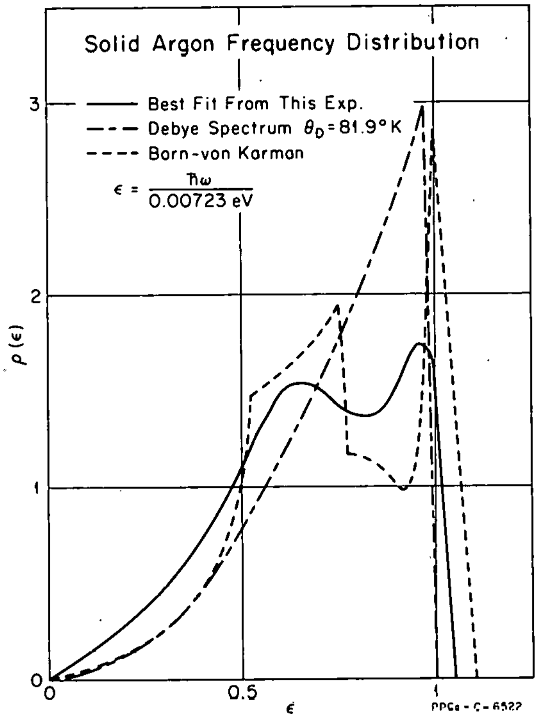

Fig. II-1 Various frequency spectra assumed for solid argonne. The solid curve gives the best overall fit.

A more complete report on this experiment is given in U. S. Atomic Energy Commission Report, IDO-17089, May 1965.

### 1.2 Liquid Lead (P. D. Randolph)

An experiment to measure the inelastic scattering from liquid lead at 350°C was completed during this quarter. The actual data results were made during three weeks of reactor operation at the HT-1 north beam hole. Due to the higher flux at this new source-beam hole, a large amount of data of very good quality was obtained even though the total running time was relatively short. These data have all been processed to scattering law and the plotting of the results by machine is largely completed. Further analysis and interpretation of the results are being done at Argonne National Laboratory during the summer in collaboration with K. S. Singwi of that laboratory.

Two innovations were made in this experiment. First, due to the high flux at HT-1 north, narrower detector banks were used which resulted in a much improved angular resolution and, therefore, an improved resolution in momentum transfer. At an incident energy of 0.02 eV, the spread in momentum transfer ($\hbar\kappa$) is given by $\Delta\kappa \approx \pm 0.05$ Å-1. This is in contrast to previous scattering law measurements where $\Delta K \approx \pm 0.2$ Å-1 or more. Secondly, a helium flight path was used to reduce the scattering of the incident beam from the air in the region just before and just after the sample. Helium, having a lower cross section than air, contributes less background scattering. This helium flight path not only enclosed the sample and the major portion of the forward beam, but also extended all the way out to the detectors covering the angular region from 15 to 90 deg.

The experiment was done at incident energies of 0.015, 0.017, and 0.020 eV on two samples having different thicknesses, the thicker being a 15 percent scatterer and the other being a 10 percent scatterer. Also, a run at 0.04 eV was taken on the thinner sample. To observe the improvement due to helium in the flight path, a comparison run at 0.02 eV was taken with air in the flight path. The results show that for scattering angles less than 40 deg, the effects of air scattering are quite large. This shows up very clearly in the scattering law. At a fixed energy transfer, the air scattering depresses the scattering law at small momentum transfer, the effect decreasing with increasing momentum transfer. Above $K \approx 2 - 2.5$ Å-1, air scattering had very little effect. Figure II-2 shows the qualitative effect of air compared to helium. This figure shows the raw data for the same angle of scattering (25 deg) and of the same incident energy (0.02 eV) for liquid lead at 350°C where Figure II-2(a) was obtained with air in the flight path and Figure II-2(b) with He. Note that the vertical scales are different. Also, the running times are different, 1870 minutes for the He-filled flight path and 1450 minutes for the air-filled case. The data points are taken with the sample in place, and the continuous curves represent the data with the empty sample holder in the beam. The air gives an effective broadening of the empty holder scattering and tends to obscure the inelastic scattering. The low broad humps in the data seen at around 3 Å and at 4 Å are due to the two rotating collimators, which open twice per revolution. The humps arise from the second or 180 deg opening of each collimator, allowing neutrons to scatter from the choppers which open only once per revolution.

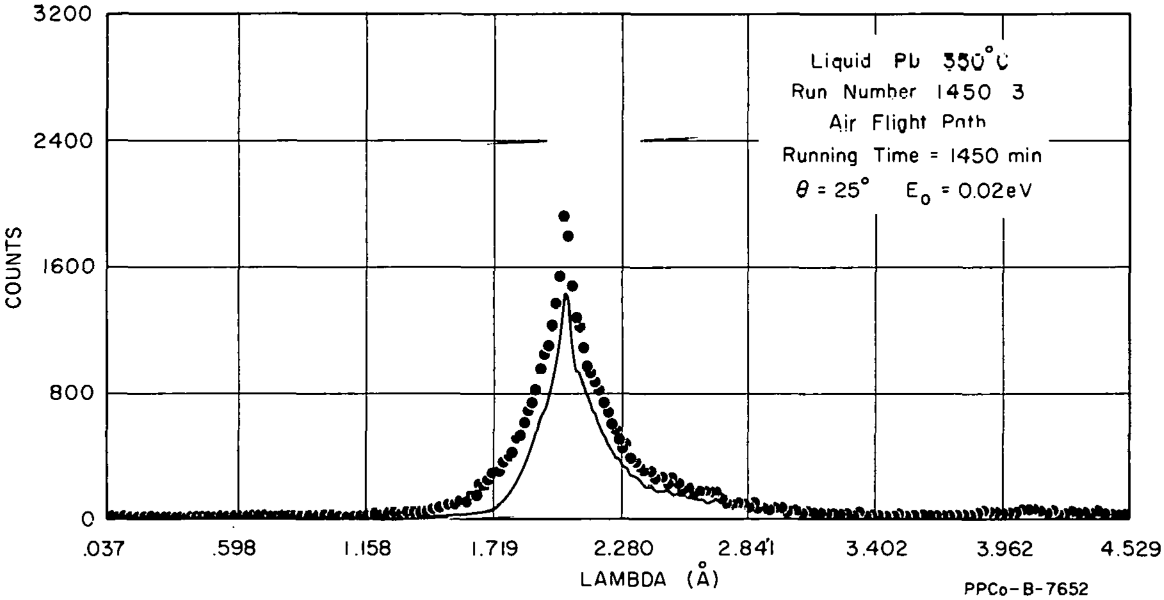

Fig. II-2(a) Comparison of the effect of air and helium in the flight path of the incident and scattered neutrons. The points are for the sample in the beam, and the solid curve with the empty sample holder in the beam. Note the scale and time change between the two figures.

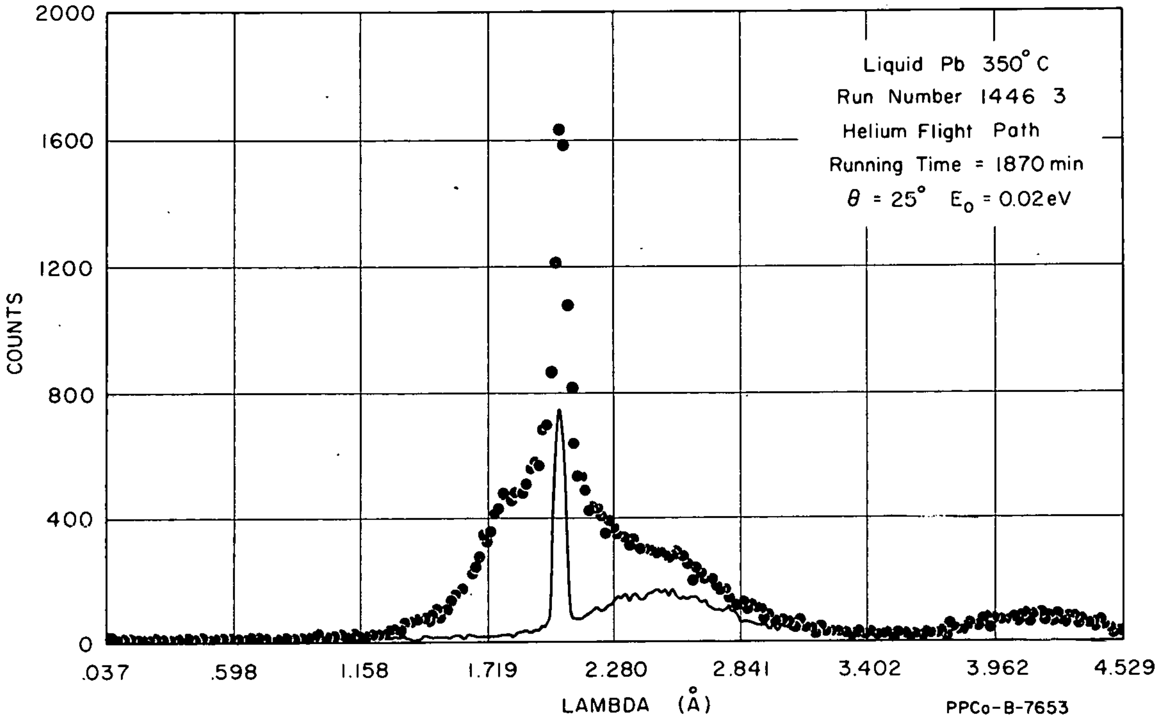

Fig. II-2(b) Comparison of the effect of air and helium in the flight path of the incident and scattered neutrons. The points are for the sample in the beam, and the solid curve with the empty sample holder in the beam. Note the scale and time change between the two figures.

### 1.3 Beryllium (R. E. Schmunk)

Renewed interest in the dispersion relation of beryllium arose because of recent comparisons [4] which were made with data for magnesium and zinc and also from recent work on lattice dynamics models. The dispersion relation of beryllium is of interest through the information it conveys on solid state physics and the application of this information to the problem of neutron moderation. Given a lattice dynamics model which accurately describes the dispersion relation data, one should be able to apply the model to the calculation of neutron scattering from polycrystalline beryllium. For these reasons, the dispersion relation data for beryllium were extended during the third quarter.

The dispersion relation data for beryllium for phonon propagation in the crystallographic directions [0001], $[01\bar{1}0]$, and $[1\bar{1}20]$ are displayed in Figure II-3. The relation is completely mapped for the first two directions, but is only partially mapped for $[11\bar{2}0]$ where the phonon polarizations are not pure. All data points for the $[11\bar{2}0]$ direction and those data points for the $[0\bar{1}10]$ direction which are plotted as circles were obtained recently. It is of interest that the branches for the $[0\bar{1}10]$ direction which were measured recently (transverse optical and acoustical with phonon polarization parallel to the basal plane) are nearly degenerate with other branches which were measured previously. This near degeneracy is not predicted from the symmetry of the structure, but is a result of the force field in the crystal which is peculiar to beryllium.

All dynamical models which have developed for the hexagonal close-packed structure follow the Born - von Karman formalism with varying assumptions regarding the interatomic forces. The models and the accompanying assumptions are the following:

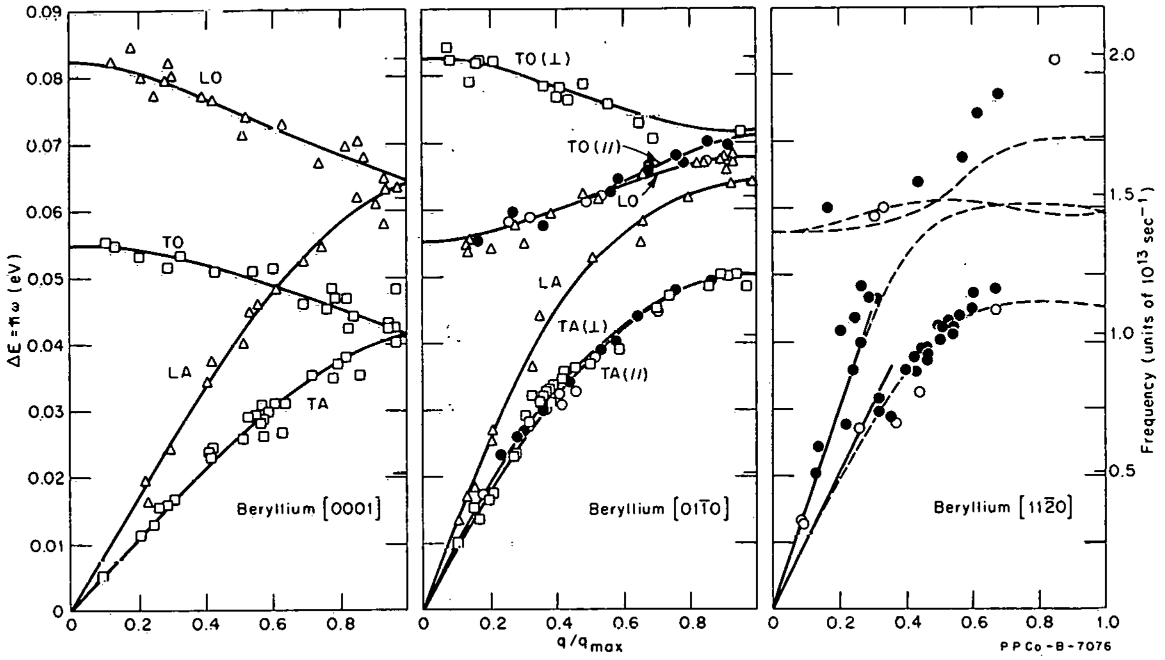

Fig. II-3 Phonon dispersion relation for beryllium determined by neutron inelastic scattering. Data obtained recently are plotted as circles, solid points for neutron energy gain and open points for neutron energy loss. The smooth curves represent the experimenter's interpretation of the data.

(1) Begbie and Born model assuming general tensor forces with interactions out to fourth nearest neighbors [5]

(2) The model of DeWames, Lehman, and Wolfram [6] which assumes bond stretching and bond bending interactions out to sixth nearest neighbors

(3) The central force model of Slutsky and Garland which has been extended [7] to include interactions out to fifth nearest neighbors

(4) The model of Gupta and Dayal [8] which adds the contribution of the electron gas to the extended Slutsky-Garland model.

As one might expect, appropriate relations exist which relate the force constants of one model to those of another model. These models are compared with the experimental data for the [0001] and [0110] directions in Figures II-4 through -7 in which the predictions of the models are shown as the dotted lines, and the solid lines represent the data. The model of DeWames et al gives a slightly better fit to the data than the other models. The model of Gupta and Dayal does not appear to have improved on the extended Slutsky-Garland model at all. To obtain much improvement between the predictions of the models and the experimental data would require a model which is physically more realistic, ie, one which accurately accounts for the effects of the conduction electrons in the solid.

Even with the small discrepancies which exist between the models and the scattering law data, it should be possible to calculate the inelastic scattering from polycrystalline beryllium. The largest discrepancies would be expected

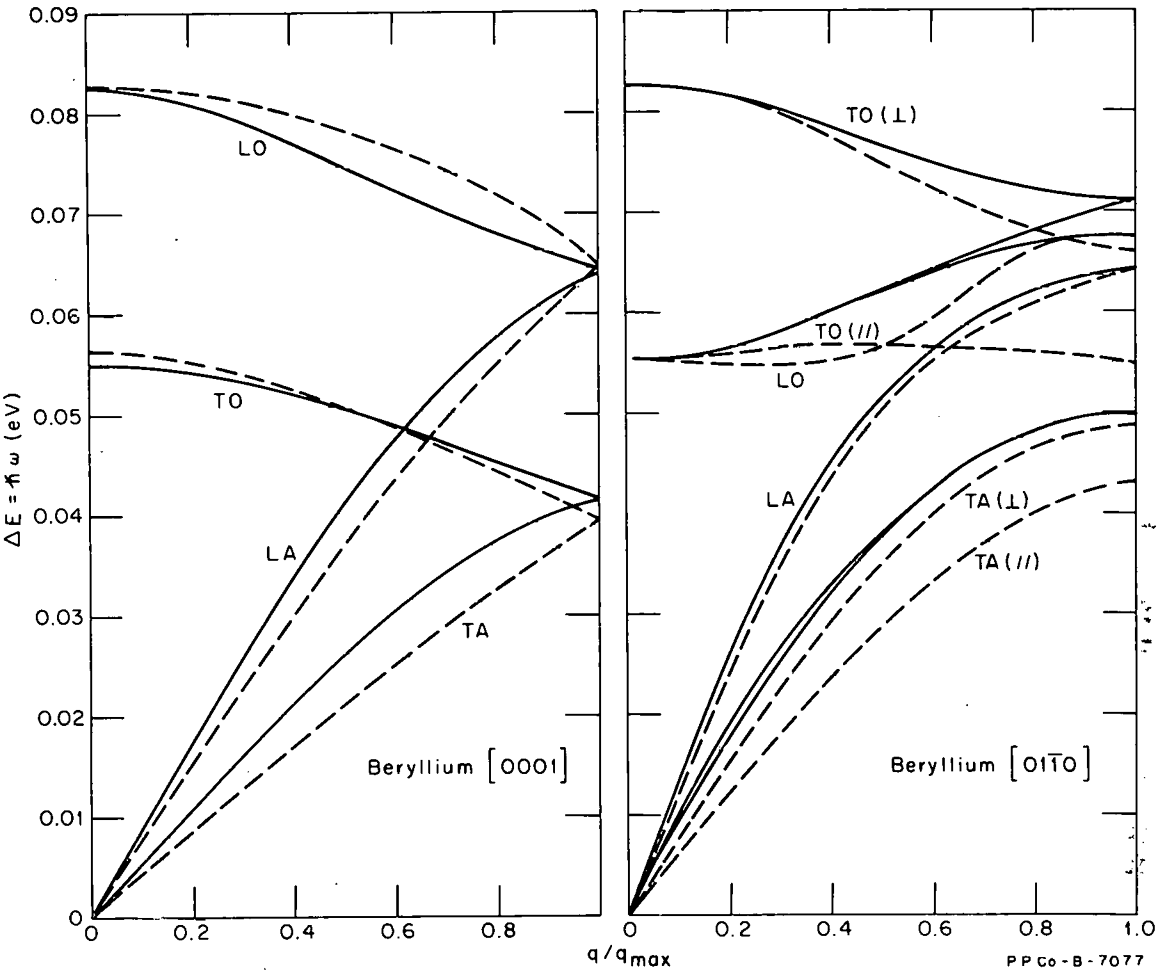

Fig. II-4 Comparison of the model of Slutsky and Garland, extended to fifth nearest neighbors and identified by the dashed lines, with the experimental data which are represented by the solid lines.

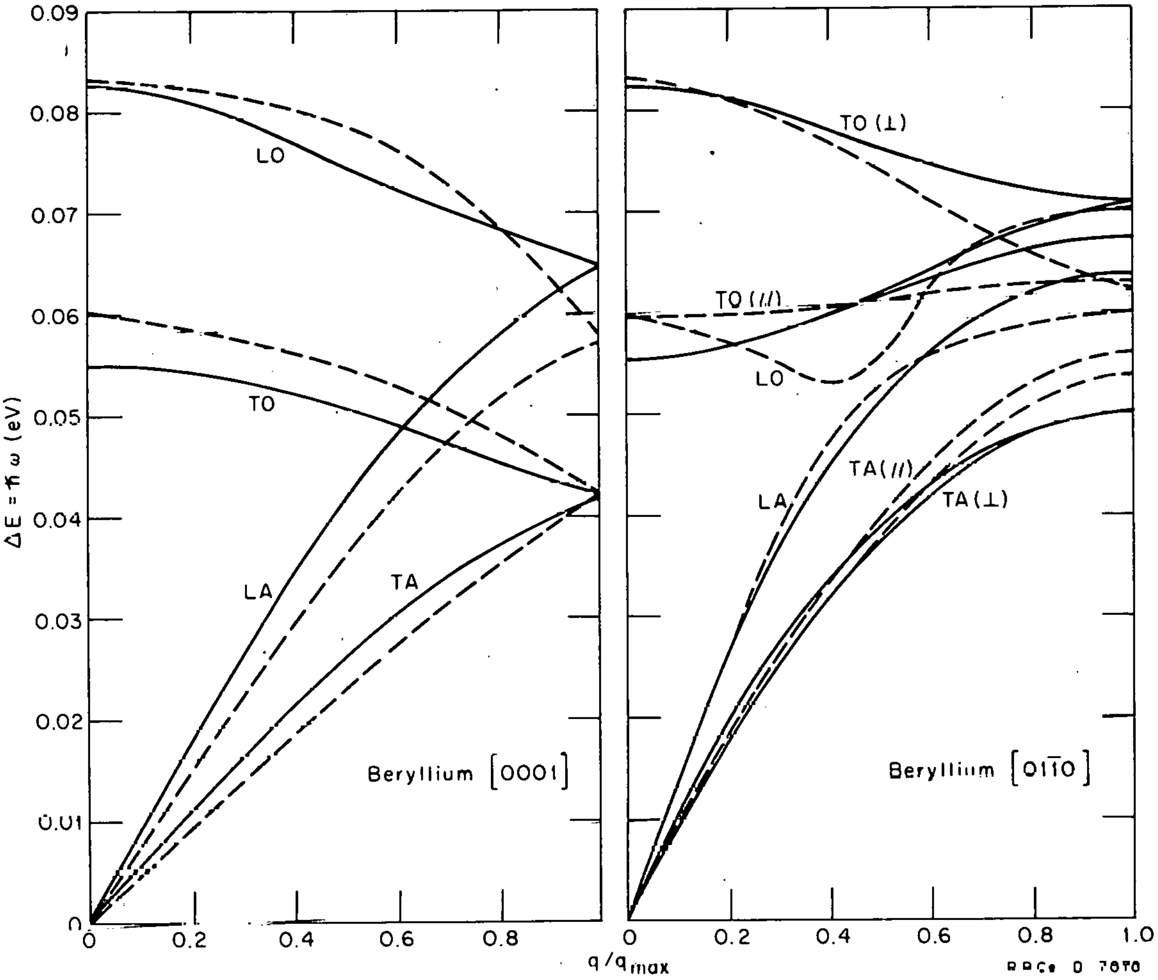

Fig. II-5 Comparison of the model of Gupta and Dayal (dashed lines) with the experimental data (solid lines).

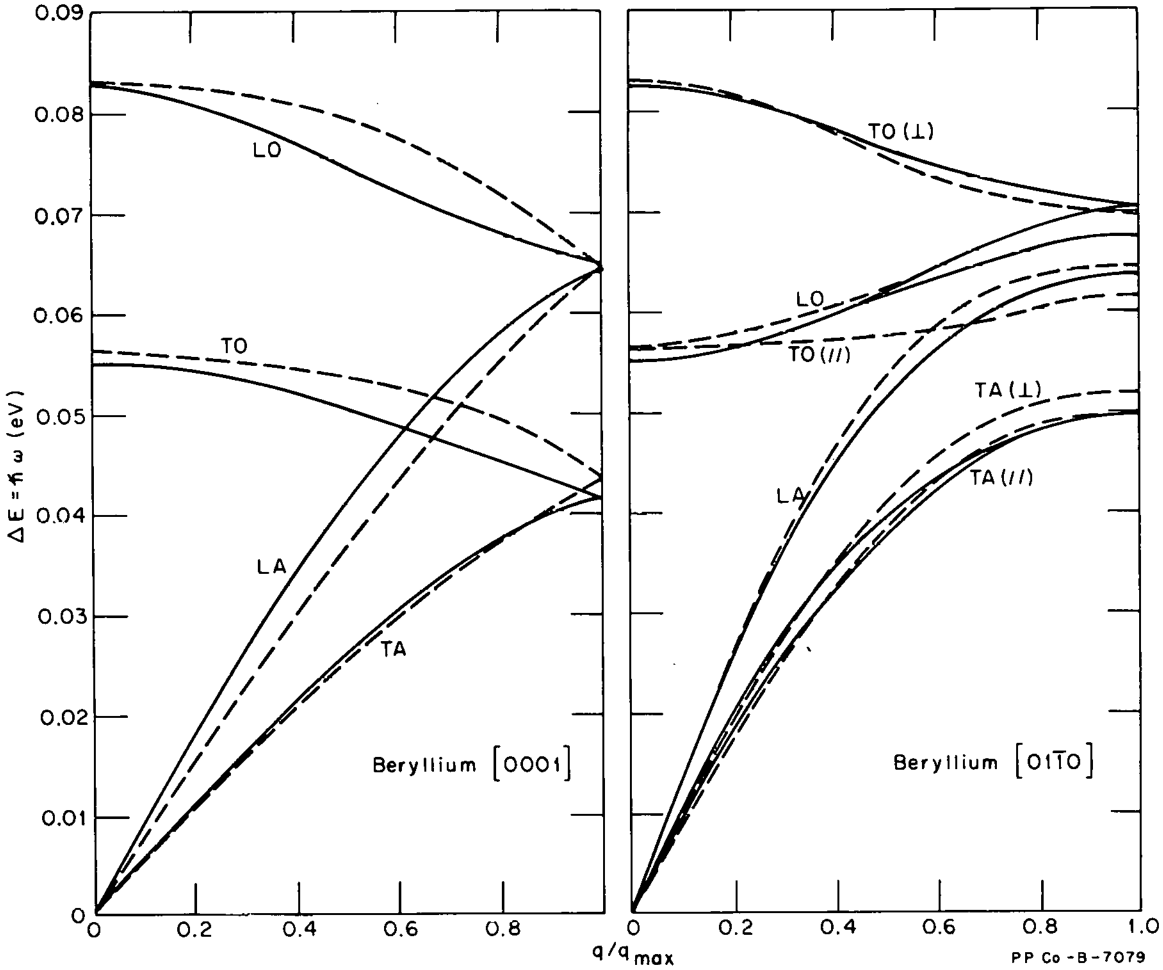

Fig. II-6 Comparison of the axially symmetric lattice model of DeWames, Lehman, and Wolfram (dashed lines) with the experimental data (solid lines).

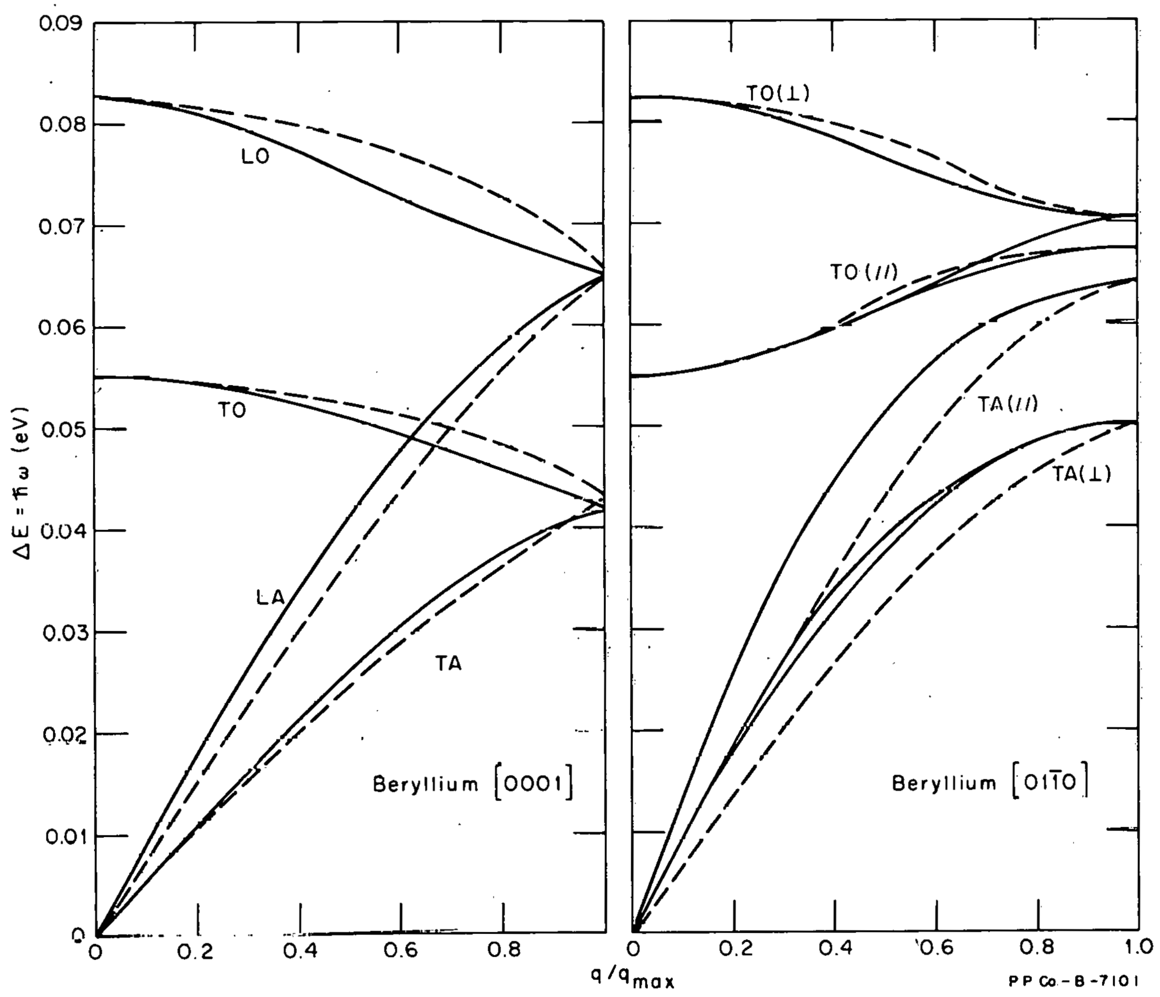

Fig. II-7 Comparison of the tensor force model of Begbie and Born (dashed lines), extended to fourth nearest neighbors, and the experimental data (solid lines).

to occur at small momentum transfer where the calculation is most sensitive to the model. Young at General Atomics has recently attempted such a calculation [9] and obtained rather good agreement with the beryllium powder data [2].

### 1.4 He-3 Counters (R. E. West)

Two He-3 counters were checked by determining their pulse-height distributions and by attempting to compare their jitter times with a $BF_3$ counter. The first counter had a shell of 0.032-inch aluminum, a 6-inch active length, and 1-inch diameter and was filled with He-3 + 3 percent $CO_2$ gas to a pressure of 10 atmospheres. The second counter had a shell of 0.032-inch stainless steel, a 4-inch active length, and a 1-inch diameter and was filled with He-3 gas to a pressure of 10 atmospheres.

Differential and integral pulse-height distributions were obtained by using a Pu-Be neutron source placed so that neutrons were reflected from a piece of paraffin into the counter. The pulse-height distributions were obtained at several different counter voltages. Typical differential pulse-height distributions are shown in Figures II-8 and -9. The He-3 - $CO_2$ counter has a sharper pulse-height distribution as is expected from such counters while the pure-He-3 counter has a double peak.

An attempt was made to compare the jitter times of the two counters with one another and with a $BF_3$ counter which should have a smaller jitter time than

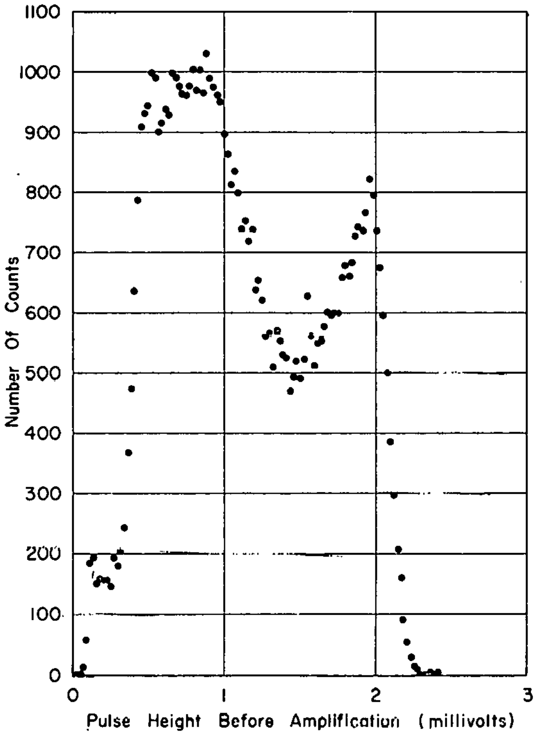

PPCo-B-7618

Fig. II-8 Partial differential cross section measured for polyethylene.

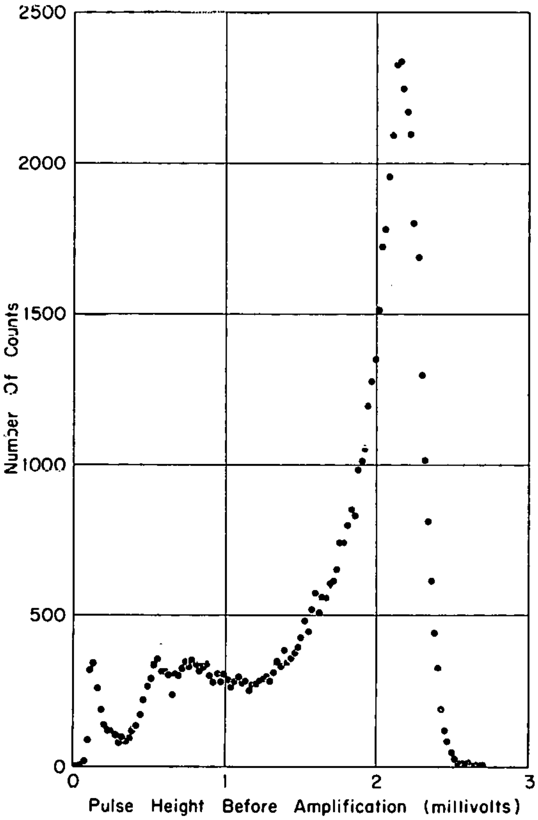

PPCo-B-7617

Fig. II-9 The ratio of the differential cross section measured for polyethylene oriented in two directions.

the He-3 counters. The method used was to look at bursts of neutrons from the MTR time-of-flight Neutron Diffraction apparatus with each of the three counters and to compare the full widths at half maximum (FWHM) of the bursts as seen by the counters. Bursts of approximately 14 microseconds FWHM were obtained as follows: A 42-inch-radius velocity selector chopper, spinning at 10,000 rpm, was used to obtain the initial burst from the reactor. The initial burst was passed through a NaCl single crystal, oriented such that a Bragg reflection was obtained at the counter approximately 2.75 meters from the crystal at a scattering angle of 60 deg. The time-of-flight analyzer was triggered by the rotor, and the time of flight of the burst was recorded and plotted to obtain the FWHM. The number of counts in the peaks ranged from 250 to 1430 for the different runs.

The results are recorded in Table II-1. The counters were checked at several different discriminator voltages over their plateaus, and this is listed under discriminator voltage. The standard deviation of several of the runs were calculated and are listed under "$2\sigma$". No major differences can be seen in the FWHM as measured by the three counters and, hence, the difference in jitter time has no effect on the measured FWHM for bursts as large as 14 microseconds.

Nine more counters of the He-3 - $CO_2$ were studied to test reproducibility. The characteristics of these counters are similar to the first counter. Differential

TABLE II-1

COMPARISON OF JITTER TIME OF He-3 AND $BF_3$ COUNTERS

| Counter | Discriminator Voltage (volts) | Full Width at Half Maximum ($\mu$sec) | $2\sigma$ ($\mu$sec) |
|---|---|---|---|
| Pure He-3 | 7.5 | 14 | ---- |
| Pure He-3 | 15.0 | 13 | 12.5 |
| Pure He-3 | 25.0 | 14 | ---- |
| He-3 - $CO_2$ (3 percent) | 5.0 | 14 | ---- |
| He-3 - $CO_2$ (3 percent) | 15.0 | 14 | 12.4 |
| He-3 - $CO_2$ (3 percent) | 25.0 | 13 | ---- |
| $BF_3$ | 12.5 | 13 | ---- |
| $BF_3$ | 20.0 | 12 | ---- |
| $BF_3$ | 25.0 | 14 | 12.7 |
| $BF_3$ | 40.0 | 13 | ---- |

pulse-height distributions were run for the new counters and compared to the first counter. The gain of all the new counters except two were from 1.0 to 1.5 times the gain of the 1st counter. The other two counters had gains of 6.3 and 0.4 times the gain of the first counter. The gain relative to counter 454 and the capacitance of each counter is given in Table II-2.

TABLE II-2

GAIN AND CAPACITANCE OF He-3 - $CO_2$ COUNTERS

| Counter Number | Gain (relative to counter 454) | Capacitance[a] (picofarads) |
|---|---|---|
| 454 | 1.00 | ---- |
| 801 | 1.18 | 18.0 |
| 806 | 1.20 | 15.5 |
| 808 | 1.13 | 16.2 |
| 807 | 6.30 | 15.5 |
| 809 | 0.42 | 10.0 |
| 1008 | 1.50 | 7.0 |
| 1009 | 1.35 | 7.0 |
| 1010 | 1.00 | 7.5 |
| 1011 | 1.42 | 7.0 |

[a] The $CO_2$ content of counters 1008, 1009, 1010, and 1011 was adjusted such that their gains were approximately the same as counters 801, 806, and 808.

### 1.5 Slow Neutron Inelastic Scattering from Polyethylene (W. E. Moore[a], Y. D. Harker, R. M. Brugger)

The differential scattering cross sections and scattering law have been obtained for highly crystalline polyethylene. Incident energies used were 0.072, 0.030, and 0.017 eV, and scattered neutron spectra were measured for 15 angles ranging from 15 to 145 deg. The range of scattering law variables covered was $0.1 \leq \alpha \leq 15$ and $0 \leq \beta \leq 4$, a generous region of overlap with recent data from RPI[10] and GA[11] which permits direct comparison with these experiments. The high-resolution capabilities of the MTR velocity selector in the lower energy range permits observation of the low-lying skeletal acoustic modes and lattice vibrations which were not resolved from the elastic scattering in the RPI or GA data.

The first scattering material used was the same long chain polyethylene (Marlex 6050) used at RPI. The sample was prepared by slow cooling from the melt to achieve the highest possible crystallinity (approximately 90 percent). The thickness was reduced to 0.006 inch (transmission 89 percent at 0.01 eV) to limit multiple scattering. The cross sections were calculated through use of calibrated beam monitors and the known sample thickness, detector efficiency, and solid angles. The differential cross-section profiles for scattering angles less than 105 deg exhibit structural features coincident with those expected for some of the lower infinite chain vibration modes[12] and the crystalline lattice modes[13]. A typical sample is pictured in Figure II-10. These lowest lying modes are observed clearly by both energy-loss and energy-gain interactions; the numbers labeling these features represent excitation energy in millielectron volt units and, in parenthesis, reciprocal centimeter units. The evidence for observation of the 90-meV level is clearer in some of the data not presented here; the group of levels starting at 130 meV has not been clearly observed in the present experiment. Table II-3 lists the predicted modes of vibration for this energy range.

---

[a] On assignment from Knolls Atomic Power Laboratory.

In order to study these features more clearly, a second sample was prepared from stretch-oriented polyethylene fibers (Marlex 6009). The scattering was measured with the molecular orientation aligned perpendicular (vertical) to the scattering plane in one experiment; and in another, the sample was rotated so as to cause the long-chain molecules to lie within this plane (horizontal). An example of the orientation dependence observed is given in Figure II-11. Pictured there is the ratio of the energy-gain cross sections obtained for four scattering angles lying between 38 and 68 deg, averaged together to reduce the statistical fluctuations. An approximate normalization of the ordinate was achieved by comparing the profiles for

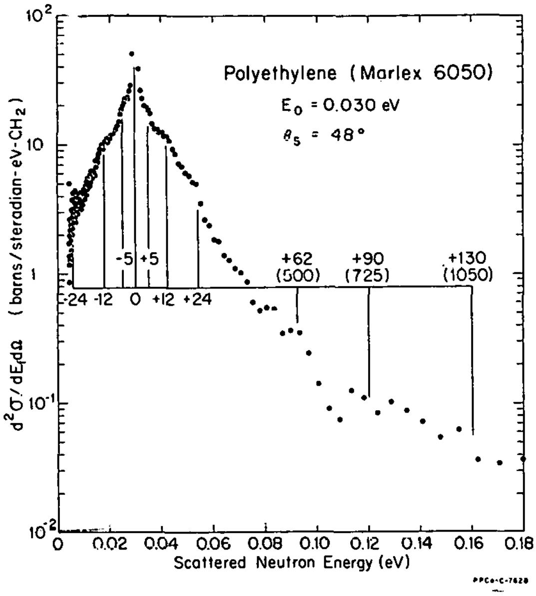

Fig. II-10 Example of differential scattering cross section for polyethylene.

## TABLE II-3

## POLYETHYLENE LOW-ENERGY VIBRATIONS[13, 14]

| Excitation Energy (meV) | Excitation Energy ($cm^{-1}$) | Theoretical Assignment |
|---|---|---|
| 90 | 725 | $CH_2$ rocking mode ($\nu_8$) |
| 62 | 500 | C-C-C bending mode ($\nu_5$ acoustic cutoff) |
| 24 | 200 | C-C-C torsional mode ($\nu_9$ acoustic cutoff) |
| 10 to 15 | 80 to 120 | Lattice vibrational modes along a-axis ($T_x'$) |
| 4 to 10 | 30 to 80 | Lattice vibrational modes along b-axis ($T_y'$) |
| 9 to 12 | 75 to 100 | Lattice rotational modes about c-axis ($R_z$ and $R_z'$) |
| 0 to 12 | 0 to 100 | Lattice translational modes along a-axis ($T_x$) |
| 0 to 7 | 0 to 57 | Lattice translational modes along b-axis ($T_y$) |

all angles and by assuming that the relatively featureless region of energy gain lying between 30 and 50 meV was not orientation sensitive. These very preliminary results indicate that the skeleton-torsional and lattice-translational acoustic modes scatter neutrons more strongly into the plane containing both the incident neutron direction and the molecular axis and that the lattice vibrational and rotational modes scatter less strongly into this plane. This analysis, when complete, should give a clearer understanding of the low-energy transfer processes in polyethylene, and an improvement may be made upon the present computational approximations used in this region for comparison of theory with polyethylene-moderated critical assembly experiments.

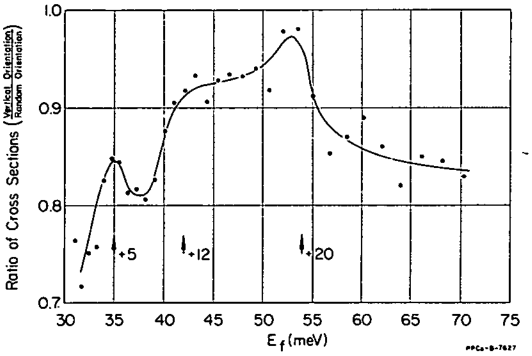

Fig. II-11 An example of the orientation dependence of polyethylene samples.

## 1.6 High-Pressure Neutron Diffraction (R. M. Brugger, E. R. Peterson, R. B. Bennion, T. G. Worlton)

In the search for good pressure cell materials, additional neutron diffraction measurements were made during the quarter at a scattering angle of 58.15 deg, a flight path of 3.07 meters, a channel width of 16 μsec, and a chopper rotational velocity of 6000 rpm. To be useful for high-pressure neutron diffraction, the pressure cell material should have high transmission, low background, and large "windows" between the diffracted peaks, and of course, it should also have high mechanical strength. Table II-4 lists some of the properties of the materials

TABLE II-4

DIFFRACTION PROPERTIES OF SEVERAL PRESSURE CELL MATERIALS

| | Diffraction Characteristics | | | | Pressure Characteristics | | | | |
|---|---|---|---|---|---|---|---|---|---|
| Material | Crystal Structure | Cross Section | Background | Transmission | Mho Hardness | Elastic Modulus ($10^6$ psi) | Yield Strength ($10^6$ psi) | Machining and Handling Characteristics | Comments |
| Al | fcc | 1.6 | Low | High | 2 to 3 | 10.3 | 73 | Ordinary machine tools for soft materials. | By using alternating Al or Mg as sample containers, most of the diffraction pattern may be obtained. These can be used in a compressible gasket device. |
| Mg | hcp | 3.1 | Low | High | 2.0 | 6.5 | --- | Same as Al. | Same as Al. |
| S | Complex Structures | 1.5 | Low | High | 1.0 | --- | --- | Handled most easily by melting or compressing in a die. | This could be used in a gasket device if mixed with Si or SiC for friction. |
| Be | hcp | 7.5 | Medium | Low | --- | 44.2 | 82 | Ordinary machine tools for medium hard steels. Special handling for toxic effects necessary. | Be has desirable "window" characteristics but its cross section is very high. |
| Cr | bcc | 7.0 | Medium | Low | 9.0 | 42.0 | --- | Probably need carboly machine tools. | If the magnetic lines were eliminated, the "windows" would be usable. |
| Si | Diamond Cubic | 2.4 | Low | High | 7.0 | 15.5 | 160 | Hard steel or carboly tools needed. | Si is very brittle, but if contained would be suitable. |
| $Al_2O_3$ | Trigonal | 3.2 | Medium | High | 9.5 | --- | 225 | Can be worked with ordinary tools and then fired for strength | If the peaks can be minimized by collimation, $Al_2O_3$ can be profitably used. Must be supported. |
| V | bcc | 10.0 | High | Low | 4 to 5 | 18 to 19 | --- | Ordinary machine tools. | There are no peaks to hide a sample, but the cross section is very high. |
| Ti-Zr Alloy | hcp | 7.0 | High | Low | 7.0 | --- | --- | Hard steel or carboly machine tools. | Similar neutron characteristics as V but is better for mechanical properties. |

tested. Figure II-12 shows the location of diffraction peaks and windows in terms of the d-spacing between planes. Aluminum, silicon, and vanadium exhibit the best diffraction properties of those materials studied.

A U-235 beam monitor counter was placed 3.07 meters behind the chopper face. A small second maxima was observed at lower energies in the Maxwellian distribution of velocities of the neutrons in the "white" incident beam. It was thought that possibly neutrons were traveling in the reverse direction through the second fluted slot in the chopper. A collimating slit of borated polyethylene lined with cadmium behind this "reversed" chopper slot eliminated the second maxima in the Maxwellian distribution.

A relatively high neutron background was observed in the general area of the diffraction equipment, indicating that special attention must be paid to the shielding of both the He-3 sample counter and the U-235 beam monitor.

The collimator in front of the He-3 counter has a cross-sectional area 1 by 4 inches. Air scattering (no sample) showed a Maxwellian-shaped distribution in the background of this counter. A 1/8-inch slit of cadmium placed in front of this collimator near the sample position resulted in a greatly diminished essentially "flat" background.

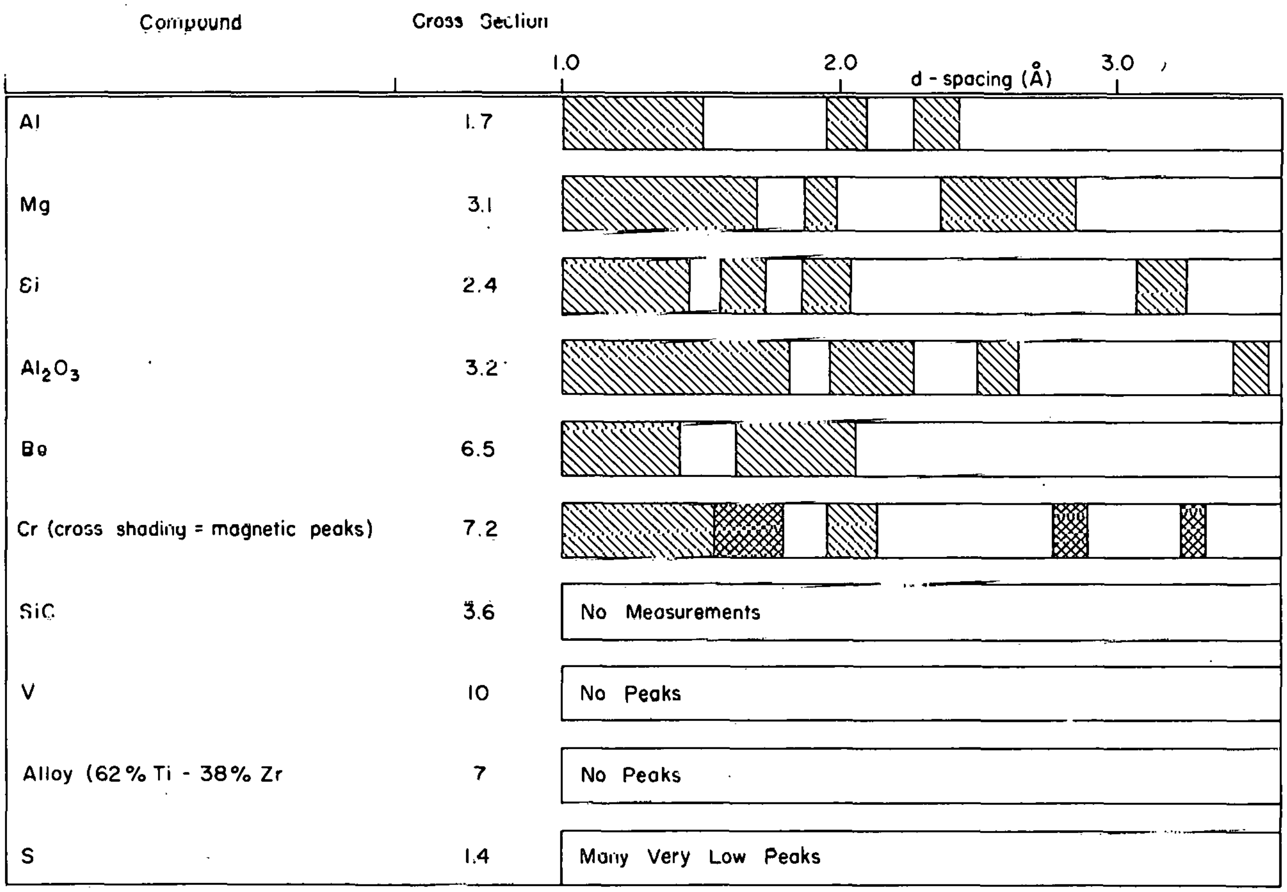

PPCo-B-7619

Fig. II-12 Neutron diffraction peaks and "windows" of proposed sample chamber materials ($2\theta = 58.15$ deg).

A chopper, hydraulic press, and alignment table were designed and are being constructed. The chopper has fluted slots to transmit neutrons of $\infty > E > 0.0006$ eV with a diverging beam of 0.5 degrees. It will rotate at 15,000 rpm giving 7-μsec bursts with 2,000 μsec between bursts. The chopper slot has an area 1/16 by 1 inch at its face. The press uses two opposing 60-ton rams which should be capable of producing 35 to 40 kbar on a one-inch sample with 1/4-inch diameter. The table is designed to have four inches adjustment of the chopper along the neutron beam to permit a minimum distance between the chopper and the sample. The press is designed to have one-inch vertical adjustment even while pressurizing a sample to ensure keeping the sample aligned in the beam from the chopper.

Several designs of pressure cells and their estimated limitations have been considered. Further study of materials and their properties is needed to optimize the designs.

## 2. NUCLEAR CHEMISTRY

(W. H. Burgus)

### 2.1 Swelling of Irradiated Beryllium (R. L. Tromp)

Measurements of high-temperature swelling characteristics of irradiated beryllium metal were continued this quarter. A group of samples previously found to contain 8 cc of He-4 per cc of Be (produced by irradiation to a total fast nvt of 4 x $10^{21}$ neutrons per $cm^2$) was chosen for investigation of density-time-temperature relationships. These measurements should yield a new point on the curve showing the swelling threshold as a function of nvt. Samples were heated at temperatures of 500 and 600°C for six hours each. No evidence of swelling was shown by the samples under these conditions.

### 2.2 Lithium-Drifted Germanium Gamma-Ray Detector System (R. N. Chanda, R. A. Deal)

A lithium-drifted germanium crystal of 2.6 mm depletion depth obtained from a commerical supplier was installed in a recently completed cryostat system and, together with its electronic components, tested for performance characteristics. Pulse amplification was provided by a solid-state preamp employing a liquid-nitrogram-cooled, field-effect transistor and a "Tennelec TC 200" linear amplifier. The preamp was designed and built by the Instrument Development Group at the MTR. Measurements of the 122- and 136-keV lines of Co-57 showed resolutions of 1.75 keV FWHM as shown in Figure II-13.

### 2.3 Composition of Pa-233 Chopper Sample (R. A. Deal, J. W. Codding)

The Pa-233 chopper sample prepared in December 1963 has decayed sufficiently so that it now can be handled without shielding. The sample holder has been opened for examination of the Pa compacts which look much as they did when prepared though somewhat blackened. A small piece of one compact was removed and dissolved for analyses. A gross gamma count showed slight amounts of Zr-95 - Nb-95 and of 2.7-year Sb-125 as the major gamma-emitting contaminants. The U-233 daughter was purified using an anion column, and a sample was electroplated and alpha analyzed. The alpha spectrum showed U-233, U-232, and Pa-231. By estimating the yield of Pa-231 from a comparison of its gamma peaks to those of the remaining Pa-233, the atom percent of Pa-231 at the time of isolation was calculated. In addition, the purified uranium fraction was mass analyzed at ICPP, yielding atom percent values for U-234, U-235, and U-238. The U-233/U-234 ratio at the time of isolation was calculated by estimating the effect of Pa-233 decay between successive $MnO_2$ separations on the amount of U-233 still to be removed. Using all of the above information, the composition of the Pa-233 chopper sample at the time of final Pa-233 isolation was calculated and is shown in Table II-5, listed as atoms/$cm^2$ of each constituent.

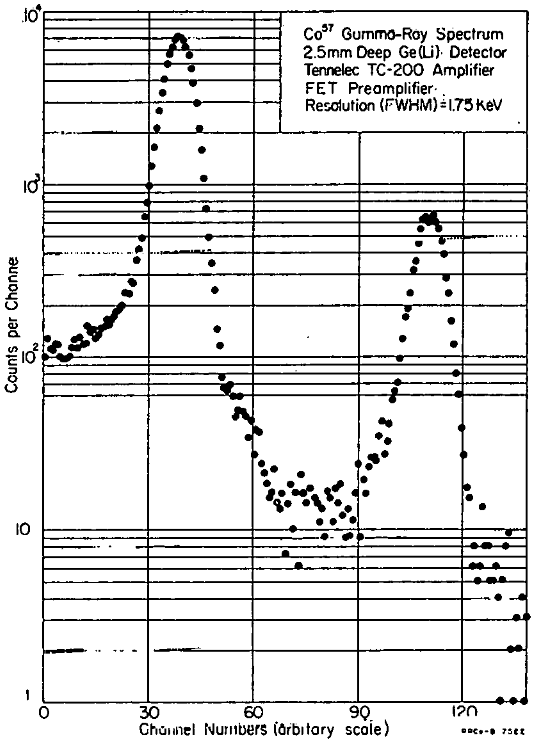

Fig. II-13 Co-57 gamma-ray spectrum taken with Ge(Li) detector.

TABLE II-5

COMPOSITION OF
Pa-233 CHOPPER SAMPLE AT
TIME OF FINAL Pa-233 ISOLATION

| Constituent | Atoms/$cm^2$ |
|---|---|
| Pa-231 | $5.82 \times 10^{18}$ |
| Pa-233 | $3.46 \times 10^{21}$ |
| U-232 | $2.30 \times 10^{17}$ |
| U-233 | $8.63 \times 10^{18}$ |
| U-234 | $3.48 \times 10^{16}$ |
| U-235 | $3.48 \times 10^{16}$ |
| U-238 | $6.96 \times 10^{16}$ |
| Sb-125 | $1.60 \times 10^{17}$ |
| Zr-95 | $1.39 \times 10^{16}$ |
| Oxygen | $8.64 \times 10^{21}$ |

## 3. CROSS SECTIONS
(M. S. Moore)

### 3.1 Manganese Bath Measurements of Eta (J. R. Smith, S. D. Reeder, R. G. Fluharty)

The MTR Crystal Spectrometer has been used as the neutron source for the first measurement using monochromatic neutrons of the absolute value of eta for the three common fissionable isotopes. Measurements were made during 1963 at 0.057 eV neutron energy for U-233 and Pu-239. Preliminary results of these measurements were reported at the American Physical Society meeting in New York during January 1964[14]. Measurements of eta for U-233, U-235, and Pu-239 were made at 0.25 eV neutron energy during 1964. The results of the latter measurements have not been previously reported.

The experiment utilized the well-known manganese bath method for the measurement of neutron source strengths. When the Bragg beam of the crystal spectrometer is absorbed completely in the bath, the resultant Mn-56 activity gives a measure of the number of neutrons in the beam. When the Bragg beam is absorbed in a fissionable sample and the resultant fission neutrons absorbed in the bath, the resultant Mn-56 activity gives a measure of the number of fission neutrons produced as the result of the absorption of all the neutrons in the beam. The ratio of these two activities, modified by a few small corrections, is the value of eta for the isotope of which the sample is composed.

The tank containing the manganese bath is shown in Figure II-14. It is a stainless steel, right-circular cylinder, 42 inches in diameter and in length. A large stirrer, mounted on top of the tank toward the rear, mixed the solution thoroughly after each irradiation before the counting sample was drawn. Before entering the tank, the Bragg beam was required to pass through a mechanical neutron filter [15] which removed all higher order neutrons and transmitted a truly monochromatic beam. A variable aperture collimator beyond the filter trimmed the beam to proper size to fit the sample. Just before entering the tank, the beam passed through a monitor foil of manganese-aluminum alloy. To prevent ambiguities associated with varying irradiation times or reactor levels, all solution activities were normalized to the activity produced in the monitor foil.

The incident beam was allowed to reach the center of the bath before being absorbed. The structure that allowed this penetration and also held the sample was called the sample snout. Two different sample snouts were used, both of which are shown in Figure II-15. There was a two-fold purpose in having two snouts. The heavier snout has a more versatile sample-loading system and would accept samples of various shapes and sizes. The thinner snout was designed to minimize structural material and was made to handle only the set of samples that were obtained from Oak Ridge National Laboratory. These were the same samples that had been used in the Macklin-deSaussure experiment [16]. The second advantage in using two different snouts was that this arrangement gave greater breadth to a parametric study of the important correction for structural absorption.

After the solution had been irradiated and stirred to distribute the Mn-56 activity uniformly, a five-gallon aliquot was drawn into a stainless steel can to be gamma-counted. Two 3- by 3-inch NaI scintillation counters were used, each in its own shield of lead 4 inches thick. While the solution sample was on one counter, the monitor foil was on the other. Samples were interchanged after the first, third, and fifth 30-minute counts. A total of six counts was normally made, giving three counts for each sample on each counter. The entire energy spectrum of the Mn-56 gamma activity was accepted for counting. The electronics system was a simple amplifier-scaler combination with the low-noise, transistorized amplifier set to pass all pulses greater in height than the Ba X-ray from Cs-137 spectrum. This setup yielded the best counting sensitivity and stability of all systems tested for this experiment.

A full discussion of the corrections associated with this experiment will not be made here, but will be found in IDO-17083, which is a full report of this experiment. Many of the corrections were of minor significance. The three largest corrections (fast effect, structural absorption, and the effect of the cadmium introduced to suppress indirect multiplication) were treated parametrically. The fast effect was modified by changing the spacing of the samples and, in case of the plutonium, by using two different sets of samples. The structural absorption was varied by adding aluminum around each snout in

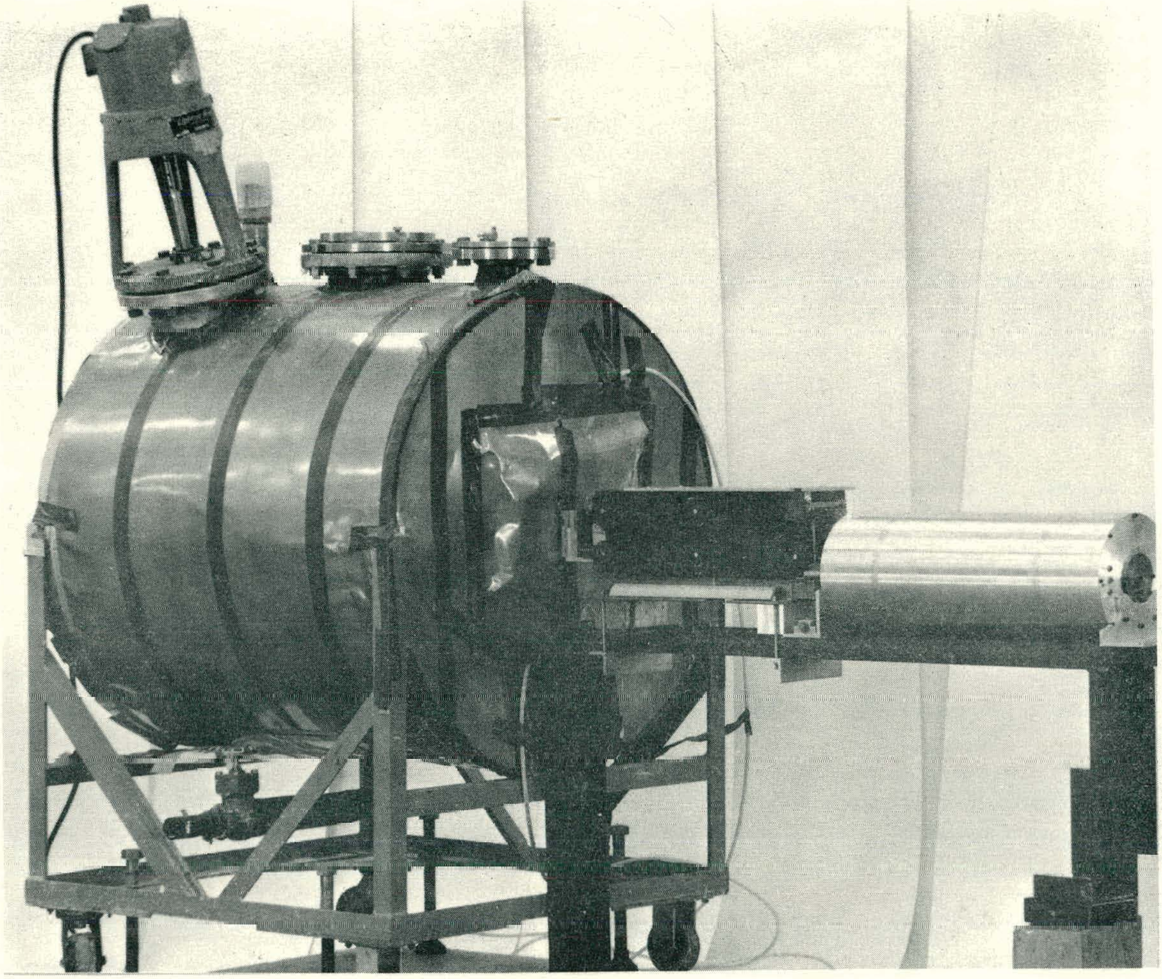

Fig. II-14  Manganese bath exposure tank -- the support holds the mechanical neutron filter and the variable aperture collimator.

addition to using the two snouts of different weights. Indirect multiplication by neutrons returning to the sample from the solution was suppressed by wrapping the samples in cadmium, except for the side facing the incident beam. The effect of this cadmium was investigated by varying both the thickness and the area of the cadmium, with and without changing the exposed area of the sample.

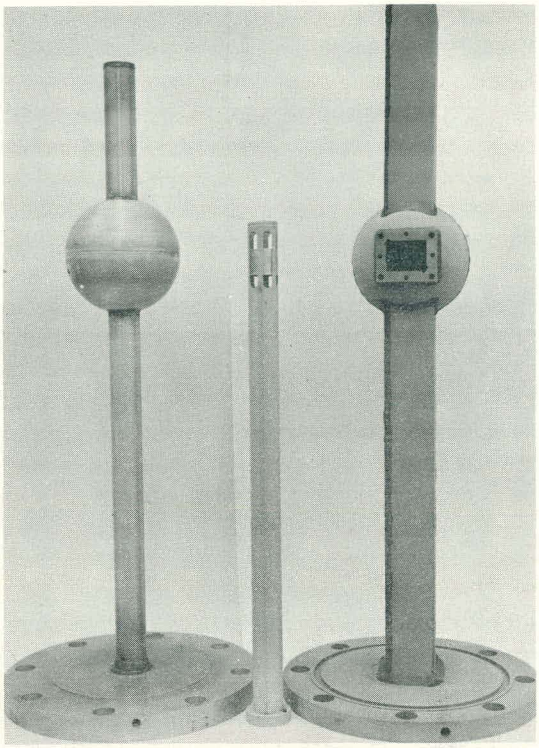
Fig. II-15 The two sample snouts used in the experiment. On the left is the thin snout which uses a sphere having a 0.030-inch wall thickness. The thick snout, shown at right, uses a sphere of 0.086-inch wall thickness. The tube between the snouts is the sample holder used with the thin snout. The sample holder for the thick snout bolts to the flange on the sphere and is not shown.

The least-squares technique of data analysis, described by Cohen, Crowe, and DuMond[17], is ideal for the treatment of data containing many runs and many parameters as is the case for the present experiment. It was applied by describing each day's irradiation as as equation, one side of which was the product of all the factors affecting the activity produced in the solution. The other side of the equation was the solution-to-monitor ratio for the run, corrected for counting and irradiation backgrounds. For those corrections that were calculated but not measured as part of the experimental program, auxiliary equations were added giving the calculated value and variance of the correction. The data from the two energies were treated separately. The array of expressions describing the experiment at 0.025 eV comprised 154 equations with 39 variables. The system at 0.057 eV listed 103 equations with 26 variables. In the least-squares analysis, these systems were reduced to normal sets of linearized equations with the number of equations equal to the number of variables. This system was then solved to yield the best values of the variables, and the matrix of the array was inverted to yield the variances and covariances. In the face of such a task, it is easy to feel grateful for the IBM 7040 computer that ground out the results in double precision in about fifteen minutes.

The final results, as given by the least-squares output, are listed in Table II-6. Errors shown represent one standard deviation. The probable errors (50 percent probability) would be approximately two-thirds of the errors shown.

TABLE II-6

VALUES OF ETA FOR THE THREE COMMON FISSIONABLE ISOTOPES

| | E = 0.025 eV | | E = 0.057 eV | |
|---|---|---|---|---|
| Isotope | Eta | Standard Error | Eta | Standard Error |
| U-233 | 2.298 | 0.009 | 2.288 | 0.009 |
| U-235 | 2.079 | 0.010 | ----- | ----- |
| Pu-239 | 2.108 | 0.008 | 2.034 | 0.009 |

# 4. THEORETICAL PHYSICS

(H. L. McMurry)

## 4.1 A Matrix of Interest in the Inverse-Scattering Problem (A. W. Solbrig, Jr.)

In the "inverse-scattering" problem, one seeks to find the nonrelativistic potential energy between two spinless particles starting from information provided by scattering experiments. If the potential is assumed to be spherically symmetric and if the experimental information consists of phase shifts at fixed energy, a certain infinite matrix arises in the solution of the problem. Some properties of this matrix are known. We have shown that the matrix is of the well-known Hilbert-Schmidt type. Some properties of the matrix, derived laboriously by other workers, are an immediate consequence of this fact. We have attempted, with limited success, to derive other previously unknown properties of the matrix and to simplify the demonstration of other known properties. This work may lead to improved understanding of the very important class of compact operators on extensions of the Hilbert space $l^2$.

## 4.2 Commutation and Uncertainty Relations (A. W. Solbrig, Jr.)

Slow neutron scattering theory makes extensive use of certain operator identities involving commutation relations. The domain of validity of some of these identities, particularly those involving angular momentum and angular position, is not clearly understood. The uncertainty relations and the commutation relations are intimately connected and, in some cases, almost equivalent. We have examined some commutation and uncertainty relations in classical Hilbert space. For the case of angular momentum and angular position, we have obtained a strengthened form of the uncertainty relation along with precise statements about its domain of validity.

In theory of slow neutron scattering from liquids, Griffing has used an operator form of the Langevin equation. This form apparently implies that the time-dependent position and momentum operators satisfy a commutation relation, $[x(t), p(t)] = in\, e^{-\eta t}$, where $\eta$ is the viscous damping coefficient. Conventionally, this relation has a factor unity instead of $e^{-\eta t}$ on the right. Our methods may be useful in examining the validity of the above commutation relation and of results involving it.

## 4.3 Slow Neutron Scattering by Water (H. L. McMurry, G. J. Russell)

A paper has been submitted to Nuclear Science and Engineering which describes a structural model for water which gives calculated slow neutron scattering in good agreement with the low-energy data from the MTR[18].

This model has been used to calculate Legendre moments $\sigma_\ell(E_0) = \int_0^\infty \int_{-1}^{1} \sigma(E_0, E, \mu)\, P_\ell(\mu)\, d\mu\, dE$ which appear in some reactor analysis calculations. The $\sigma(E_0, E, \mu)$ is the partial differential scattering cross section for scattering a neutron from energy $E_0$ to $E$ through an angle whose cosine is $\mu$, and $P_\ell(\mu)$ is the $\ell$th Legendre function. The integrals are obtained numerically; and it is found that to get converged values for $\ell > 1$, very fine-mesh intervals in E must be taken for E near $E_0$, and the mesh in $\mu$ must also be fine. We have used energy intervals $\Delta E$ such that $\Delta E/E_0 \approx 10^{-2}$. The range $-1 \leq \mu \leq 1$ has been divided into as many as 30 intervals with the mesh size $\Delta\mu$ being small where $\sigma(E_0, E, \mu)$ is largest. The total scattering cross section ($\ell = 0$) agrees well with the data[19] for $0.002 \leq E_0 \leq 0.15$ eV, the range for which calculations were made. Table II-7 presents values of $\bar{\mu} = \sigma_1/\sigma_0$ for energies $E_0$ in this range. Also included are $\bar{\mu}$ values calculated using the widely employed Nelkin model [20] modified, however, to include the contribution of the oxygen scattering and to allow for transfers of more than one quantum of vibrational energy.

TABLE II-7

AVERAGE SCATTERING COSINE FOR $H_2O$

| $E_0$(eV) | Observed[a] | MR[b] | N[b] |
|---|---|---|---|
| 0.002 | ----- | 0.017 | 0.035 |
| 0.003 | 0.033 | 0.048 | 0.071 |
| 0.025 | 0.14 | 0.18 | 0.19 |
| 0.05 | 0.22 | 0.27 | 0.28 |
| 0.10 | 0.29 | 0.35 | 0.35 |
| 0.15 | 0.34 | 0.38 | 0.38 |

[a] J. R. Beyster, J. C. Young, J. M. Neill, and W. R. Mowry, GA-629, March 1965.

[b] The notation MR refers to the present model (McMurry-Russell) and N to the modified Nelkin model.

At very low neutron energies, the MR model predicts smaller values of $\bar{\mu}$ because the effective scattering masses for the H atoms (mainly components of mass 75 and 150) are much larger than in the N model (mass 18).

### 4.4 Slow Neutron Scattering by Polyethylene (H. L. McMurry)

The scattering of polyethylene was simulated by using the scattering by $CH_2$ groups in normal butane. Calculations made for W. L. Whittemore of General Atomics agreed quite well with his data for the scattering by 0.233 eV neutrons. The model has been investigated further by making comparisons with Kirouac's recent data[10] and the results are displayed in Figures II-16 and -17.

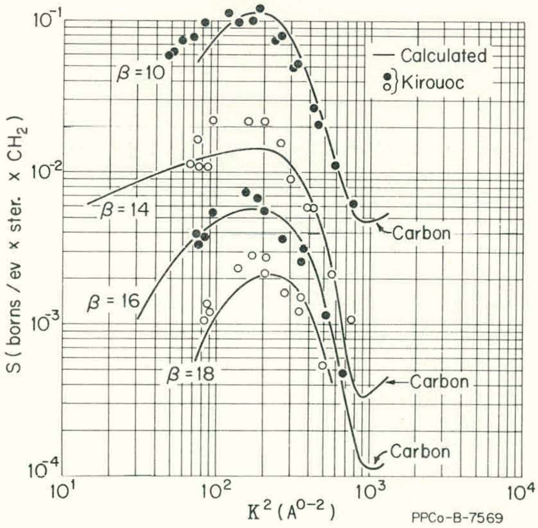

Fig. II-16 $S(\kappa^2, \beta)$ versus $\kappa^2$ for polyethylene T = 302°K.

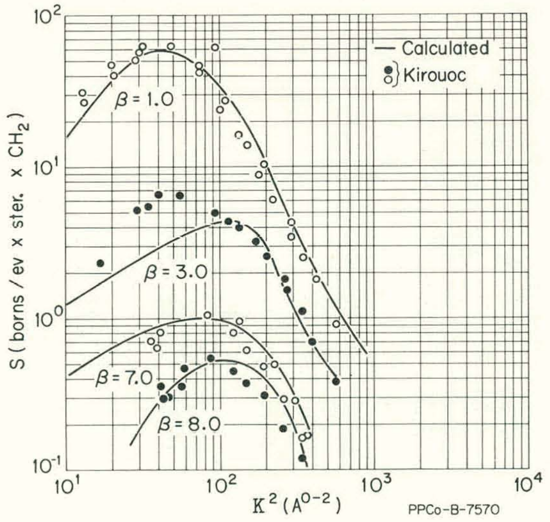

Fig. II-17 $S(\kappa^2, \beta)$ versus $\kappa^2$ for polyethylene T = 302°K.

### 4.5 Theory of Liquid Scattering (G. W. Griffing)

A model for the scattering of neutrons by liquid methane has been investigated. The model used was quite similar to that for gaseous methane except the positional coordinate of the center of mass was assumed to obey the Langevin equation of Brownian motion instead of the equation of motion for a free particle. Comparison of the numerical results with the experimental results indicated that a satisfactory fit to the experimental data could be obtained by treating the viscous damping coefficient $\eta$ appearing in the Langevin equation as a parameter whose value depends upon the momentum transfer in the collision. Using the value of $\eta$ which best fits the quasi-elastic peak and plotting against the momentum transfer $\kappa$ on a semi-logarithm graph resulted in a straight line of negative slope. An extrapolation of this line to zero momentum transfer gave the macroscopic value of $\eta$. This work has been accepted for publication in the Journal of Chemical Physics. Much remains to be done to understand if the empirical results are purely accidental or if they constitute a basis for a deeper understanding of the dynamics of liquids.

## 5. REACTOR EXPERIMENTS

(E. Fast)

### 5.1 Thorium Program -- Distribution of U-233 in Irradiated Thorium Slugs

(R. G. Nisle, E. F. Aber)

Previous measurements on the distribution of uranium in irradiated thorium were reported in 1957[21]. The present work was conducted in basically the same manner except that the sectioning procedure was improved.

Two slugs were cut up; one was the same type as that used previously (RD 1), the other was somewhat smaller. The dimensions and irradiation histories are given in Table II-8.

TABLE II-8

DIMENSIONS AND IRRADIATION HISTORY OF THORIUM SLUGS

| Slug Number | Diameter (cm) | Length (cm) | Nominal weight (grams) | Irradiation Exposure ($10^{21}$ nvt) |
|---|---|---|---|---|
| SR-88 | 2.76 | 15.31 | 900 | 1.8 |
| RD-1 | 3.63 | 16.51 | 1600 | 0.93 |

The irradiation exposures shown in Table II-8 are rough since accurate flux measuring methods were not available. The uncertainty in nvt is estimated at 50 percent of the given value.

A transverse section, 2.5 cm long, was cut from the center part of the slug. The first sample was cut from this section by drilling an axial hole of about 0.5 cm diameter. Additional samples were then cut by drilling progressively larger concentric holes. The bit diameters are given in Table II-9.

## TABLE II-9

## DISTRIBUTION OF URANIUM ISOTOPES IN IRRADIATED THORIUM SLUGS

RD-1

| | Diameters | | | Isotopic Abundances | | | | | |
|---|---|---|---|---|---|---|---|---|---|
| Sample | Inside (cm) | Outside (cm) | Total Uranium (weight percent) | U-233 (percent) | U-234 (percent) | U-235 (percent) | U-238 (percent) | U-233 (weight percent) | Fissions per gram Sample |
| 1 | 0.0 | 0.52 | 0.315 | 98.43 | 1.44 | 0.07 | 0.05 | 0.31 | $6.95 \times 10^{17}$ |
| 2 | 0.52 | 1.03 | 0.310 | 98.44 | 1.46 | 0.05 | 0.04 | 0.31 | $6.59 \times 10^{17}$ |
| 3 | 1.03 | 1.27 | 0.340 | 98.42 | 1.48 | 0.05 | 0.04 | 0.34 | $7.27 \times 10^{17}$ |
| 4 | 1.27 | 1.59 | 0.325 | 98.40 | 1.50 | 0.06 | 0.03 | 0.32 | $6.81 \times 10^{17}$ |
| 5 | 1.59 | 1.91 | 0.335 | 98.38 | 1.53 | 0.05 | 0.03 | 0.33 | $7.90 \times 10^{17}$ |
| 6 | 1.91 | 2.23 | 0.360 | 98.35 | 1.56 | 0.05 | 0.04 | 0.35 | $8.17 \times 10^{17}$ |
| 7 | 2.23 | 2.54 | 0.355 | 98.28 | 1.63 | 0.05 | 0.04 | 0.35 | $9.07 \times 10^{17}$ |
| 8 | 2.55 | 2.86 | 0.390 | 98.17 | 1.70 | 0.06 | 0.06 | 0.38 | $9.55 \times 10^{17}$ |
| | | | ± 0.02 | | | | | ± 0.02 | $\pm 0.10 \times 10^{17}$ |

SR-88

| | Diameters | | | Isotopic Abundances | | | | | | |
|---|---|---|---|---|---|---|---|---|---|---|
| Sample | Inside (cm) | Outside (cm) | Total Uranium (weight percent) | U-233 (percent) | U-234 (percent) | U-235 (percent) | U-236 (percent) | U-238 (percent) | U-233 (weight percent) | Fissions per gram Sample |
| 1 | 0.0 | 0.52 | 0.84 | 94.16 | 5.41 | 0.38 | 0.02 | 0.03 | 0.79 | $8.95 \times 10^{18}$ |
| 2 | 0.52 | 1.03 | 0.88 | 94.16 | 5.40 | 0.39 | 0.02 | 0.03 | 0.83 | $4.69 \times 10^{18}$ |
| 3 | 1.03 | 1.27 | 0.94 | 94.01 | 5.52 | 0.40 | 0.02 | 0.05 | 0.88 | $11.7 \times 10^{18}$ |
| 4 | 1.27 | 1.57 | 1.00 | 93.75 | 5.67 | 0.41 | 0.02 | 0.15 | 0.94 | $13.2 \times 10^{18}$ |
| 5 | 1.59 | 1.91 | 1.91 | 93.69 | 5.83 | 0.43 | 0.02 | 0.03 | 0.85 | $8.25 \times 10^{18}$ |
| 6 | 1.91 | 2.23 | 0.98 | 93.33 | 6.15 | 0.47 | 0.03 | 0.02 | 0.92 | $15.9 \times 10^{18}$ |
| 7 | 2.23 | 2.76 | 1.07 | 92.91 | 6.50 | 0.52 | 0.04 | 0.03 | 0.99 | $16.4 \times 10^{18}$ |
| | | | ± 0.03 | ± 0.01 | ± 0.01 | ± 0.01 | ± 0.01 | ± 0.01 | ± 0.03 | $\pm 0.10 \times 10^{18}$ |

Chemical and mass spectrographic analyses were made on the samples for total uranium and isotopic abundances. Total fissions were determined from the Cs-137 analyses. The results are shown in Table II-9. The results for the RD-1 slug are averages of values measured on two adjacent transverse sections cut from the center part of the slug. Only one transverse section was analyzed in the case of the Sr-88 slug. Figures II-18 and -19 show the radial distribution of the total uranium and U-233 in weight percent. Figures II-20 and -21 show the distributions of fissions and the isotopic abundances of the two most important isotopes, U-233 and U-234. In making comparisons, care must be taken to allow for scale differences and displaced origin.

Qualitatively, the radial variation of uranium isotopes is in agreement with previous results and calculations[21]. Improved calculations on the above slugs are in progress and will be reported later. Results obtained in the previous work on an RD-1 type slug are reproduced in Figure II-22 for comparison. It should be born in mind that it is difficult to generalize on the basis of the above results because of the differences in radii and exposure times of the two slugs, and because of uncertainties introduced during sampling.

### 5.2 A Comparison of Calculated and Measured Reactivities for a Typical ARMF Experiment (D. A. Millsap)

Knowledge of the energy dependence of the real and adjoint fluxes in the sample measuring positions of the ARMF-I and ARMF-II reactors may be useful and even essential for the proper interpretation of reactivity measurements. By use of an appropriate computer code, one should be able to calculate the desired

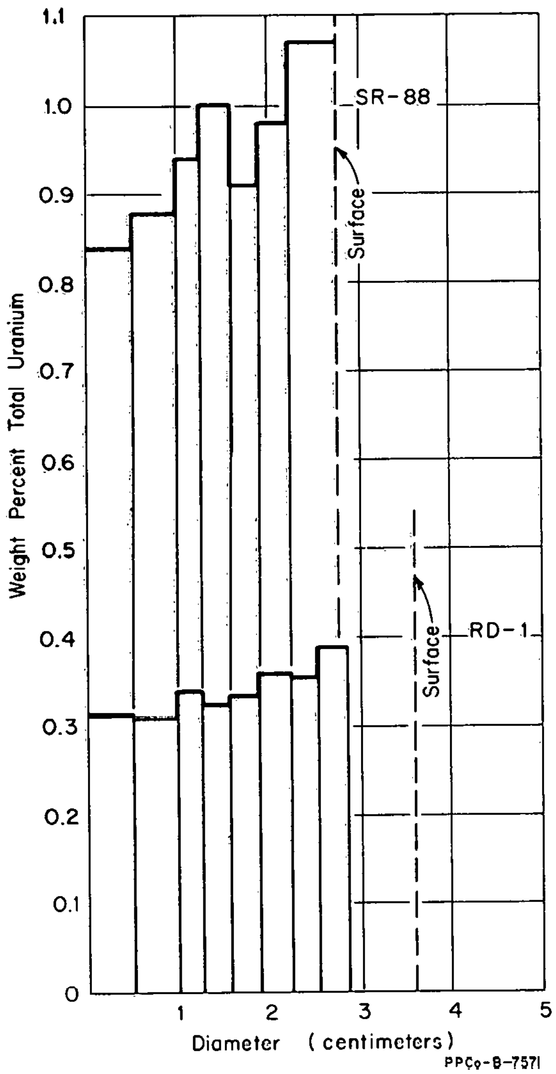

Fig. II-18 Radial distribution of total uranium in irradiated thorium slugs.

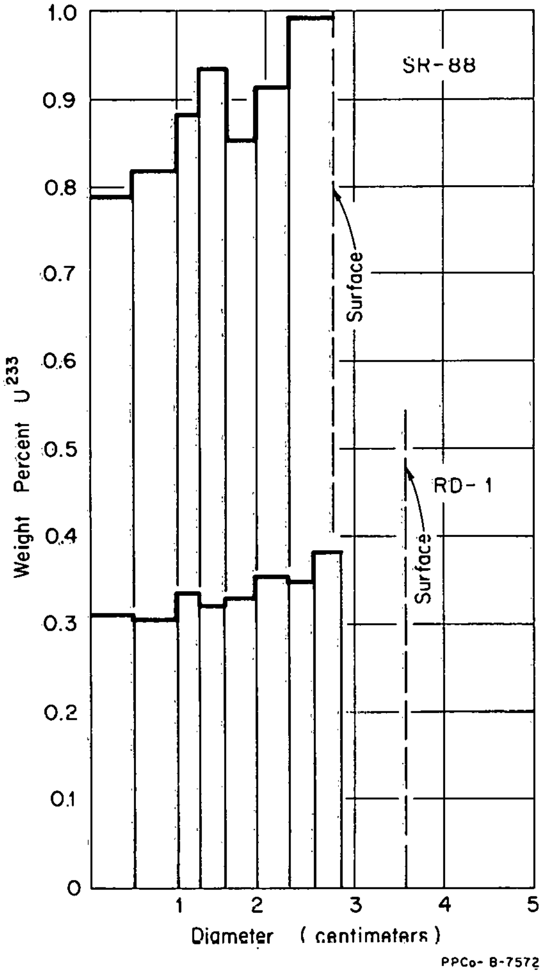

Fig. II-19 Radial distribution of U-233 in irradiated thorium slugs.

fluxes, however, since approximations must be made for any reactor calculation, some criteria must be employed to decide whether a particular calculational model has given the real and adjoint fluxes with sufficient accuracy and detail. One approach is to use the calculational model and its resulting fluxes to calculate the reactivities of some representative samples for which actual measurements are available. Presumably, if a model can be used to predict accurately reactivities for materials with fairly well-known cross sections, then the real and adjoint fluxes of the model could be used with some assurance in interpreting the reactivity measurements of materials of similar but less well-known cross sections.

A series of exploratory calculations has been made for the ARMF reactors in order to obtain useful calculational models for these reactors. Preliminary models have been developed and used to predict the reactivities of a series of samples used in the ARMF scattering experiment [22]. These predictions are reported and compared with measured values.

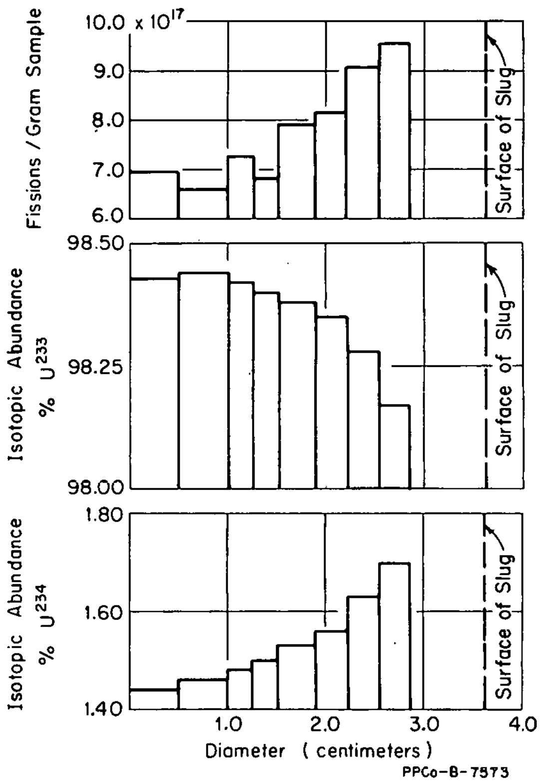

Fig. II-20 Radial distribution of fissions and isotopic abundances in irradiated RD-1 thorium slug.

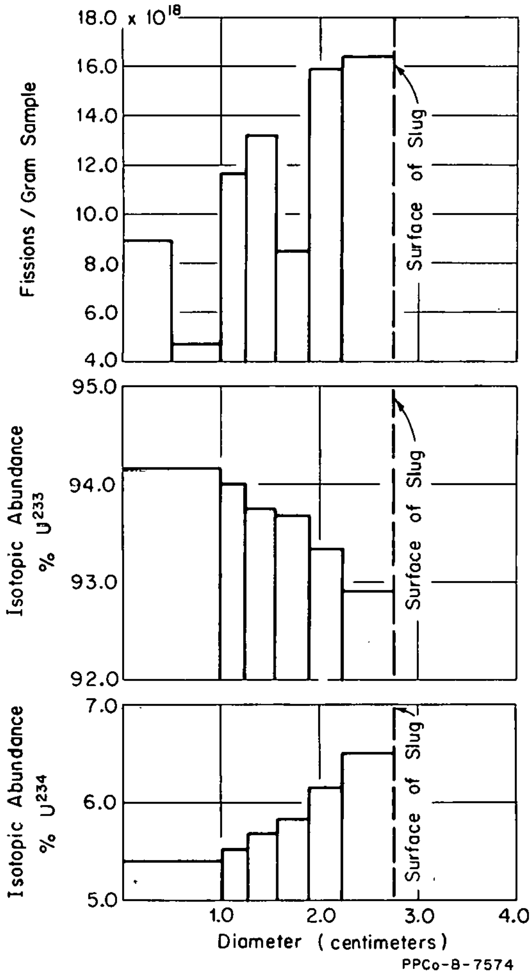

Fig. II-21 Radial distribution of fissions and isotopic abundances in irradiated SR-88 thorium slug.

Putnam has shown [23] that the reactivity due to a constant perturbation (and, thus, time independent) may be expressed either as a function of eigenvalues alone or as one of two alternate expressions involving real and adjoint fluxes with appropriate cross sections. The expression using eigenvalues is simply

$$\rho = (\lambda - \lambda_c)\, \lambda_c^{m} \lambda^{n} / \lambda_c \lambda \qquad (1)$$

where

$\rho$ = the reactivity effect of the perturbed condition relative to some critical (ie, unperturbed) state of the reactor

$\lambda_c$ = the calculated eigenvalue (or correction factor) for some critical state of the reactor

$\lambda$ = the calculated eigenvalue for the perturbed condition

m,n = arbitrary exponents.

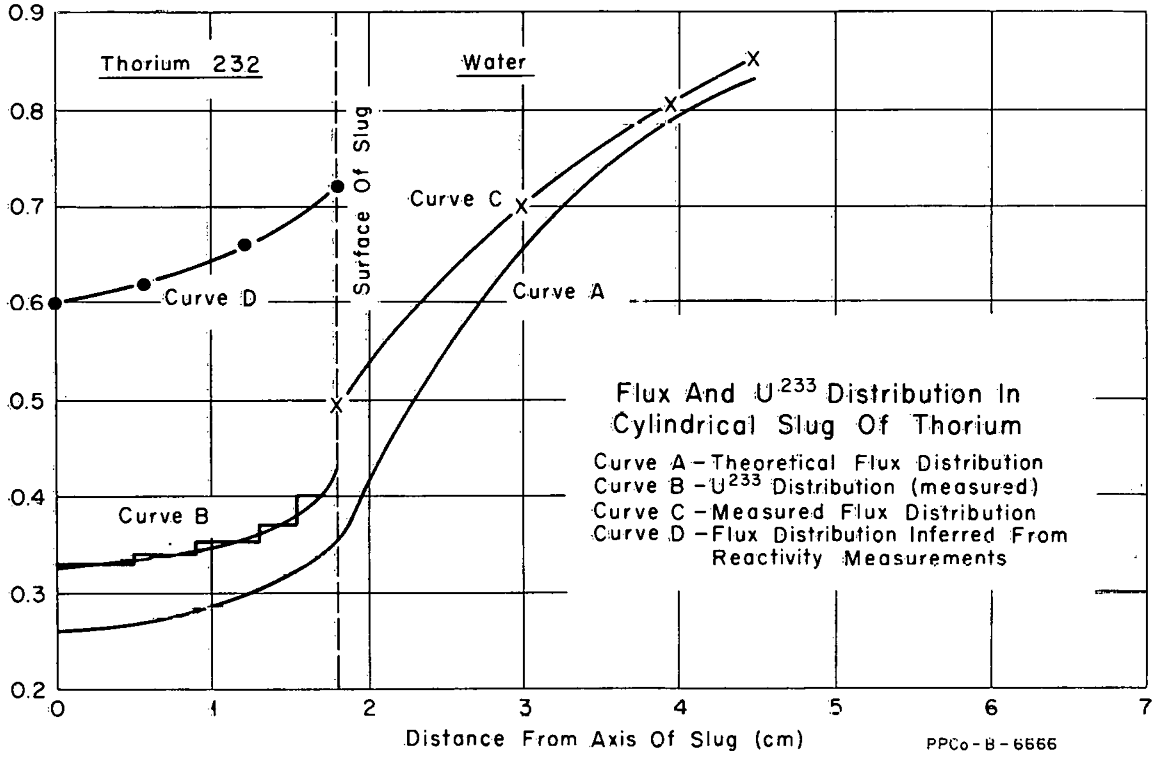

Fig. II-22 Flux and U-233 distribution in cylindrical slug of thorium.

The other expressions for reactivity are too lengthy to warrant quoting in the present context but are nearly identical to those generally derived from transport perturbation theory. Their primary distinction resides in the manner in which the real and adjoint fluxes are combined with the cross-section changes to calculate the reactivity. Briefly, it is shown that one has the option of (a) using the real fluxes from the perturbed case with the adjoint fluxes from the unperturbed case or (b) using the real fluxes from the unperturbed case with the adjoint fluxes from the perturbed case. One of these two expressions will usually be required when calculations of say the individual contributions of absorption or scattering to the total reactivity are desired.

A simple 4-region, cylindrical model of ARMF-II was used by Foell[24] to determine real and adjoint fluxes in a cadmium-shielded region. Preliminary models in the present work used 18 regions for ARMF-I and 20 for ARMF-II. The model was determined by trial and error,with major emphasis placed on the geometric representation necessary to obtain $\lambda_c \approx 1$. Annular regions represent the sample center hole, control rod followers (aluminum), fuel plates, side plates, reflector, etc, and were made as nearly identical as possible to the reactor represented.

The computer code, AIM-6[25], has been used to test the preliminary models for the ARMF-I and -II. AIM-6 is a multigroup,one-dimensional diffusion code which handles up to 18 energy groups, 20 regions, 101 space points, and allows downscattering to a given group from any high group. It calculates real and adjoint fluxes and provides for a punched-card output of these results. For these initial calculations, four energy groups were used[a] with downscattering to a given group allowed from all of the higher energy groups. Both models used the full complement of 101 space points. Flux-averaged cross sections for the materials contained in the various regions of the two reactor models were obtained by use of the computer codes GAM-1[26] and TEMPEST-II[27]. The eigenvalues for the adopted models were 1.035670 for the ARMF-I and 1.035435 for the ARMF-II.

A set of nine samples from the ARMF scattering experiment[22] was chosen for a comparison of measured and calculated reactivities. The set consists of $H_2O$, Be, $D_2O$, C, Mg, Al, Zr, Pb, and Bi. The sample holders were polyethylene capsules inside aluminum cans.

The samples were measured in the center positions of both reactors. Their total reactivities, listed in Column 1 of Table II-10, are quoted net to a void reactivity measurement. Column 2 of the table gives an estimate of the absorption component of the reactivity obtained from a calibration with solutions of boric acid in $D_2O$. The difference between the measured total reactivity and the estimated absorption component is given as the net scattering reactivity in Column 3 of Table II-10. This necessarily includes any reactivity due to n-2n reactions.

Reactivities were calculated from the eigenvalues and by PERT, a computer code based on diffusion-perturbation theory[28]. The PERT code used the card output containing the real and adjoint fluxes calculated by AIM-6.

Calculated reactivities for a given sample were obtained as follows:

(1) The cross sections of the three central regions of each model were modified to correspond to that of the sample, the polyethylene holder, and the aluminum capsule, respectively

(2) A core calculation was then made for the new arrangement from which the eigenvalue, $\lambda$, and a card output of the "unperturbed" real flux were obtained

(3) A similar calculation was made for a void in the sample region to obtain the eigenvalue, $\lambda_c$, and the "unperturbed" adjoint fluxes

(4) The card outputs for the "perturbed" real fluxes and the "unperturbed" adjoint fluxes were combined with appropriate $\delta\Sigma$'s as inputs for a PERT code calculation

(5) The PERT calculation was used in a manner which gave the total, absorption, scattering, and n-2n reactivities

---

[a] Group 1 -- $1 \times 10^7$ eV - $8.21 \times 10^5$ eV
Group 2 -- $8.21 \times 10^5$ eV - $5.53 \times 10^3$ eV
Group 3 -- $5.53 \times 10^3$ eV - 0.532 eV
Group 4 -- 0.532 eV - 0 eV

(6) The results were then scaled to take into account the actual length of the measurement samples.

As a check on the PERT calculations, total reactivities were also calculated from the eigenvalues, $\lambda$ and $\lambda_c$, using Equation (1), with m = 0, n = 1; ie, $(\lambda - \lambda_c)/\lambda_c$ (Column 8, Table II-10). The resulting predicted reactivities are also shown in Table II-10 (Columns 4 through 7).

## TABLE II-10

### MEASURED AND CALCULATED REACTIVITY VALUES IN ARMF-I AND ARMF-II

| | Measurements ARMF-I | | | PERT Calculations ARMF-I | | | | Eigenvalues |
|---|---|---|---|---|---|---|---|---|
| | Total Reactivity | Absorption Reactivity | Scattering Reactivity | Total Reactivity | Absorption Reactivity | Scattering Reactivity | N-2N Reactivity | Total Reactivity |
| $H_2O$ | -194.7 | - 67.0 | -127.8 | -231.78 | - 84.76 | -147.03 | --- | -232.4 |
| $D_2O$ | - 50.4 | - 0.5 | - 49.9 | - 42.93 | - 0.86 | - 42.59 | + 0.51 | - 43.0 |
| Be | - 27.5 | - 4.6 | - 22.9 | - 13.42 | - 12.91 | - 25.32 | + 24.81 | - 13.4 |
| C | - 15.8 | - 1.5 | - 14.3 | - 12.65 | - 1.24 | - 11.42 | --- | - 12.7 |
| Mg | - 15.8 | - 10.2 | - 5.6 | - 21.74 | - 18.78 | - 2.96 | --- | - 21.8 |
| Al | - 50.0 | - 45.3 | - 4.7 | - 57.97 | - 52.85 | - 5.12 | --- | - 58.1 |
| Zr | - 38.7 | - 26.3 | - 12.4 | - 48.11 | - 42.71 | - 5.40 | --- | - 48.2 |
| Pb | - 26.0 | - 18.4 | - 7.6 | - 24.38 | - 20.50 | - 3.88 | --- | - 24.5 |
| Bi | - 9.3 | - 3.6 | - 5.7 | - 8.23 | - 3.67 | - 4.65 | + 0.09 | - 8.3 |

| | Measurements ARMF-I | | | PERT Calculations ARMF-I | | | | Eigenvalues |
|---|---|---|---|---|---|---|---|---|
| | Total Reactivity | Absorption Reactivity | Scattering Reactivity | Total Reactivity | Absorption Reactivity | Scattering Reactivity | N-2N Reactivity | Total Reactivity |
| $H_2O$ | + 76.1 | -538.5 | +614.6 | +243.91 | 694.56 | +938.47 | --- | +244.4 |
| $D_2O$ | +437.7 | - 3.8 | +441.5 | +398.99 | - 7.45 | +399.54 | + 6.90 | +400.0 |
| Be | +449.4 | - 33.0 | +482.4 | +409.61 | -110.88 | +209.66 | +310.83 | +410.6 |
| C | +123.5 | - 9.4 | +132.9 | + 89.24 | - 7.65 | + 96.89 | --- | + 89.3 |
| Mg | - 2.9 | - 75.8 | + 72.9 | -160.63 | -188.24 | + 27.61 | --- | -161.1 |
| Al | -237.8 | -356.4 | +118.6 | -291.16 | -347.62 | + 56.45 | --- | -292.0 |
| Zr | - 93.7 | -203.1 | +109.3 | -376.70 | -435.58 | + 58.88 | --- | -377.8 |
| Pb | - 59.9 | -140.2 | + 80.3 | - 89.31 | -131.28 | + 41.96 | --- | - 88.7 |
| Bi | + 59.9 | - 25.2 | + 85.0 | + 27.43 | - 24.65 | + 50.95 | + 1.13 | + 27.4 |

One significant modification of the basic models was made for the sample calculations. It was recognized that the true leakage from the samples could not be duplicated by the one-dimensional approximation since this implies that the sample (for calculational purposes) is the same length as the core. Such a sample representation considerably overestimates the true leakage, particuarly for the void calculation. The axial leakage for all sample calculations was equalized by placing the axial buckling equal to zero in the sample regions.

In general, the calculated reactivities agree fairly well with the measured values. For the ARMF-I, calculated results agree to within 25 percent of the measured total reactivities for all but the Be and Mg samples. In the case of Be, the calculated reactivities due to scattering and n-2n reactions nearly balance each other. Since the calculated absorption reactivity is already higher than that estimated from the measurements, there is a strong indication that one or more of the input cross sections are in error. The calculated absorption reactivity of Mg is obviously too high since no realistic change in the scattering effect would bring the results into line.

The agreement of results for the ARMF-II is poorer, with $H_2O$, Mg, and Zr showing the greatest disparities. Both Mg and Zr give calculated reactivities which are far too negative, implying that probably their input absorption cross sections are incorrect; for Mg, this is in line with the conclusion from the ARMF-I calculation. A part of the discrepancy for water, no doubt, lies in the fact that the total reactivity in ARMF-II is the difference of two relatively large components, leading to a high percentage error. However, the scattering reactivity is quite high and may be so because of the assumption that axial leakage is the same as that of the void. The calculated scattering reactivities for the ARMF-II are consistently lower than those obtained from the measurements for all but the $H_2O$ and Be. The deviations are believed due to deficiences in the calculational model rather than errors in input cross sections. Thus, though the procedure shows promise, additional refinements in both the input cross sections and the calculational models are required.

The preliminary four-group models developed thus far show considerable promise of improving the interpretation of reactivity measurements in the ARMF reactors. Additional refinements to the calculations are planned including: The GAM-1 input cross sections will be modified in cases where there are clear discrepancies with other sources of equal or greater validity. The number of groups will be increased to assess the influence of group structure on reactivity. R, z calculations will be made using a two-dimensional reactor code and should provide a check on those assumptions of the present model pertaining to sample length and axial leakage. A transport code will be used in an attempt to obtain better estimates of scattering reactivities. Upscattering will be included in the thermal groups. It is expected that some combination of the above approaches will improve the agreement between calculated and experimental results.

## 6. PRECISION ENERGY MEASUREMENTS USING LITHIUM-DRIFTED GERMANIUM DETECTORS

(W. W. Black)

The advent of the lithium-drifted, germanium [Ge(Li)] detector has made it possible to measure gamma-ray energies with increased precision. However, to take advantage of this increased precision, it is necessary to have a better understanding of the amplifier and multichannel analyzers associated with the detector. The object of this study was an attempt to find a procedure by which it would be possible to measure gamma-ray energies with considerable precision on a routine basis. In order to make precise measurements, the amplifier-analyzer system (AAS) must have good stability and accurately known linearity characteristics. This report will concern itself with the subject of linearity and the subsequent measurement of gamma-ray transition energies.

## 6.1 Determination of the Amplifier-Analyzer System's Nonlinearity

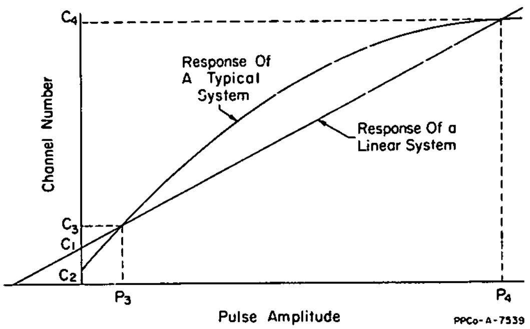

Fig. II-23 Comparison of the response of a typical amplifier-analyzer system (AAS) and an ideal linear AAS to a linear pulser.

Figure II-23 illustrates the channel-versus-pulse-amplitude response of a typical AAS (greatly exaggerated for purpose of illustration) as compared to the response of a linear system. Channel C2 is the channel corresponding to a pulse of zero amplitude. The value of $C_2$ is determined by the "zero" control on the multi-channel analyzer and is variable over a range of a few channels. Channel $C_1$ is uniquely defined by the coordinates ($P_3$, $C_3$) and ($P_4$, $C_4$) in the following way: The "zero" control and the pulser amplitudes are adjusted so that $C_3 = \beta P_3$ and $C_4 = \beta P_4$ where $\beta$ is a constant. Channels $C_3$ and $C_4$ are arbitrarily chosen. For the 1024-channel analyzers to be described here, $C_3 = 63.5$ and $C_4 = 831.5$. These values were chosen primarily to facilitate the collection of the linearity data.

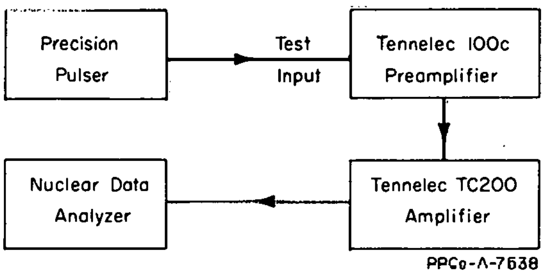

Fig. II-24 Configuration used to measure nonlinearity of amplifier-analyzer systems.

To obtain the linearity data, the system shown in Figure II-24 was used. With the aid of a precision linear pulser, the linearity of an AAS can be measured with rather high accuracy if it is stable enough to hold the pulser output within a few hundredths of a channel for a period of ≈ 30 seconds. Of course, the pulser used must have good stability and linearity characteristics. The pulser used in the experiments to be described here has an amplitude stability of several parts in $10^5$ for the order of minutes and better that 1 part in $10^4$ for the order of hours. The output pulse amplitude is determined by a precision voltage divider. The linearity of this divider has been measured to be good to several parts in $10^5$ by measurements with a precision bridge. The pulser dial can be read directly in increments of 0.01 from 0.00 to 1000.00. A complete description of the pulser can be found in Reference 29.

Normally, with the pulser set at a given reading, the resulting pulses will be stored in one or two channels of the multichannel analyzer. Since there are no more than two channels represented in these "pulser peaks", it is difficult to determine within a few hundredths of a channel the center of the peak. However, the center of a channel can be determined visually with an accuracy of better than 0.05 channels. For example, if the pulser is adjusted so that pulses are falling in channels 63 and 64 with equal frequency, then the center of the pulser peak is in channel 63.50. Therefore, these half-channel units were used to obtain the linearity data as follows: Suppose the multichannel analyzer is a 1024-channel analyzer, then the pulse amplitudes and the "zero" control are adjusted so that when the pulser reads 63.50 and 831.50, the resulting pulser peaks are in channels 63.50 and 831.50, respectively. This defines $C_3$, $C_4$, and $\beta$. If the measurement is now to be made around channel 400, the pulser dial is adjusted to read 399.50. If the pulser peak because of the nonlinearities of the system is not in 399.50, the pulser dial is adjusted until the pulses fall in channel 399.50. Now the pulser dial might, for example, read 399.86. Thus, the AAS response deviates from a linear response by + 0.36 pulser units at channel 399.50. The deviation in pulser units must be converted to channel units for actual correction of the data. This is simply done since the ratio of pulser units to channel units is one within the necessary accuracy. Using this method at many channels, from channel zero through channel 1000, the nonlinearity of the system is determined. In practice, the points at channel 63.5 and 831.5 were checked frequently so that small adjustments could be made for slight "zero" and gain drifts that occur during the course of the measurements.

Once the nonlinearity has been measured, a plot of "correction-to-be-applied" versus channel number can be drawn. The correction is just the deviation of the true response from that of a linear response.

### 6.2 Energy Measurements

Now suppose that a gamma-ray spectrum with several photopeaks has been obtained with a Ge(Li) detector and that some of these photopeaks correspond to well-known energies. If linearity correction data are available, the photopeak locations can be corrected for the nonlinearity of the AAS. The corrected channel locations ($X_i$) for the photopeaks will be related to their corresponding energies ($E_i$) by

$$E_i = BX_i$$

where B represents the particular energy/channel value chosen for the measurement. Since the energies corresponding to some of the $X_i$ are known, B can be determined by least-squares methods. However, this is a somewhat simplified picture. In practice, the value of $C_1$ is not exactly that defined by the coordinates ($P_3$, $C_3$) and ($P_4$, $C_4$) due to arbitrary adjustments of the zero control. This results in all photopeak locations being shifted by some constant amount. Taking this shift into account, it is possible to express the energy of a gamma ray as a function of the channel position of its photopeak with the displacement of $C_1$ ($\Delta C_1$) and B as parameters. Since both the energy and photopeak positions of some of the gamma rays are known, the two parameters, $\Delta C_1$ and B, can be determined by least-squares methods. Once $\Delta C_1$ and B are known, the energies of all the remaining gamma rays can be determined from their corresponding photopeak positions. The formulation of E as a function of the photopeak position, with $\Delta C_1$ and B as parameters and the incorporation of this formulation into a FORTRAN computer program, will be given in a later section.

To test the performance of the computer program and the precision of the method of energy measurements mentioned above, a test spectrum was obtained and analyzed. Ir-192 was chosen as a source of the "unknown" energies because its decay includes several gamma-ray transitions that have been measured with high precision[30,31]. For calibration the Ir-192 source was combined with sources of Au-199, Au-198, Y-88, and Cu-64 and a spectrum of radiations from all 5 isotopes was taken. Figure II-25 shows the resulting spectrum. From the energies and photopeak positions of the Au-199, Au-198, Y-88, and Cu-64 calibration transitions, the parameters $\Delta C_1$ and B were calculated. Using these parameters and the photpeak positions, the energies of the calibration

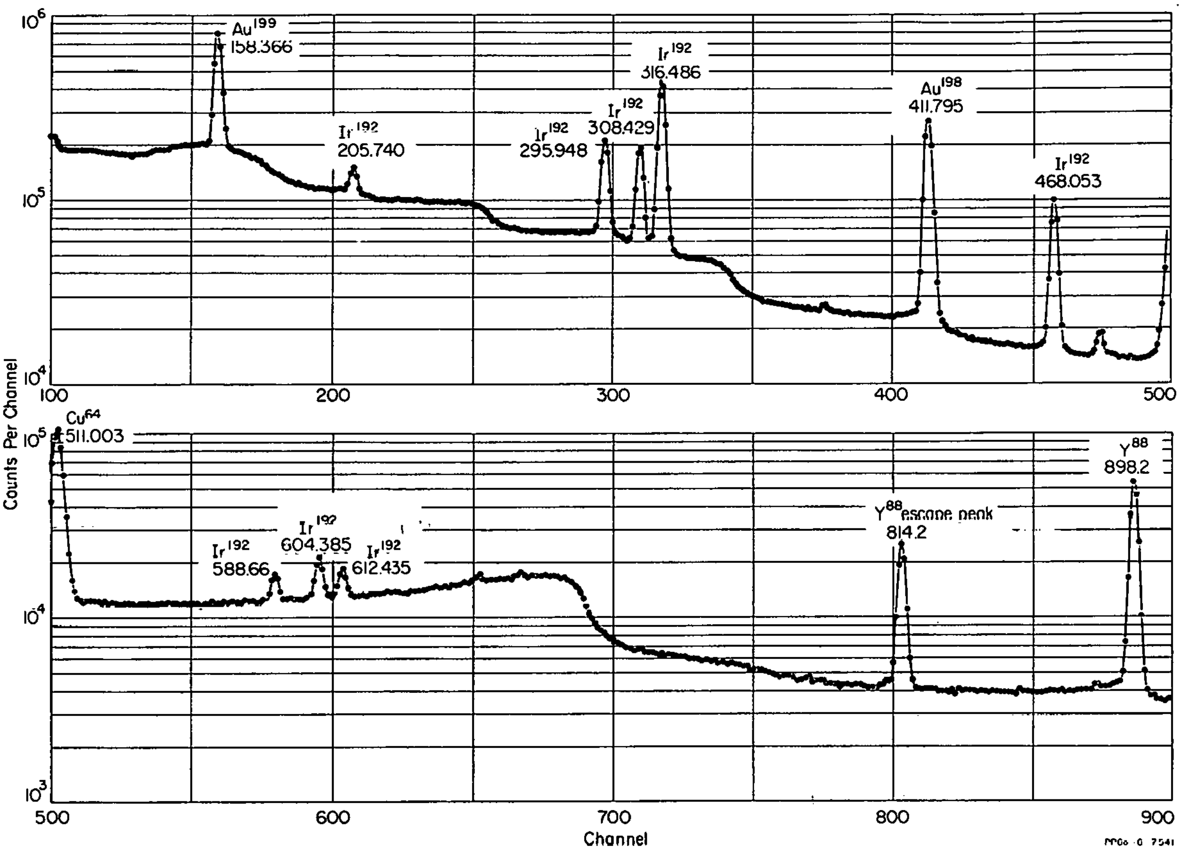

Fig. II-25 A combined spectrum of Ir-192, Au-199, Au-198, Y-88, and Cu-64 taken with a lithium-drifted germanium detector. All energies are in keV.

transitions were calculated. These calculated energies are compared with the correct energies, as given by References 30, 32, and 33, in Table II-11 under the heading "Calibration Transitions". Again, using the calculated parameters and photopeak positions, the energies of some of the more prominent transitions in Ir-192 were calculated. The results are listed under the heading "Ir-192 Transitions" in Table II-11. These calculated energies agree in all cases with the previous measurements to a few parts in $10^4$. It is worthy of note that all the calculated energies are slightly high. This may be due to the fact that the two calibration transitions of Y-88 are not known with the precision of the other calibration transitions.

### 6.3 Accuracy of the Energy Measurements

There are two major factors limiting the ultimate precision with which gamma-ray energies can be measured using the method described in the previous section. First, the accuracy with which the center of the photopeaks can be determined and second, the accuracy with which the nonlinearity of the AAS can be measured.

In all cases discussed here, the center of the photopeaks have been determined by doing a nonlinear least-squares fit[34] to the five or six highest points in the peak after the underlying Compton distribution has been subtracted. The accuracy of the fit will depend on the total number of counts in the peak and the ratio of the peak height to the intensity of the underlying Compton distribution.

## TABLE II-11

### ENERGY MEASUREMENT[a] OF SOME TRANSITIONS IN THE DECAY OF Ir-192

| Calibration Transitions | | | | | Ir-192 Transitions | | | |
|---|---|---|---|---|---|---|---|---|
| Calculated Energy | Correct Energy | Difference | Error Parts/$10^4$ | Isotope | Calculated Energy | Correct Energy | Difference | Error Parts/$10^4$ |
| 158.32 | 158.366 ± 0.007[b] | 0.04 | 2.8 | Au-199 | 205.79 | 205.74 ± 0.04[e] | 0.05 | 2.4 |
| 411.85 | 411.795 ± 0.009[c] | 0.05 | 1.4 | Au-198 | 295.99 | 295.938 ± 0.009[c] | 0.05 | 1.9 |
| 511.02 | 511.003 ± 0.005[c] | 0.02 | 0.3 | Cu-64 | 308.48 | 308.429 ± 0.010[c] | 0.05 | 1.6 |
| 814.17 | 814.2 ± 0.3[d] | 0.03 | 0.3 | Y-88 | 316.52 | 316.486 ± 0.010[c] | 0.03 | 1.1 |
| 898.20 | 898.2 ± 0.4[d] | 0.00 | 0.0 | Y-88 | 468.13 | 468.053 ± 0.014[c] | 0.08 | 1.6 |
| | | | | | 588.66 | 588.557 ± 0.017[c] | 0.10 | 1.7 |
| | | | | | 604.50 | 604.385 ± 0.017[c] | 0.11 | 1.9 |
| | | | | | 612.56 | 612.435 ± 0.017[c] | 0.12 | 2.1 |

[a] All energies are in keV.

[b] Reference 34.

[c] Reference 32.

[d] Reference 35.

[e] Reference 33.

It is felt that under the best conditions the center of a peak can be determined within 0.05 channels. Under less ideal conditions, for example, a peak-height-to-Compton ratio of 2, the photopeak position can probably not be determined with assurance to better than 0.1 channels.

If an AAS has good stability, then the differential nonlinearity of the system can probably be determined with an accuracy of 0.05 channels in the range of channels from 100 to 1000. Therefore, under good conditions, the channel location of a photopeak corrected for nonlinearity can be determined with an accuracy of about 0.07 channels. Then, for example, with a gain of 1 keV/channel, the energy of a 100-keV gamma ray could be determined with an accuracy of 7 parts in $10^4$. Under less ideal conditions, it should be possible to determine a corrected photopeak position with an accuracy of about 0.11 channels. Using these criteria the 295-, 308-, 316-, and 469-keV transitions of Ir-192 should have been determined with an accuracy of 0.07 keV. Similarly, the 205-, 588-, 604-, and 612-keV transitions should have been determined with an accuracy of 0.11 keV. It can be seen that the first group of transitions have variances from the correct energies ranging from 0.03 to 0.08 keV, and the second group of transitions have variances from 0.05 to 0.12 keV. Thus, in this particular example, the accuracy of the energy determinations is as good as, or slightly better than, those expected. It should be pointed out that the choice of Y-88 was somewhat unfortunate since the quoted errors on its transition energies are not as small as needed for the accuracy desired here.

Of course, the considerations above have not taken into account any systematic errors connected with the equipment. As always, some estimates of these factors must be made for each individual measurement. Another somewhat intangible errors is the accuracy with which the parameters, $\Delta C_1$ and B, are determined. This of course depends on the accuracy with which the photopeak positions and energies of the calibration transitions are known. But, as with all least-squares calculations, the accuracy of $\Delta C_1$ and B will depend strongly on the number of calibration transitions used. Certainly, as a minimal requirement, calibration transitions should be chosen with energies lower and higher than the lowest and highest unknown energies to be determined.

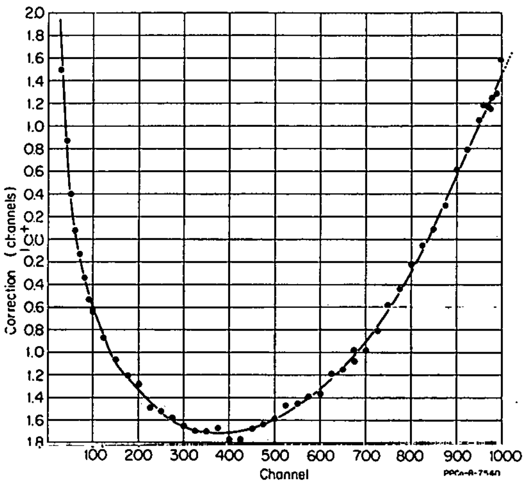

Fig. II-26 A typical linearity correction versus channel plot.

## 6.4 Analysis of Linearity Data

Figure II-26 shows a typical linearity-correction-versus-channel plot. To obtain a functional expression for this data, a power series fit was made. Let $c_i$ be the correction and $x_i$ the channel location of a peak, then the correction is given by

$$c_i = \sum_{n=0}^{N} a_n x_i^n \quad . \qquad (2)$$

Actually, the correction-versus-channel data were broken into two portions, each of which was fit with a function of the type of Equation (2). Thus, more generally, Equation (2) becomes

$$c_i = \sum_{n=0}^{N} a_n^k x_i^n \qquad (3)$$

where k now designates the first or second portion of the curve. In Figure II-26, the data are shown by the points, and the solid line represents the results of the power series fits. In practice, each portion of the curve was fit with different orders, ie, different values of N, and the fit with the smallest residuals chosen as the "best".

## 6.5 Determination of Energy as a Function of the Photopeak Position

Now suppose a Ge(Li) spectrum with many photopeaks is available and that some of these photopeaks correspond to known energies. If the system were perfectly linear, the following relation would hold:

$$E_i = BX_i$$

where $E_i$ is the energy in keV corresponding to the ith photopeak; B is the gain in keV/channel; and $X_i$ is the channel location of the ith photopeak. But the system is not linear. Therefore, suppose the actual location of the ith photopeak is $x_i$. Also, in practice, $C_1$ of Figure II-23 will not correspond to $P_1 = 0$ because the system may not have been set up with the proper adjustment of the "zero" control. Thus, $X_i$ is given by

$$X_i = x_i + A + \sum_{n=0}^{N} a_n^k (A + x_i)^n$$

where $A = -\Delta C_i$ is the correction for "zero shift" and $\sum_{n=0}^{N} a_n^k (A + x_i)^n$

is the correction for nonlinearity. Therefore, the energy corresponding to the photopeak in terms of the actual channel location, $x_i$, is

$$E_i = B \left| x_i + A + \sum_{n=0}^{N} a_n^k (A + x_i)^n \right| \quad . \tag{4}$$

Now if $A << x_i$ ($i = 1$ to $N$), then

$$(A + x_i)^n \approx x_i^n (1 + nA/x_i)$$

and

$$E_i \approx B \left( x_i + A + \sum_{n=0}^{N} a_n^k x_i^n + \sum_{n=0}^{N} a_n^k A\, n\, x_i^{n-1} \right) \tag{5}$$

Taking the photopeaks whose energies are known, the linear least-squares technique can be applied to Equation (5) to find the "best" values of A and B. To do this, minimize the sum of the squares of the residuals,

$$S = \sum_{i=0}^{I} \left| E_i - B\,(x_i + A + \Delta_i + A\alpha_i') \right|^2 . \tag{6}$$

where I is the number of photopeaks corresponding to known energies,

$$\Delta_i = \sum_{n=0}^{N} a_n^k x_i^n , \text{ and } \alpha_i' = \sum_{n=0}^{N} a_n^k\, n\, x_i^{n-1} .$$

Rewriting Equation (6) slightly gives

$$S = \sum_{i=0}^{I} \left| E_i - B\,(D_i + A\alpha_i) \right|^2 \tag{7}$$

where $D_i = x_i + \Delta_i$ and $\alpha_i = 1 + \alpha_i'$.

To minimize Equation (7), take the partial derivative of S with respect to A and B and set them equal to zero. This gives

$$\frac{\partial S}{\partial A} = B \left[ -\sum_{i=0}^{I} E_i\alpha_i + B \sum_{i=0}^{I} D_i\alpha_i + AB \sum_{i=0}^{I} \alpha_i^2 \right] = 0 .$$

B = 0 is not a permissible solution leaving

$$-\sum_{i=0}^{I} E_i\alpha_i + B\sum_{i=0}^{I} D_i\alpha_i + AB\sum_{i=0}^{I} \alpha_i^{2} = 0 \qquad (8)$$

$$\frac{\partial S}{\partial B} = -\sum_{i=0}^{I} E_iD_i - A\sum_{i=0}^{I} E_i\alpha_i + B\sum_{i=0}^{I} D_i^{2} + 2BA\sum_{i=0}^{I} D_i\alpha_i$$

$$+ A^{2}B\sum_{i=0}^{I} \alpha_i^{2} = 0 \qquad (9)$$

Let

$$a = -\sum_{i=0}^{I} E_i\alpha_i \,, b = \sum_{i=0}^{I} D_i\alpha_i \,, c = \sum_{i=0}^{I} \alpha_i^{2}$$

$$d = -\sum_{i=0}^{I} E_iD_i \,, e = \sum_{i=0}^{I} D_i^{2} \,.$$

Solving Equations (8) and (9) gives

$$A = \frac{ae - bd}{cd - ab}$$

$$B = \frac{cd - ab}{b^{2} - ce} \,.$$

Now with these calculated values of A and B, Equation (4) can be used to calculate the energies corresponding to any photopeaks in the spectrum for which the energies were previously unknown.

In some cases, it is possible to say with confidence that A = 0. Then Equation (4) becomes

$$E_i = B\left( x_i + \sum_{n=0}^{N} a_n^{k} \; x_i^{n} \right).$$

Using exactly the same least-squares technique just described, B can be calculated (except now, no approximations are necessary). Carrying out the calculations gives

$$B = \frac{\sum_{i=0}^{I} E_i \alpha_i}{\sum_{i=0}^{I} \alpha_i^2} .$$

A FORTRAN program has been written that performs the calculations just described. The input is the linearity coefficients, $a_n^k$, the energy and channel locations of "known" photopeaks and the channel locations of "unknown" photopeaks. The following calculational options are available: (a) determine values for A and B; (b) set A≡0, and determine the value of B. The output consists of the calculated energies and linearity corrections in all cases and error information in the case of the "known" photopeaks.

## 7. TRANSITIONS OBSERVED IN THE DECAY OF 54-DAY Eu-148

(J. E. Cline, R. G. Helmer)

### 7.1 Introduction

Nuclei in the region between spherical and deformed equilibrium shapes often present interesting, although poorly understood, energy-level structures. The study of the levels of Sm-148, a nuclide within this region, was undertaken at this laboratory[35] through a study of the decay of Pm-148 and Pm-148m. To corroborate the results of this previous study and to obtain additional information on the level structure, a study has been undertaken of the decay of 54-day Eu-148.

Several previous studies of the decay of the Eu-148 nuclide have been reported in recent years[36,37,38,39]. There are significant differences between these reported level schemes. The present work, done since the advent of lithium-drifted germanium detectors, has indicated the presence of over 100 gamma-ray transitions as opposed to the 27 transitions reported in Reference 39. Due to the superior resolution of the new devices, many of the previously reported transitions have been revealed to be multiplets.

The following is a discussion of this investigation and a presentation of a tentative level scheme which incorporates about half of the observed transitions.

### 7.2 Experimental Measurements

7.21 Source Preparation. Sources of Eu-148 were produced by (p, 2n) reactions on samples of $Sm_2O_3$, enriched to 99 percent in Sm-149. Irradiations were performed in the 22-MeV proton beam of the ORNL cyclotron. Samples were purified by rare-earth chemistry followed by an ion-exchange column separation with $\alpha$-hydroxyisobutyric acid as the eluting agent. A slight contaminant of 24-day Eu-147 was observed in each sample. No evidence of the presence of 120-day Eu-149 or any other nuclide has appeared after six months.

Sources for the internal-conversion-electron spectrographs were made by electroplating the europium onto a 0.006-inch-diameter platinum wire.

7.22 Gamma-Ray Measurement.

(1) Singles Measurements. Figures II-27 and -28 show spectra of the gamma radiation from the decay of Eu-148 taken with a 4-mm-thick by 2.5-$cm^2$, lithium-drifted germanium detector. This detector had a resolution of ≈2 keV at 100 keV and ≈ 3 keV at 1 MeV. It was cooled to ≈ 78°K and was used in conjunction with a low-noise preamplifier incorporating a field-effect transitor in the first stage. Energy calibration of the spectra was accomplished by the method of internal comparison using sources of Bi-207 and of Th-228 in equilibrium with its daughters. The nonlinearity of the 1024-channel multichannel analyzer was carefully determined using a precision pulser and was taken into account in the energy determinations. Energy measurements below 1 MeV have previously been found to be accurate to within ± 0.2 keV using this method. Due to the lack of a good "window-amplifier", it was necessary to record the high-energy

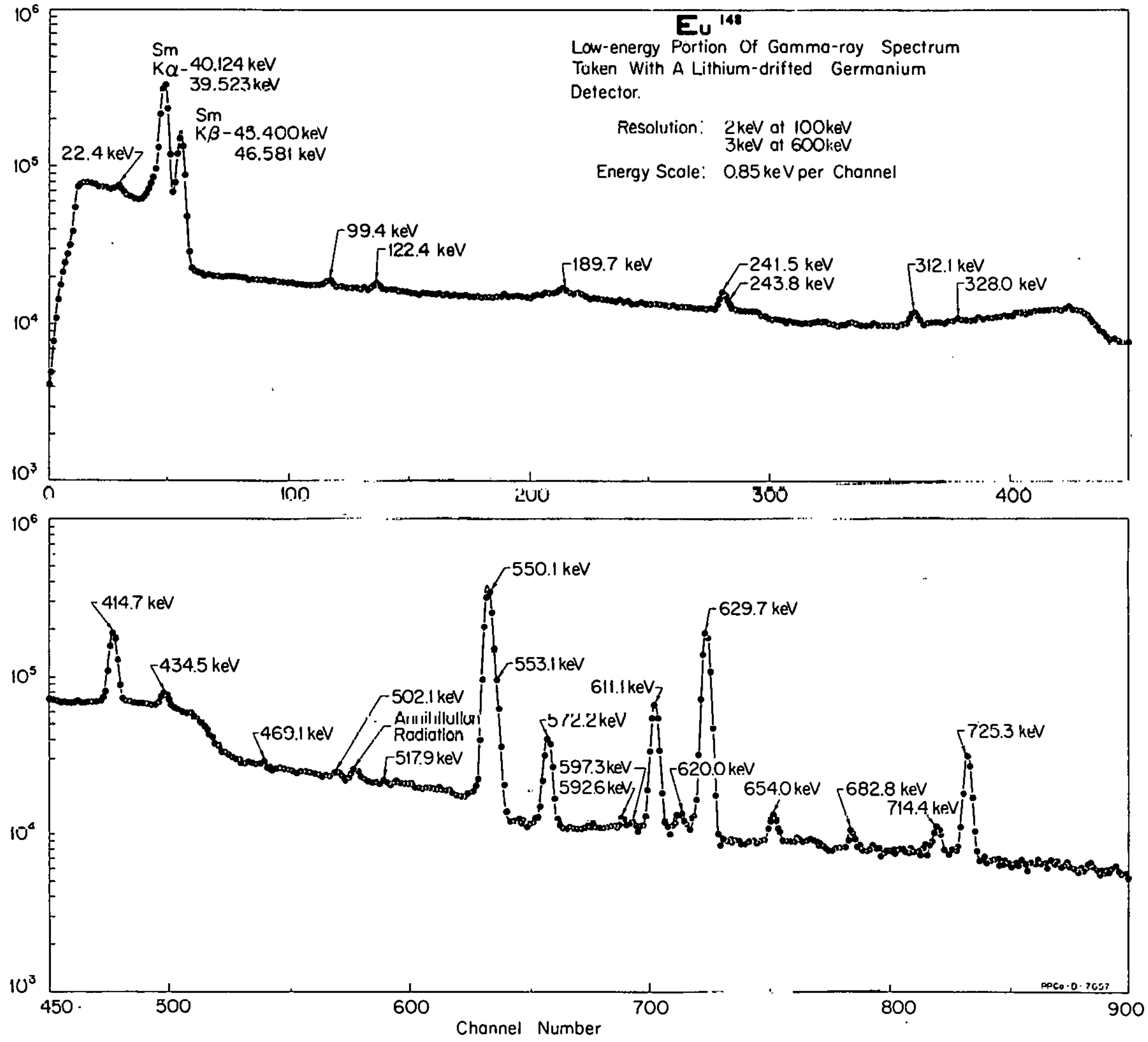

Fig. II-27 Low-energy portion of gamma-ray spectrum taken with 4-mm by 2.5-$cm^2$ Ge(Li) detector.

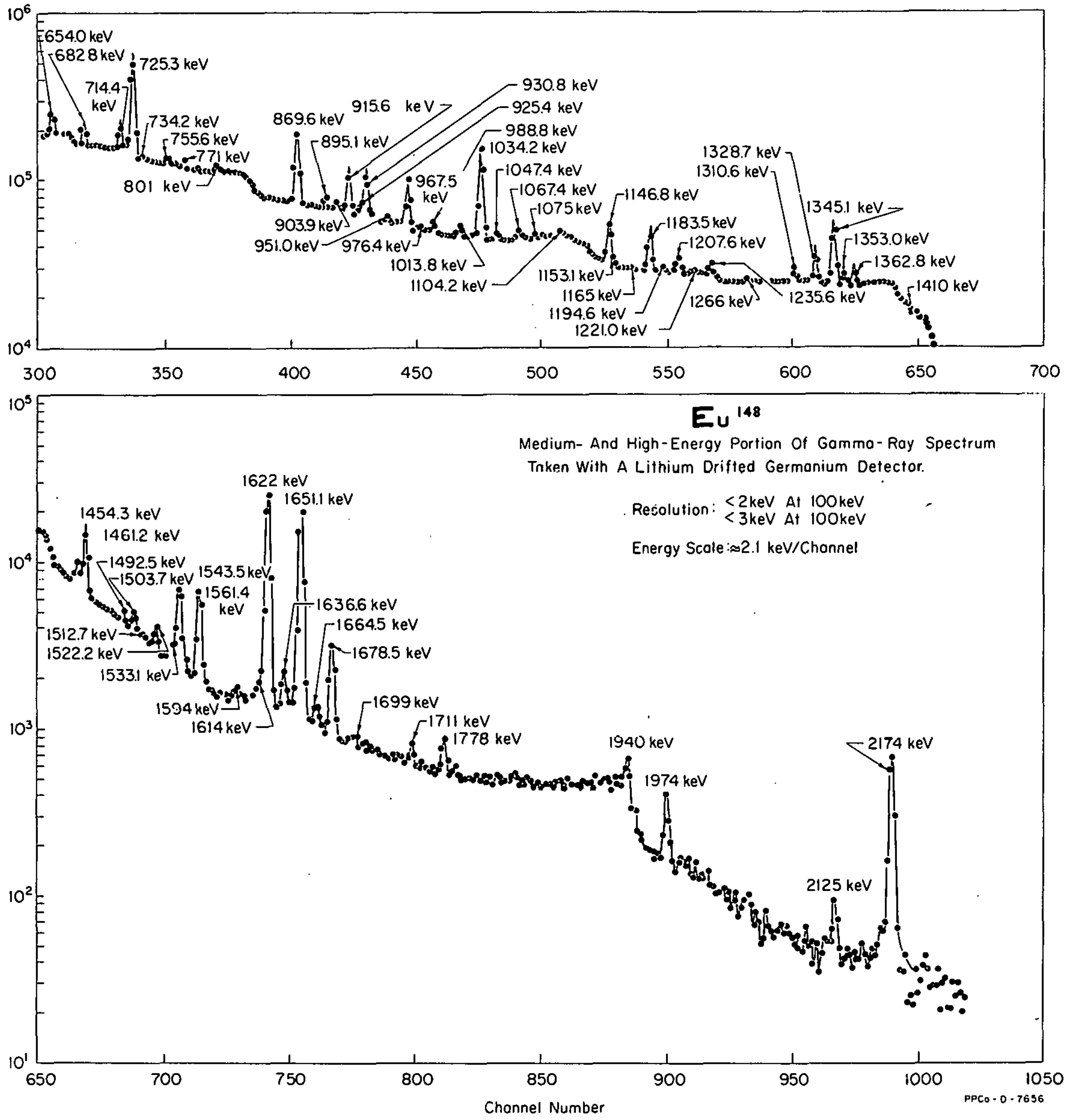

Fig. II-28 High-energy portion of gamma-ray spectrum taken with 4-mm by 2.5-cm$^2$ Ge(Li) detector.

spectra (ie, > ≈ 1800 keV) on a rather coarse energy scale (>2 keV/channel). This, as well as the relative unavailability of calibration standards for high-energy gamma rays and the comparatively large effects of analyzer nonlinearity in the high channels, has temporarily limited the precision of the energy measurements of the gamma rays above 1800 keV to about ± 1 keV.

Since the efficiency of the germanium detectors as a function of energy of the incident photons for detecting an event in the photopeak is rather poorly understood at this time, intensities for the transitions observed were not obtained in the main from these data. Rather, these data were used in conjunction with data taken using a 3- by 3-inch NaI(Tl) spectrometer. Such a spectrum is presented in Figure II-29. These data were taken at a source-detector distance

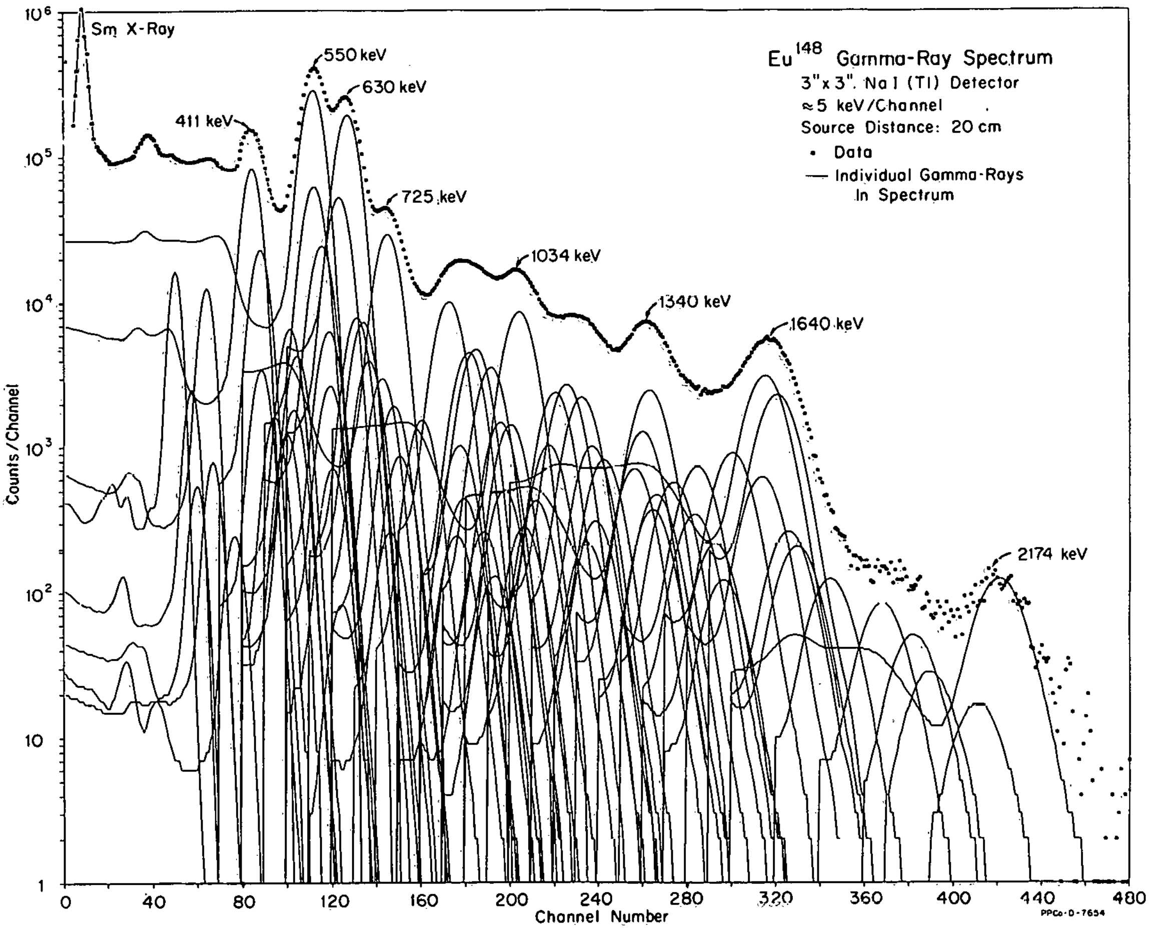

Fig. II-29 Gamma-ray spectrum taken with 3- by 3-inch NaI(Tl) detector. Solid curves represent components of "stripped" spectrum.

of 20 cm. This was done to reduce the effects of coincidence summing to a negligible level. The determination of relative intensities then proceeded as follows: It was felt that over small regions of energy (ie, ≈ 100 keV), relative detection efficiencies for the germanium detector could be determined from the interpolated[40] photoelectric cross-sections for germanium. Thus, the relative intensities of all the transitions observed over such a range in the spectra taken with the germanium detector were determined. Using these relative intensities and the gamma-ray energies, the spectrum of gamma radiation taken with the NaI(Tl) detector was fit. This fit was carried out by a nonlinear least-squares fitting routine[41] and an IBM 7040 computer. Due to the extreme complexity of the gamma-ray spectrum, the precision of the results of this fit is not up to usual standards (ie, those reported in Reference 41). Absolute intensities for the transitions were obtained by assuming that all decays proceeded through a level at 550.1 keV, an assumption which appeared justified by coincidence measurements described below. The intensities and positions of the individual gamma rays as determined by the fit are also shown in Figure II-29.

Table II-12 presents a listing of the transition energies observed in this work and the absolute intensities for each transition. Included in this tabulation

# TABLE II-12

## LIST OF OBSERVED TRANSITION ENERGIES, INTENSITIES, CONVERSION-ELECTRON INTENSITIES, MEASURED CONVERSION COEFFICIENTS, AND PROPOSED MULTIPOLARITY ASSIGNMENTS

| | $E_\gamma$ (keV) | | | $I_\gamma$ | $I_c$ (percent of decays) | | | | | | | | Multipolarity Assignments | |
|---|---|---|---|---|---|---|---|---|---|---|---|---|---|---|
| | | | | | Si(Au) | | Magnetic Spectrometer | | | | | | | |
| | Ge(Li) | Magnetic Spectrograph | "Best Value" | Percent of Decays | K | L | K | L | M | N | $\alpha_K$ | $\alpha_L$ | This Experiment | Reference 42 |
| 1 | 22.4 | 22.41 | 22.41 ± 0.10 | | | | | 0.4 | 0.3 | 0.1 | | | | |
| 2 | 67.4 | 66.63 | 66.63 ± 0.10 | | | | | | | | | | | |
| 3 | 99.4 | 98.35 | 98.35 ± 0.10 | | | | 0.13 | 0.023 | | | | | | |
| 4 | 122.4 | 121.18 | 121.18 ± 0.12 | | | | 0.02 | | | | | | | |
| 5 | 168.4 | 166.14 | 166.14 ± 0.17 | | | | 0.03 | | | | | | | |
| 6 | | 182.74 | 182.74 ± 0.18 | | | | | | | | | | | |
| 7 | 189.7 | 189.68 | 189.68 ± 0.19 | | | | 0.045 | | | | | | | |
| 8 | | 215.94 | 215.9 ± 0.2 | | | | | | | | | | | |
| 9 | 242.5 | 241.51 | 241.5 ± 0.2 | 1.7 ± 0.4 | 0.17 | | 0.21 | 0.03 | | | 0.11 | 0.02 | | |
| 10 | | 243.8 | 243.8 ± 0.3 | | | | 0.03 | | | | | | | |
| 11 | | 252.50 | 252.5 ± 0.2 | | | | | | | | | | | |
| 12 | 278.4 | 277.00 | 277.0 ± 0.3 | $0.3 \pm^{0.3}_{0.2}$ | | | 0.02 | | | | 0.07 | | | |
| 13 | 289.3 | 288.03 | 288.0 ± 0.3 | $0.7 \pm^{0.5}_{0.3}$ | | | 0.04 | | | | 0.06 | | | |
| 14 | | 296.01 | 296.0 ± 0.3 | | | | | | | | | | | |
| 15 | | 310.1 | 310.1 ± 0.3 | | | | | | | | | | | |
| 16 | 312.1 | 311.6 | 311.6 ± 0.3 | 1.8 ± 0.4 | 0.03 | | 0.02 | | | | 0.014 | | E1 | E1 |
| 17 | | 319.2 | 319.2 ± 0.3 | | | | | | | | | | | |
| 18 | 328.0 | 327.6 | 327.6 ± 0.3 | $0.1 \pm^{0.1}_{0.05}$ | | | 0.02 | | | | 0.2 | | M2 | |
| 19 | | 377.5 | 377.5 ± 0.5 | | | | | | | | | | | |
| 20 | 414.7 | 414.0 [a] | 414.0 ± 0.4[a] [43] | 19.3 ± 2.0 | 0.09[a] | | 0.08[a] | | | | 0.010 | | E1 | E1 |
| 21 | | | 413.5 ± 1.0[a] [44] | | 0.22[a] | | 0.20[a] | | | | 0.021 | | E2 | E2 |
| 22 | 434.5 | 433.0 | 433.0 ± 0.4 | 2.8 ± 0.4 | 0.05 | | | | | | 0.018 | | E2 | E2 |
| 23 | | 437.0 | 437.0 ± 0.4 | 0.8 ± 0.5 | | | | | | | | | | |
| 24 | 469.1 | 468.4 | 468.4 ± 0.4 | $0.4 \pm^{0.4}_{0.2}$ | 0.02 | | | | | | 0.05 | | M1 or M2 | |
| 25 | 496.2 | 495.5 | 495.5 ± 0.4 | $0.4 \pm^{0.4}_{0.2}$ | 0.01 | | | | | | 0.03 | | M1 | |
| 26 | 502.1 | 501.3 | 501.3 ± 0.5 | $0.4 \pm^{0.4}_{0.2}$ | | | | | | | | | | |
| 27 | 510.6 (annihilation radiation) ⟶ | | | | | | | | | | | | | |
| 28 | 517.9 | 518.4 | 518.4 ± 0.5 | $0.4 \pm^{0.4}_{0.2}$ | | | | | | | | | | |
| 29 | 550.8 | 550.1 | 550.1 ± 0.4 | 100.0 | 1.03 | 0.18 | 0.90 | 0.14 | 0.04 | 0.01 | 0.009 | 0.0019 | E2 | E2 |
| 30 | | 553.1 | 553.1 ± 0.4 | 21.0 ± 2.0 | | | 0.20 | 0.04 | | | 0.009 | 0.0019 | E2 | E2 |
| 31 | 572.2 | 571.8 | 572.0 ± 0.4 | 8.6 ± 1.0 | 0.023 | | 0.026 | | | | 0.003 | | E1 | |
| 32 | 592.6 | | 592.6 ± 0.5 | $0.3 \pm^{0.2}_{0.1}$ | | | 0.010 | | | | 0.03 | | M1 or M2 | |
| 33 | 597.3 | 596.8 | 597.0 ± 0.4 | $0.2 \pm^{0.2}_{0.1}$ | | | | | | | | | | |
| 34 | 611.1 | 611.1 | 611.1 ± 0.4 | 19.8 ± 2.0 | 0.04 | | 0.05 | 0.005 | | | 0.0025 | 0.0003 | E1 | E1 |
| 35 | 620.0 | 620.0 | 620.0 ± 0.5 | 0.6 ± 0.3 | | | | | | | | | | |
| 36 | 629.7 | 629.7 | 629.7 ± 0.4 | 76 ± 3 | 0.465[b] | 0.077 | 0.465[b] | 0.068 | 0.022 | | 0.0061 | 0.0009 | E2[b] | E2[b] |
| 37 | | 630.9 | 630.9 ± 0.6 | | | | | | | | | | | |
| 38 | 654.0 | 653.9 | 653.9 ± 0.4 | 3.3 ± 0.4 | 0.025 | | 0.020 | 0.006 | | | 0.007 | 0.002 | E2(M1) | |
| 39 | 682.8 | 682.9 | 682.9 ± 0.4 | 1.8 ± 0.3 | 0.009 | | 0.012 | | | | 0.006 | | E2(M1) | |
| 40 | 714.4 | 714.3 | 714.3 ± 0.4 | 2.4 ± 0.3 | 0.019 | 0.005 | 0.016 | | | | 0.007 | 0.002 | M1(E2) | E1 |
| 41 | 725.3 | 725.2 | 725.2 ± 0.3 | 14.4 ± 1.0 | 0.054 | 0.01 | 0.066 | 0.01 | | | 0.004 | 0.0007 | E2 | E2 |
| 42 | 734.2 | 734.3 | 734.3 ± 0.7 | $0.1 \pm^{0.1}_{0.05}$ | | | | | | | | | | |
| 43 | 755.6 | 756 | 755.8 ± 0.6 | 0.5 ± 0.3 | | | | | | | | | | |
| 44 | 771 | | 771 ± 1 | | | | | | | | | | | |
| 45 | 801 [c] | | 801 ± 1 | | | | | | | | | | | |
| 46 | | 816.8 | 816.8 ± 0.8 | | | | | | | | | | | |
| 47 | 869.6 | 869.3 | 869.5 ± 0.3 | 6.6 ± 0.6 | 0.015 | 0.004 | 0.018 | | | | 0.0024 | 0.0006 | E2 | E2 |
| 48 | 895.1 | 895.0 | 895.0 ± 0.4 | 0.7 ± 0.3 | 0.003 | | | | | | 0.004 | | E2(M1) | |
| 49 | 903.9 | 904.0 | 904.0 ± 0.3 | 0.3 ± 0.2 | | | | | | | | | | |
| 50 | 915.0 | 914.6 | 914.8 ± 0.3 | 3.2 ± 0.3 | 0.006 | 0.0012 | | | | | 0.0019 | 0.0004 | (E2) | E2 |
| 51 | 925.4 | | 925.4 ± 0.5 | | | | | | | | | | | |
| 52 | 930.8 | 931.2 | 931.0 ± 0.3 | 3.4 ± 0.3 | 0.005 | | | | | | 0.0015 | | (E1) | M1, E2 |
| 53 | 951.0 | | 951.0 ± 1.0 | $0.2 \pm^{0.2}_{0.1}$ | | | | | | | | | | |
| 54 | | 954.8 | 954.8 ± 1.0 | | | | | | | | | | | |
| 55 | 967.3 | 967.5 | 967.4 ± 0.4 | 2.7 ± 0.4 | 0.006 | | | | | | 0.0022 | | E2 | E2 |
| 66 | 976.4 | 975.1 | 975 ± 1 | $0.1 \pm^{0.1}_{0.05}$ | | | | | | | | | | |

## TABLE II-12 (Cont.)

### LIST OF OBSERVED TRANSITION ENERGIES, INTENSITIES, CONVERSION-ELECTRON INTENSITIES, MEASURED CONVERSION COEFFICIENTS, AND PROPOSED MULTIPOLARITY ASSIGNMENTS

| | $E_\gamma$ (keV) | | | $I_\gamma$ | $I_c$ (percent of decays) | | | | | | | | Multipolarity Assignments | |
|---|---|---|---|---|---|---|---|---|---|---|---|---|---|---|
| | | | | | Si(Au) | | Magnetic Spectrometer | | | | | | | |
| | Ge(Li) | Magnetic Spectrograph | "Best Value" | Percent of Decays | K | L | K | L | M | N | $\alpha_K$ | $\alpha_L$ | This Experiment | Reference 42 |
| 57 | 989.8 | 990.1 | 989.9 ± 0.4 | 0.6 ± 0.3 | 0.0007 | | | | | | 0.0012 | | E-1 | |
| 58 | 1000 | 999.3 | 999.6 ± 1.0 | 0.4 ± 0.3 | | | | | | | | | | |
| 59 | 1013.8 | 1014.2 | 1014.0 ± 0.4 | 1.0 ± 0.3 | 0.0011 | | | | | | 0.0011 | | E1 | |
| 60 | 1034.2 | 1034.2 | 1034.2 ± 0.3 | 7.3 ± 0.6 | 0.013 | | | | | | 0.0018 | | E2 | E2 |
| 61 | 1047.4 | | 1047.4 ± 0.5 | | | | | | | | | | | |
| 62 | 1067.4 | | 1067.4 ± 0.5 | | | | | | | | | | | |
| 63 | 1075 | 1074.2 | 1074.5 ± 1.0 | | | | | | | | | | | |
| 64 | 1080.4 | | 1088.4 ± 0.5 | | | | | | | | | | | |
| 65 | 1104.2 | 1104.5 | 1104.3 ± 0.3 | 0.8 ± 0.4 | | | | | | | | | | |
| 66 | 1146.8 | 1147.1 | 1146.9 ± 0.4 | 2.7 ± 0.3 | 0.002 | | 0.006 | | | | 0.0014 | | E2 | E2 |
| 67 | 1153 | | 1153 ± 1.0 | | | | | | | | | | | |
| 68 | 1165 | | 1165 ± 1.0 | | | | | | | | | | | |
| 69 | 1183.5 | 1183.8 | 1183.6 ± 0.4 | 2.3 ± 0.3 | 0.0014 | | | | | | 0.0006 | | E1 or E2 | E2 |
| 70 | 1194.6 | 1194.7 | 1194.6 ± 0.4 | 0.2 ± 0.1 | | | | | | | | | | |
| 71 | 1207.6 | 1208.0 | 1207.8 ± 0.4 | 1.1 ± 0.2 | | | | | | | | | | |
| 72 | 1221 | 1222.3 | 1222.0 ± 1.0 | 0.3 ± 0.2 | | | | | | | | | | |
| 73 | 1235.6 | | 1235.6 ± 0.5 | 0.9 ± 0.2 | | | | | | | | | | |
| 74 | 1266 | | 1266 ± 2 | | | | | | | | | | | |
| 75 | 1310.6 | 1310.8 | 1310.7 ± 0.4 | 0.9 ± 0.3 | | | | | | | | | | |
| 76 | 1328.7 | 1329.0 | 1328.8 ± 0.4 | 1.2 ± 0.2 | | | | | | | | | | |
| 77 | 1345.1 | 1345.0 | 1345.1 ± 0.4 | 3.0 ± 0.3 | 0.002 | 0.0004 | 0.003 | | | | 0.0008 | 0.0001 | E1 or E2 | E2 |
| 78 | 1353.0 | 1354.5 | 1354 ± 1 | 0.5 ± 0.3 | | | | | | | | | | |
| 79 | 1362.0 | 1363.6 | 1363.2 ± 0.4 | 0.6 ± 0.3 | | | | | | | | | | |
| 80 | 1410 | | 1410 ± 1 | | | | | | | | | | | |
| 81 | 1454.3 | 1453.5 | 1453.9 ± 0.4 | 0.5 ± 0.3 | | | | | | | | | | |
| 82 | 1461.2 | 1461.4 | 1461.3 ± 0.4 | 1.1 ± 0.2 | | | | | | | | | | |
| 83 | 1492.5 | | 1492.5 ± 0.6 | | | | | | | | | | | |
| 84 | 1503.7 | | 1503.7 ± 0.6 | 0.3 ± 0.2 | | | | | | | | | | |
| 85 | 1512.7 | | 1512.7 ± 1.0 | | | | | | | | | | | |
| 86 | 1522.2 | | 1522.2 ± 0.6 | 0.2 ± 0.1 | | | | | | | | | | |
| 87 | 1535 | | 1535 ± 2 | | | | | | | | | | | |
| 88 | 1543.5 | 1543.8 | 1543.6 ± 0.4 | 1.4 ± 0.2 | | | | | | | | | | |
| 89 | 1561.4 | 1561.2 | 1561.3 ± 0.4 | 1.0 ± 0.2 | | | | | | | | | | |
| 90 | 1594.0 | | 1594.0 ± 1 | | | | | | | | | | | |
| 91 | 1614 | | 1614 ± 1 | | | | | | | | | | | |
| 92 | 1622.1 | 1621.6 | 1621.8 ± 0.3 | 5.3 ± 0.5 | 0.0012 | | 0.003 | | | | 0.0004 | | E1 | E1 |
| 93 | 1636.6 | | 1636.6 ± 0.6 | 0.4 ± 0.1 | | | | | | | | | | |
| 94 | 1651.1 | 1650.6 | 1650.8 ± 0.3 | 4.0 ± 0.4 | 0.0012 | | 0.002 | | | | 0.0004 | E1 | M1 |
| 95 | 1664.5 | | 1664.5 ± 0.6 | 0.2 ± 0.1 | | | | | | | | | | |
| 96 | [illegible] | [illegible] | [illegible] ± 0.6 | 0.6 ± 0.2 | | | | | | | | | | |
| 97 | 1699 | | 1699 ± 1 | 0.05 ± 0.03 | | | | | | | | | | |
| 98 | 1749 | | 1749 ± 2 | 0.1 ± 0.05 | | | | | | | | | | |
| 99 | 1778 | | 1778 ± 2 | 0.2 ± 0.05 | | | | | | | | | | |
| 100 | 1902 [d] | | 1902 ± 5 | 0.03 ± 0.03 | | | | | | | | | | |
| 101 | 1940 | | 1940 ± 2 | 0.2 ± 0.05 | | | | | | | | | | |
| 102 | 1974 | | 1974 ± 2 | 0.2 ± 0.05 | | | | | | | | | | |
| 103 | 2125 | | 2125 ± 2 | 0.04 ± 0.02 | | | | | | | | | | |
| 104 | 2174 | | 2174 ± 2 | 0.4 ± 0.1 | | | | | | | | | | |

---

[a] Identification and division as two transitions were made by coincidence studies and by a knowledge of the E1 component from studies of Pm-148 decay (Reference 42).

[b] Basis of intensity normalization of electron intensities.

[c] 1st identified as a requirement of the fit to the NaI data -- later observed in Ge(Li) data.

[d] Identification as a requirement of the fit to the NaI data.

are the results from conversion-electron studies which will be described below. All gamma-rays reported in this work have about a 54-day half-life and are, thus, assumed to be associated with the decay of Eu-148. The intensities which are listed in Table II-12 are based upon all available information and not solely upon values obtained from the fit to the data from NaI. They are the values which are felt to be the "best" values and the reliability of these values is reflected in the uncertainties assigned to them. The uncertainties are highly subjective.

(2) Gamma-Gamma Coincidence Measurements. Gamma-Gamma coincidence measurements were carried out using a 256- by 256-channel multiparameter analyzer. Two types of measurments were carried out. One of these used two 3- by 3-inch NaI(Tl) detectors, each located 10 cm from the source. The two detectors were located at 90 deg with respect to one another, and a shield was placed between the detectors to reduce the effects of Compton scattering of gamma rays from one detector into the other. The other set of measurements used a 2.5-cm$^2$ by 2-mm germanium detector in place of one of the NaI detectors.

In a decay scheme which is as complicated as this, the information which can be obtained from coincidence measurements is usually quite limited. This is particularly the case where NaI detectors are used with their attendant relatively poor resolution characteristics (ie, relative to germanium detectors) in order to obtain reasonable coincidence counting rates. In this particular case, previous studies[35,36,42] of the level structure of Sm-148 through the decay of Pm-148 furnish aid. In the Pm-148 studies, it has been well established that the first three excited levels lie at 550, 1162, and 1180 keV. The latter two states decay via 612- and 630-keV transitions to the 550-keV level. Since these three transitions are strongly present in the radiations from Eu-148, much information can be obtained through a careful analysis of the spectra coincident with these transitions.

Figures II-30 through -33 present some of the more pertinent spectra which were obtained from coincidence measurements. In all of these data, it is

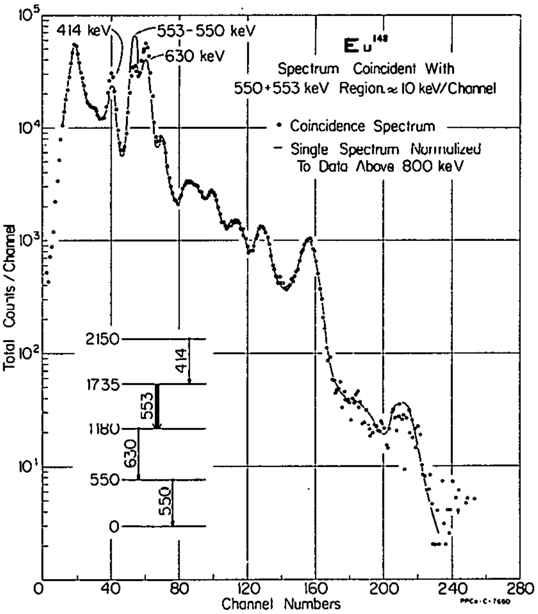

Fig. II-30 Gamma-gamma coincidence spectrum showing coincidences with 550- + 553-keV transitions. Gating detector is Ge(Li).

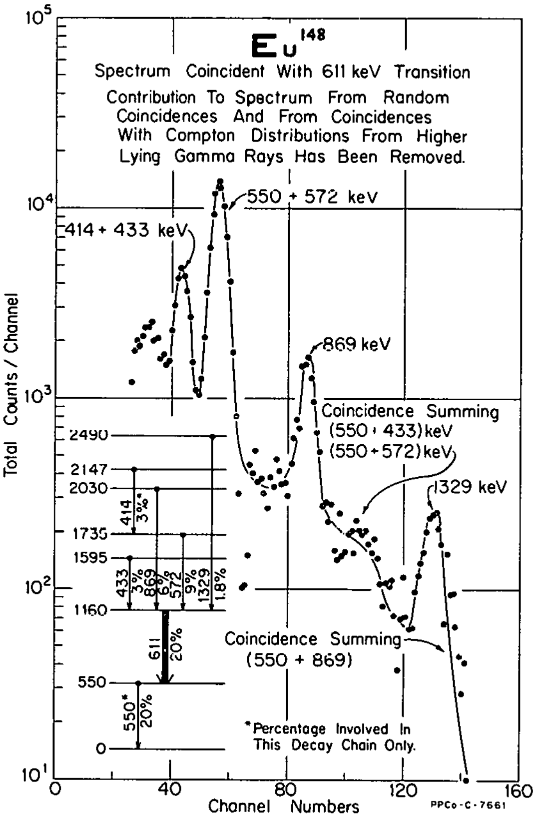

Fig. II-31 Spectrum of gamma rays coincident with 611-keV transition. Gating detector is Ge(Li).

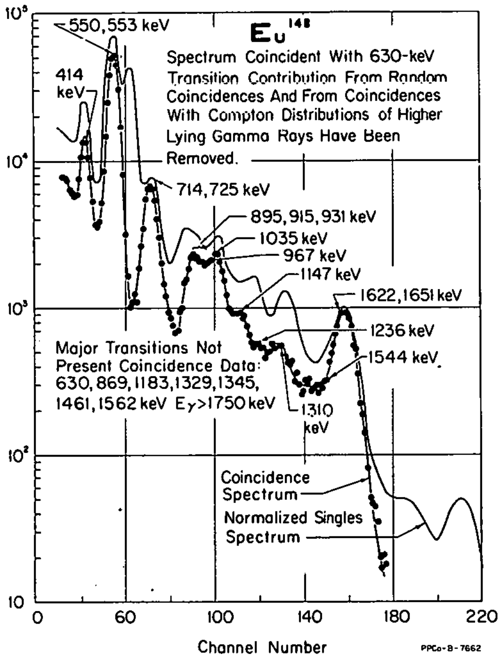

Fig. II-32 Spectrum of gamma radiation coincident with 630-keV transition. Gating detector is Ge(Li).

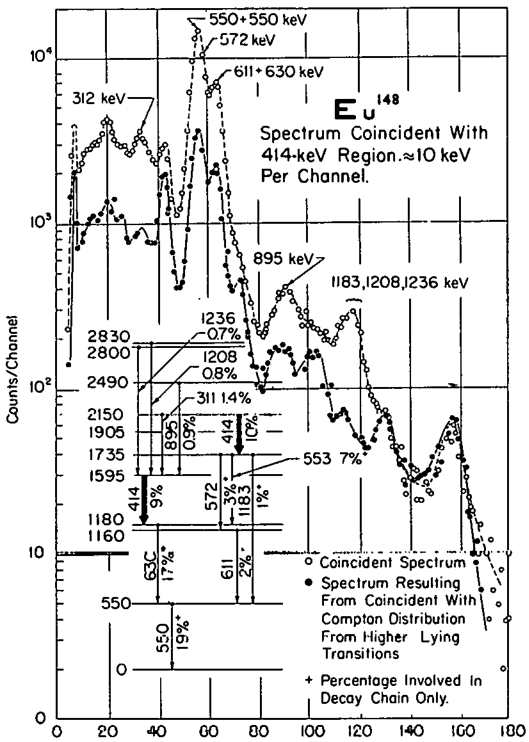

Fig. II-33 Spectrum of gamma rays coincident with 414-keV transitions. Gating detector is NaI(Tl).

the spectrum from the NaI(Tl) detector that is presented. Figure II-30 shows the spectrum coincident with the unresolved 550 + 553 keV transitions. The gating detector in this case was the germanium detector. The intensity of these two transitions was such that the contribution to the spectrum from coincidences with the underlying Compton distribution from higher lying transitions was negligible. Shown also on the figure is a singles spectrum which is normalized to the region above 800 keV. It is noticed that there is no appreciable difference between these two curves except in the region from 400 to 650 keV. This is interpreted to mean that so far as can be determined, all transitions proceed through the first excited level at 550 keV and that the enhancement of the 630- and 414-keV transitions in the coincidence spectrum represent coincidences with the 553-keV transition. This interpretation also accounts for the presence of the peak at 550 keV. A partial decay scheme is included in the figure showing the placement of the 553-keV transition along with the transitions observed to be coincident with it. Intensity considerations as well as other coincidence measurements indicated the order of the 553- and 414-keV transitions.

Figure II-31 presents the spectrum coincident with the 611-keV transition. Again, the gating detector was lithium-drifted germanium. Contributions to the spectrum from both random coincidences and coincidences with Compton distributions were determined and removed from the spectrum before plotting. An intensity analysis was then performed on the data to determine which gamma rays were present and the relative intensities. These relative intensities were then normalized to the absolute intensity of the 611-keV transition, and the following results were obtained: $I_{550+572} \approx 29$ percent, $I_{414+572} \approx 6.5$ percent, $I_{869} \approx 6$ percent, and $I_{1329} \approx 1.8$ percent. In the case of the 1329-keV transition, it was this intensity which identified the peak at ≈ 1330 keV as this transition rather than the stronger 1345-keV transition. Figure II-32 shows a spectrum of radiations coincident with the 630-keV transition. The gating detector was germanium. Contributions to this spectrum from random coincidences and coincidences with Compton distributions have been removed. The spectrum was analyzed for the energies and intensities of its constituents by the method of Reference 41, and the results are given in Table II-13 (normalized to the intensity of the 630-keV transition). Included in the figure is a singles spectrum normalized in intensity to the peak at 1630 keV. From an analysis of the difference between the two spectra, it was established which major transitions were missing from the coincidence spectrum. These missing transitions which are listed on the figure are presumed to directly populate the 550- or 1162-keV levels.

## TABLE II-13

### INTENSITY AND COMPONENTS RESULTING FROM FIT OF DATA COINCIDENT WITH 630-keV TRANSITION

| $E_\gamma$ (keV) | $I_\gamma$ (percent) | $I_\gamma$ - Singles Analysis (percent) |
|---|---|---|
| 414 | 13 | ≈ 16[a] |
| (550 + 553) | 99 | 100[a] |
| (714 + 725) | 16 | 16.8 |
| (895 + 915 + 930) | 6 | 7.5 |
| (1013 + 1034) | 9 | 8.3 |
| 1147 | 3 | 2.7 |
| 1236 | 1 | 0.9 |
| 1310 | 1 | 0.9 |
| 1544 | 1 | 1.4 |
| (1622 + 1651) | 10 | 9.3 |

---

[a] Intensity observed in this decay chain only.

Figure II-33 shows a spectrum taken in coincidence with a 10-keV wide energy region centered about 415 keV. The gating detector in this instance was an NaI(Tl) detector. Shown also is a spectrum taken in coincidence with a 10-keV region in the valley between the 415- and the 315-keV peaks. This latter spectrum is taken to represent coincidences with the underlying Compton distribution. An analysis of the difference between these two spectra yielded the following transitions and intensities (normalized to the intensity of the 414-keV transitions): $I_{311}$ = 1.4 percent, $I_{550+553+572}$ = 29 percent, $I_{611+630}$ = 19 percent, $I_{895}$ = 0.9 percent, and $I_{1183+1208+1236}$ = 2.3 percent. The interpretation is shown in the figure.

7.23 Conversion-Electron Measurement. Measurements of the conversion-electron spectra from the decay of Eu-148 were made using both silicon surface-barrier detectors and 180-deg permanent-magnet electron spectrographs. Figure II-34 shows a spectrum of electrons taken with a 1.2-mm-thick by

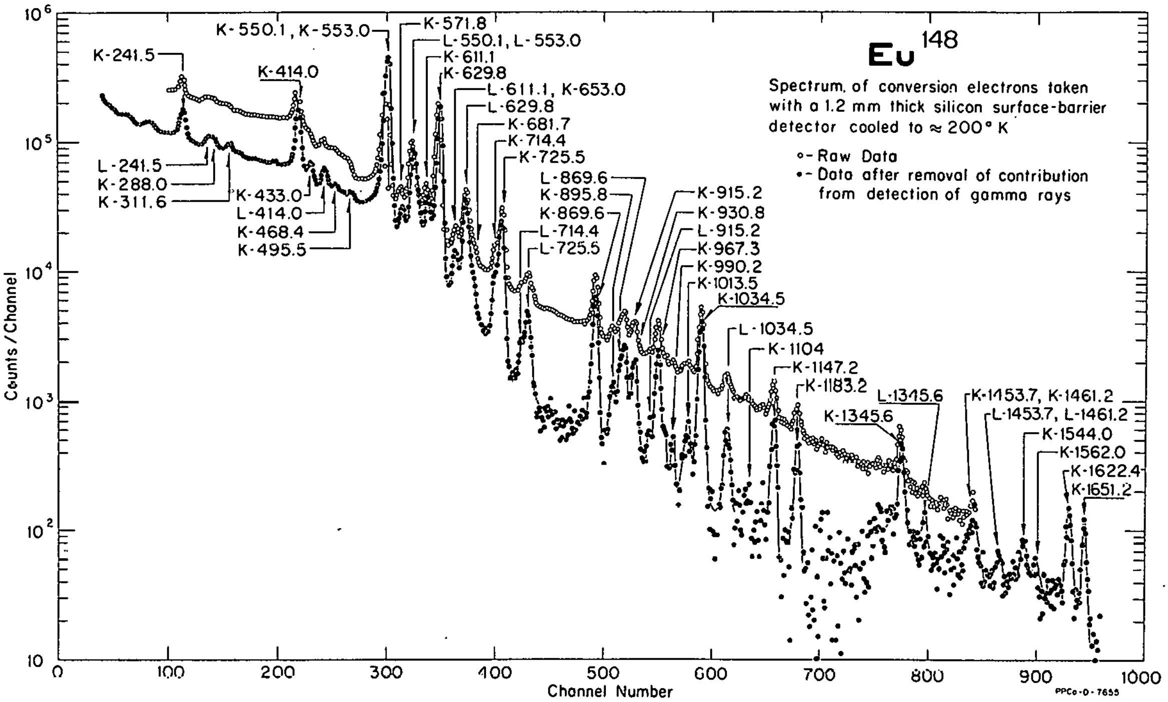

Fig. II-34 Spectrum of conversion electrons taken with 1.2-mm by 1-$cm^2$ Si(Au) detector.

1-$cm^2$, surface-barrier detector. This detector was cooled to ≈ 200°K through the use of a mixture of ethyl alcohol and dry ice. The resolution of the device when operated at this temperature was about 7 keV (FWHM). The top curve shows the data which include the gamma-ray response of the detector while the lower curve shows the same data with the gamma-ray contribution removed. This removal was accomplished by interposing a 0.5-g/$cm^2$ Be absorber between the source and detector and subtracting for a length of time equivalent to the initial counting period.

The counting characteristics of this detector have been previously studied. Relative peak efficiencies have been obtained as a function of electron energy, through the use of calibrated sources. For electron enegies where the range of the electron is less than the 1.2-mm depletion depth of the detector (ie, < ≈ 700 keV), the relative efficiencies are felt to be accurate to within 2 percent. This uncertainty becomes correspondingly higher when the range exceeds the thickness, approaching about 20 percent for electron energies of ≈ 1600 keV. With these measured efficiencies, the data of Figure II-34 were analyzed for energies and relative intensities of the lines which were observed. These intensity values were then normalized to the absolute intensities of the gamma rays listed in Table II-12 by assuming that the 630-keV transition is of pure E2 character and by using the theoretical conversion coefficient as given by Sliv[43]. This assumption has its justification from the studies[42] of this transition in the decay of Pm-148. The results are included in Table II-12.

The internal-conversion electrons were also observed photographically with the set of 180-deg, magnetic spectrographs. These data were used to identify the transitions that were present as well as to determine their energies and some electron intensities. The energy calibration of three of these spectrographs has been described[44]. The fourth magnet, which spans the energy range of 0.05 to 2.2 MeV, was calibrated for this study. Lines of Ir-192 from 0.2 to 0.6 MeV were used along with those of Co-60 at 1.1 and 1.3 MeV. Although the regions from 0.6 to 1.1 and above 1.3 MeV were not calibrated, it is believed that the measured energies should be accurate to 0.1 percent as is the case for the other spectrographs.

The decay of the Eu-148 source has been followed for five months. All the conversion lines decay with the same half-life except those from 24-day Eu-147. The energies of the transitions deduced from these lines are shown in Table II-12.

Some relative conversion-line intensities were also determined from these spectrograph plates. Although this method suffers from the inaccuracies of photographic detection, it does have the advantage over the silicon detector of higher resolution. For this set of plates, it was assumed[45] that

$$\log I_o/I = C \log (\alpha E + 1)$$

where E is the exposure (in electrons-cm$^{-2}$ or proportional units), $I_o$ is the light intensity transmitted through an unexposed portion of plate, I is light intensity at any exposed portion, $\alpha$ is a scaling factor which can be taken as unity, and C is a constant to be determined. The quantity, $\log I_o/I$, is the optical density, and it was determined by scanning the lines with a microphotometer. From the exposure times, the relative values of E for each plate is computed. The value of C which best fits the calculated ratios of E and the measured $\log I_o/I$ values for several lines were then computed and used to calculate the relative line exposures. The relative intensities were then calculated by use of these relative exposures, the "rectangular approximation" of Reference 45, and an emprical curve for the emulsion sensitivity. The best relative line intensities should be accurate to about 10 percent while most ratios should be accurate to 30 percent. The resulting values are given in Table II-12.

A comparison of the results of the two independent measurements of the absolute conversion-electron intensities indicates roughly their uncertainties. The feeling is that, in general, the agreement is quite good. The intensities furnished by these analyses allow multipolarity assignments for many of the transitions. Figure II-35 shows a plot of the theoretical K conversion coefficients[43] for E1, E2, M1, and M2 radiations as a function of transition energy. Included are the experimental values and their estimated uncertainties. These assignments are also included in Table II-12 and compared with similar assignments from Reference 42. In the few cases where there is a discrepancy, the difference lies primarily in the gamma-ray intensities rather than the electron intensities. This is not surprising since accurate analysis of gamma-ray intensities would have been almost impossible without the assistance afforded by the germanium devices.

## 7.3 Presentation of Decay Scheme

A tentative decay scheme is presented in Figure II-36. This scheme incorporates about 50 percent of the observed transtions. It is divided into two parts. The section on the left represents transitions and levels which have been placed uniquely on the basis of their coincidence relationships, intensities, and energies. The double lines indicate transitions which were also observed [35,36,42] in the decay of Pm-148. On the right-hand side are placed transitions between these same levels where the energy difference between the states corresponds to the transition energy to ± 0.5 keV. Levels at 550.1, 1161.2, 1179.9, 1594.0, 1905.4, 2095.1, and 2193.9 keV are states which are also observed [35,36,42] in the decay of Pm-148. The spins and parities assigned to these states from the Pm-148 studies have been included in Figure 36. These assignments are consistent with the experimental data of the present study -- primarily limited to the deduced multipolarities. The remainder of the tentative spin and parity assignments shown in Figure II-36 were made on the basis of transition multipolarity assignments (from conversion-coefficient measurements) and from a knowledge of the spins and parities of the states fed in the depopulation of the particular levels.

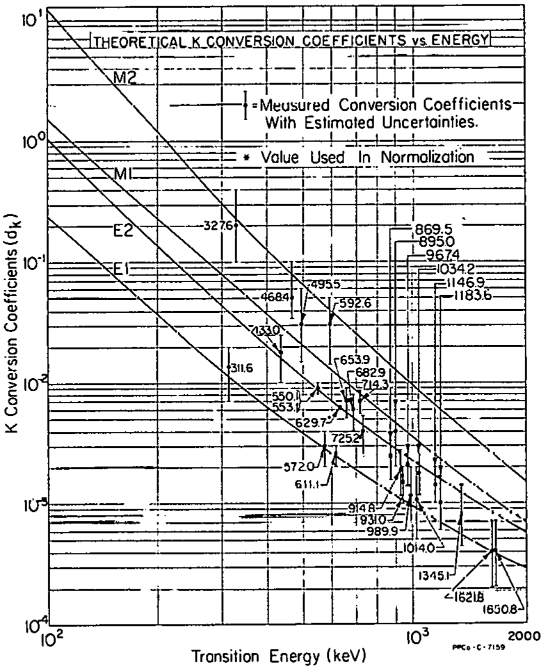

Fig. II-35 Plot of theoretical K-conversion coefficients for Z = 64. Measured coefficients and their uncertainties are shown on the curves.

Due to the tentative and incomplete nature of the proposed decay scheme for Eu-148, no further discussion of the level structure of Sm-148 or of the transitions will be made at this time. Additional study is currently being made on this decay scheme.

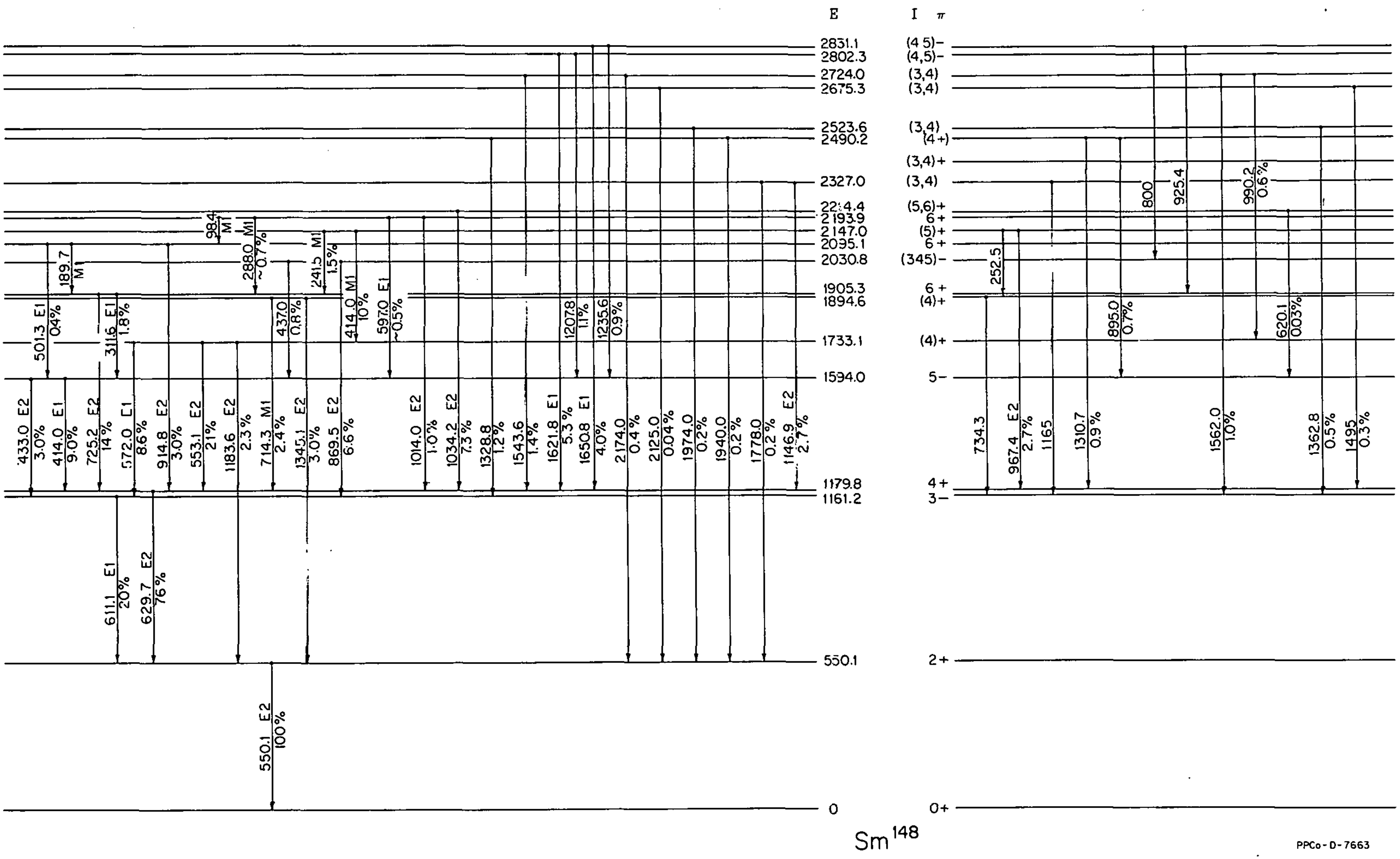

Fig. II-36 Proposed tentative decay scheme for Eu-148. Left side shows uniquely placed transitions; whereas, those shown on the right are placed on the basis of energy considerations only.

# 8. REFERENCES

1. R. M. Brugger and P. D. Randolph, Slow Neutron Inelastic Scattering from Aluminum Powder, IDO-17063 (February 1965).

2. R. E. Schmunk, "Slow Neutron Inelastic Scattering from Beryllium Powder", Phys. Rev., 136 (November 30, 1964) p 1303.

3. P. D. Randolph, "Slow Neutron Inelastic Scattering from Liquid Sodium", Phys. Rev., 134 (June 1, 1964) pp A1238-48.

4. P. K. Iyengar, "A New Method in Neutron Spectrometry", Nuclear Physics and Solid State Physics Symposium, Bombay. Atomic Energy Establishment, 1964.

5. P. K. Iyengar et al, "Dispersion Relations for Phonons in Magnesium", International Conference on Lattice Dynamics, Copenhagen: Pergamon Press, 1963, pp 223-232.

6. R. E. DeWames, T. Wolfram, and G. W. Lehman, "Lattice Dynamics, Heat Capacities, and Debye-Waller Factors for Be and Zn Using a Modified Axially Symmetric Model", Phys. Rev., 138 (May 3, 1965) pp A717-28.

7. R. E. Schmunk et al, "Lattice Dynamics of Beryllium", Phys. Rev., 128 (October 15, 1962) p 562.

8. R. P. Gupta and B. Dayal, "An Electron Gas Model for the Lattice Dynamics of Beryllium", Phys. Status Solidi, 8 No. 1 (1965) pp 115-22.

9. J. A. Young and J. U. Koppel, "Coherent Inelastic Scattering from Polycrystalline Beryllium", Phys. Letters, 16 No. 3 (June 1, 1965) pp 235-7.

10. George J. Kirouac, "Epithermal Neutron Inelastic Scattering by Room Temperature Water and Polyethylene", Thesis, Rensselaer Polytechnic Institute (June 1965).

11. J. R. Beyster et al, "Integral Neutron Thermalization", Quarterly Report for the Period Ending December 31, 1964, GA-6096 (January 28, 1965). Unable to verify communications.

12. M. Tasumi, T. Shimanouchi, and T. Miyazawa, "Normal Vibrations and Force Constants of Polymethylene Chain", J. Mol. Spectr., 9 (July-December 1962) pp 261-287.

13. Enomoto and Asahina, J. Polymer Sci. (Part A), 2, 3523 (1964).

14. J. R. Smith and S. D. Reeder, "Measurement of the Number of Fission Neutrons per Absorption in U-233 and Pu-239", Am. Phys. Soc. Bull., 9 No. 1 (1964) p 19.

15. J. R. Smith and H. G. Miller, A Mechanical Neutron Filter for a Crystal Spectrometer, IDO-16878 (June 1963).

16. R. L. Macklin et al, "Manganese Bath Measurements of $\eta$ of U-233 and U-235", Nucl. Sci. Eng., 8 No. 3 (September 1960) pp 210-220.

17. E. R. Cohen, K. M. Crowe, and J. W. M. DuMond, Fundamental Constants of Physics, New York: Interscience Publishers, Inc., 1957, Chapter 7.

18. Nuclear Technology Branches Quarterly Report, July 1 - September 30, 1964, IDO-17052 (1964).

19. D. J. Hughes and R. B. Schwartz, Neutron Cross Sections, BNL-325 (July 1958).

20. M. Nelkin, "Scattering of Slow Neutrons by Water", Phys. Rev., 119 (July 15, 1960) pp 741-746.

21. R. G. Nisle and E. Fast, Distribution of U-233 in an Irradiated Thorium Slug, IDO-16419 (October 1957).

22. J. W. Rogers, E. Fast, and D. A. Millsap, "Neutron Scattering Effects in Static Reactivity Measurements in the ARMF", Trans. Am. Nucl. Soc., 8 No. 1 (1965) p 258. Nuclear Technology Branches Quarterly Report, 1st Quarter 1965, IDO-17104 (December 1965).

23. G. E. Putnam, Some Methods of Calculation of the Parameters in the Reactor Kinetics Equations, IDO-16983 (February 1965).

24. W. K. Foell "Diffusion Theory Studies of the ARMF Neutron Flux and Adjoint Function", MTR-ETR Technical Branches Quarterly Report, October 1 - December 31, 1963, IDO-16977 (1963) pp 7-10.

    N. C. Kaufman and W. K. Foell, "Transport Theory Study of ARMF Real and Adjoint Fluxes", MTR-ETR Technical Branches Quarterly Report, January 1 - March 31, 1964, IDO-16994 (1964) pp 17-18.

25. H. P. Flatt and D. C. Baller, AIM-5: A Multigroup, One Dimensional Diffusion Equation Code, NAA-SR-4694 (March 1960).

26. G. D. Joanou and J. S. Dudek, GAM-1: A Consistent P1 Multigroup Code for the Calculation of Fast Neutron Spectra and Multigroup Constants, GA-1850 (June 1961).

27. R. H. Shudde and J. Dyer, TEMPEST-II, A Neutron Thermalization Code, TID-18284 (June 1962).

28. H. P. Flatt, "PERT, A Perturbation Theory Code", NAA Program Description from Nuclear Code Library (February 1961).

29. D. F. Crouch and R. L. Heath, Routine Testing and Calibration Procedures for Multichannel Pulse Analyzers and Gamma-Ray Spectrometer, IDO-16923 (November 1963).

30. G. Murray, R. L. Graham, and J. S. Geiger, "The Precision Determination of Some γ-Ray Energies Using a β-Spectrometer", Nucl. Phys., 63 (March 1965) pp 353-82.

31. B. Linstroem and I. Marklund, "Gamma Intensities in the Decay of Ir-192", Nucl. Phys., 49 (December 1963) pp 609-23.

32. Atomic Energy of Canada LTD. Chalk River Nuclear Labs., Chalk River, Ontario, Physics Division Progress Report, October 1 - December 31, 1963, PR-P-60 (1963) pp 23-25.

33. R. L. Robinson et al (article to be published in Nuclear Physics).

34. M. Putman et al, A Nonlinear Least-Square Program for the Determination of Parameters of Photopeaks by the Use of a Modified-Gaussion Function, IDO-17016 (August 1965).

35. C. W. Reich et al, "Radioactive Decay of Pm-148 and Pm-148m", Phys. Rev., 127 (July 1962) pp 192-204.

36. C. F. Schwerdtfeger, E. G. Funk, Jr., and J. W. Mihelich, "Decay of Pm-148, Pm-148m, and Eu-148", Phys. Rev., 125 (March 1962) pp 1641-1649.

37. K. Sugiyama, "Decay of Eu-148", J. Phys. Soc. Japan, 17 (February 1962) pp 264-73.

38. S. Jha et al, "The Decay of Eu-147 and Eu-148", Nuovo Cimento (10), 25 (July 1962) pp 28-40.

39. C. V. K. Baba, G. T. Ewan, and J. F. Súarez, "Levels in Sm-148 Fed in the Decay of Eu-148", Nucl. Phys., 43 (May 1963) pp 285-302.

40. C. M. Davisson, "Gamma Ray Attenuation Coefficients", in Alpha-, Beta-, and Gamma-Ray Spectroscopy, Vol. 1, K. Siegbahn (ed.), Amsterdam: North Holland Publishing Co., 1965.

41. R. L. Heath et al, The Calculation of Gamma-Ray Shapes for Sodium Iodide Scintillation Spectrometers. Computer Programs and Experimental Problems, IDO-17017 (April 1965).

42. C. V. K. Baba, G. T. Ewan, and J. F. Súarez, "Levels in Sm-148 Fed in the Beta-Decay of Pm-148 and Pm-148m", Nucl. Phys., 43 (May 1963) pp 264-84.

43. L. A. Sliv and I. M. Band, Coefficients of Internal Conversion of Gamma Radiation. Part I, K.-Shell, AEC-tr-2888 (1956).

44. R. G. Helmer, "Calibration of Permanent-Magnet Spectrographs", Nuclear Technology Branches Quarterly Report, April 1 - June 30, 1964, IDO-17042 (1964) p 44.

45. H. Slatis, "Intensity Determination of Photographically Recorded Conversion Lines, II", Ark. Fys., 22 No. 6 (1962) pp 517-533.

# III. INSTRUMENT DEVELOPMENT

## 1. INSTRUMENTATION ANALYSIS

(N. Wilde)

### 1.1 Analog Computer Simulation of PIQUA Primary Coolant System (J. W. Sielinsky, F. K. Hyer)

1.11 Introduction. The object of this analysis was to determine the coolant pressure at a fuel element hot spot and reactor core flow transients caused by a rupture in the upper or lower plenum of the reactor vessel. The transients will be used to calculate the burnout ratios in the reactor core.

A preliminary analysis was made to obtain a general idea of the transients caused by a rupture. The model for this analysis included only the surge tank, upper plenum of the vessel, and the rupture. Transients were obtained for (a) the initial upper plenum pressure at 120 and 200 psia, (b) the initial surge tank gas volume at 870 and 435 gal, and (c) the two surge tank connecting pipes, 3 and 4 inches in diameter.

A detailed analysis of the primary coolant system was made to obtain a more realistic simulation of the physical system. The model included everything that was felt to have a significant effect on the transients caused by the ruptures. Transients were recorded for (a) the upper and lower plenum ruptures, (b) the 3- and 4-inch-diameter surge tank connecting pipes, and (c) an upper plenum rupture with the control valve closing after the rupture.

Instantaneous ruptures were used for all cases because the time function of a rupture is questionable.

1.12 Simulation of Primary Coolant System.

(1) Preliminary Analysis. In this analysis only the surge tank, the upper plenum, and the rupture were considered (Figure III-1). The flow diagram of the system considered is shown in Figure III-2.

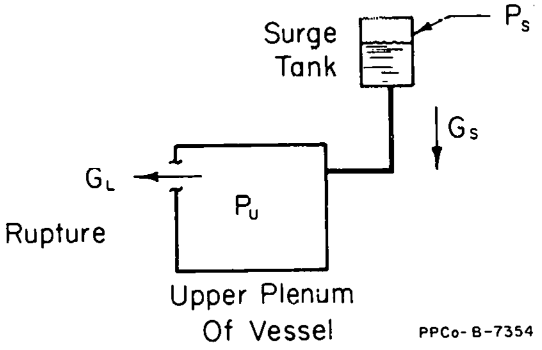

Fig. III-1 System for preliminary analysis.

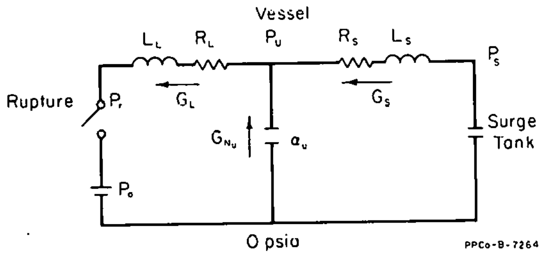

Fig. III-2 Flow diagram of system.

The equations describing the pressure drops between nodes are (see Section III-1.13), Appendix, for definition of terms):

$$P_s - P_u = R_s G_s^2 + L_s \dot{G}_s \,. \quad (1)$$

$$P_u - P_r = R_L G_L^2 + L_L \dot{G}_L \,. \quad (2)$$

For an instantaneous rupture

$$P_r = P_a \tag{3}$$

at the time of the rupture.

The equation for the summation of the flows at the node is

$$G_L = G_s + G_{Nu} . \tag{4}$$

The equation for the pressure in the vessel is

$$P_u = P_u(0) - \alpha_u \int_0^t G_{Nu}\, dt \tag{5}$$

where

$$\alpha_u = \frac{B}{60V_u} . \tag{6}$$

The surge tank pressure, assuming isothermal expansion of the gas, is calculated from

$$P_s V_s = P_s(0)\, V_s(0) \tag{7}$$

where

$$V_s = V_s(0) + \frac{1}{60} \int_0^t G_s\, dt . \tag{8}$$

Combining Equations (7) and (8) gives

$$P_s = \frac{P_s(0)\, V_s(0)}{V_s(0) + \frac{1}{60} \int_0^t G_s\, dt} . \tag{9}$$

The analog computer diagram used to solve the above equations for an instantaneous rupture is shown in Figure III-3.

The transients caused by an instantaneous 7-square-inch rupture for various initial conditions are shown in Figures III-4 through -9.

Figure III-4 shows the transients of upper plenum pressure ($P_u$), of rupture flow ($G_L$), and of surge tank gas volume ($V_s$) for initial condition of $P_u(O) = 120$ psia and $V_s(O) = 870$ gallons. The upper plenum pressure drops to 24 psia at 0.25 second, then the surge tank brings the pressure back up to 48.5 psia at 1 second. The maximum rupture flow of 2780 gpm is reached in approximately 0.02 second. The surge tank is empty of organic fluid in 26.4 seconds.

Figure III-5 shows the transients for the same initial pressure, $P_u(O) = 120$ psia, with the initial gas volume reduced to 435 gallons. The main effects of decreasing the initial gas volume are that it takes longer for the surge tank to empty and the pressure and flow decreases faster after the first part of the transient. The reason they decrease faster is that there is less gas volume to keep up the surge tank pressure.

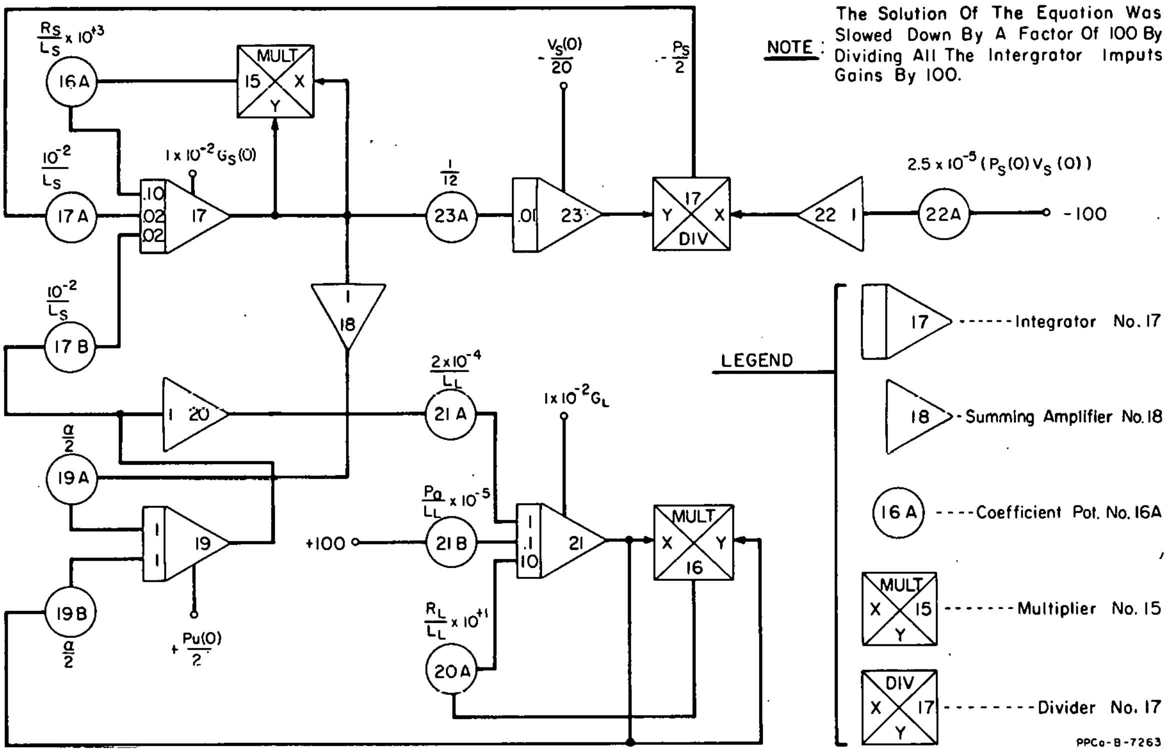

**NOTE:** The Solution Of The Equation Was Slowed Down By A Factor Of 100 By Dividing All The Intergrator Imputs Gains By 100.

Fig. III-3 Analog computer diagram for preliminary analysis.

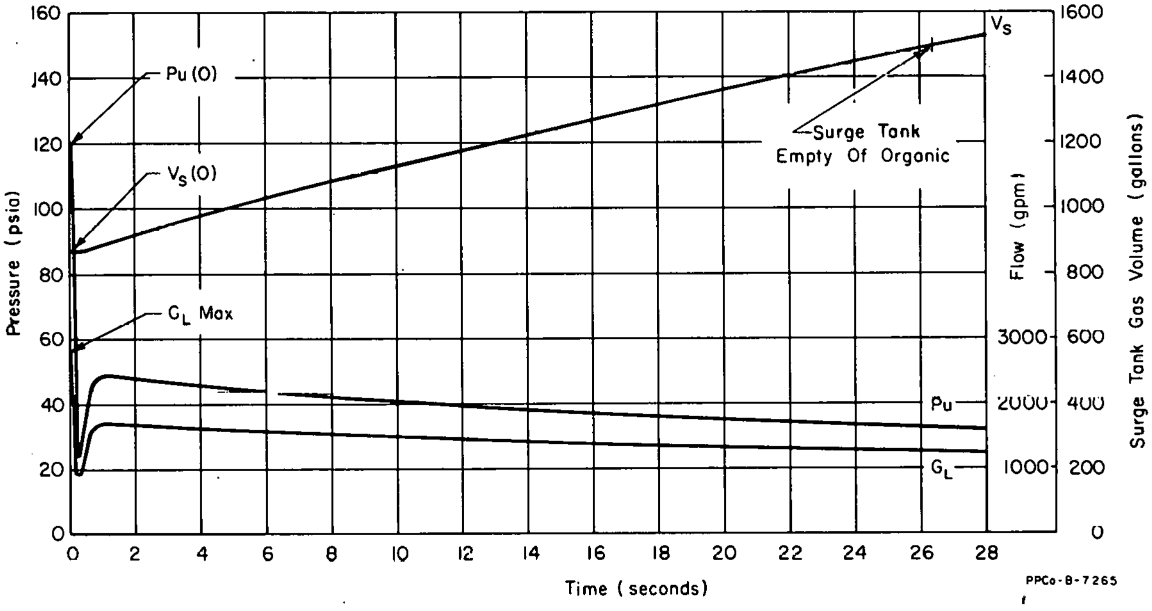

Fig. III-4 Transients with $P_u(O)$ = 120 psia and $V_s(O)$ = 870 gal.

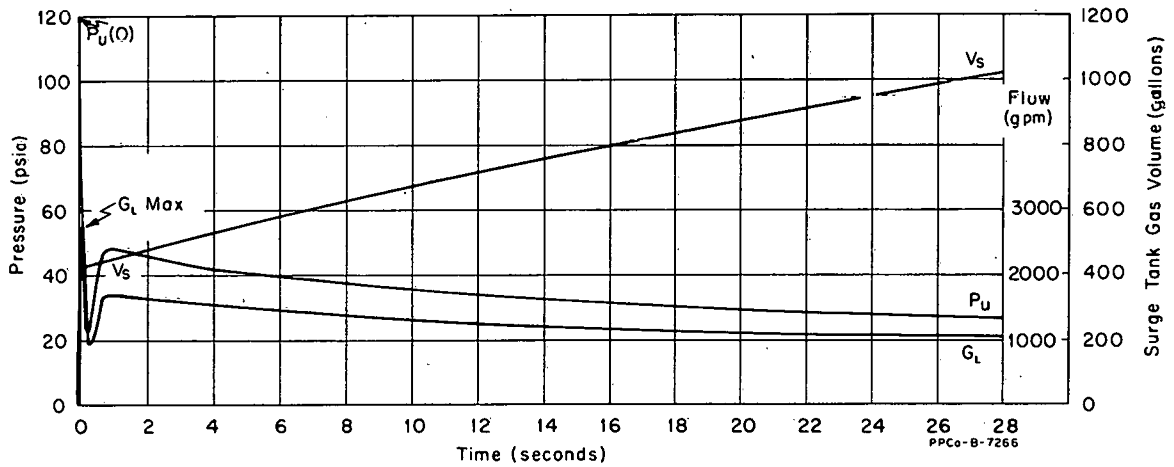

Fig. III-5 Transients with $P_u(O) = 120$ psia and $V_s(O) = 435$ gal.

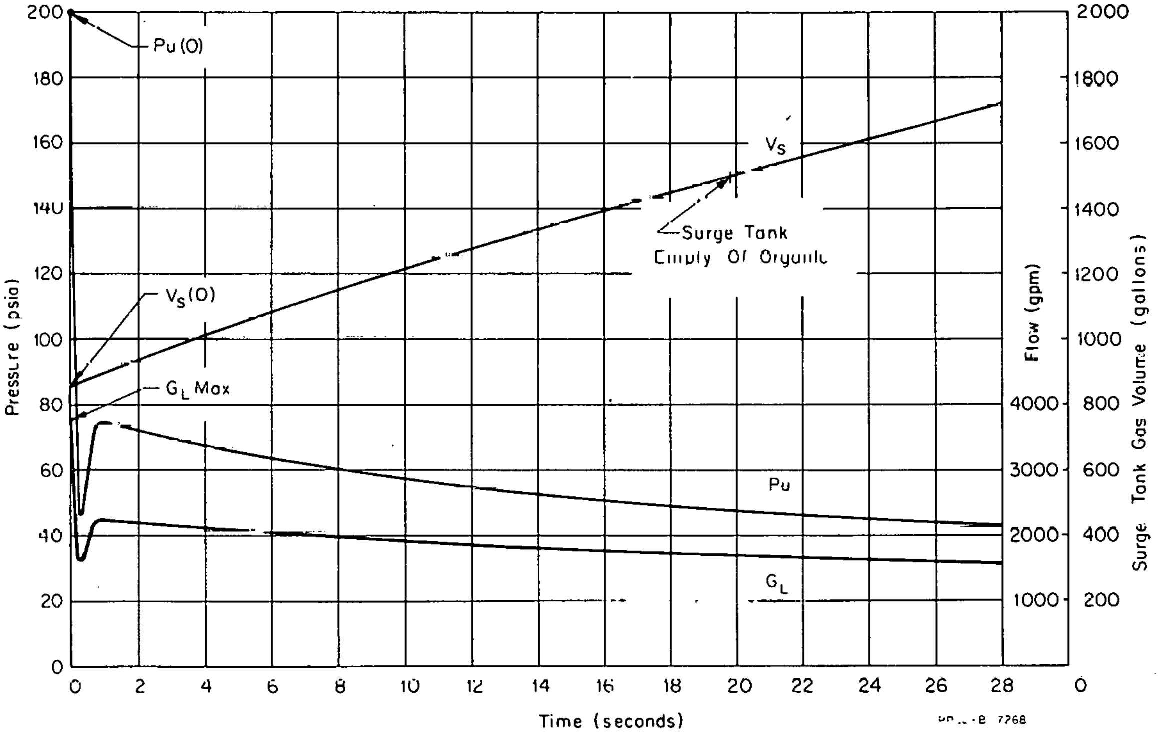

Fig. III-6 Transients with $P_u(O) = 200$ psia and $V_s(O) = 870$ gal.

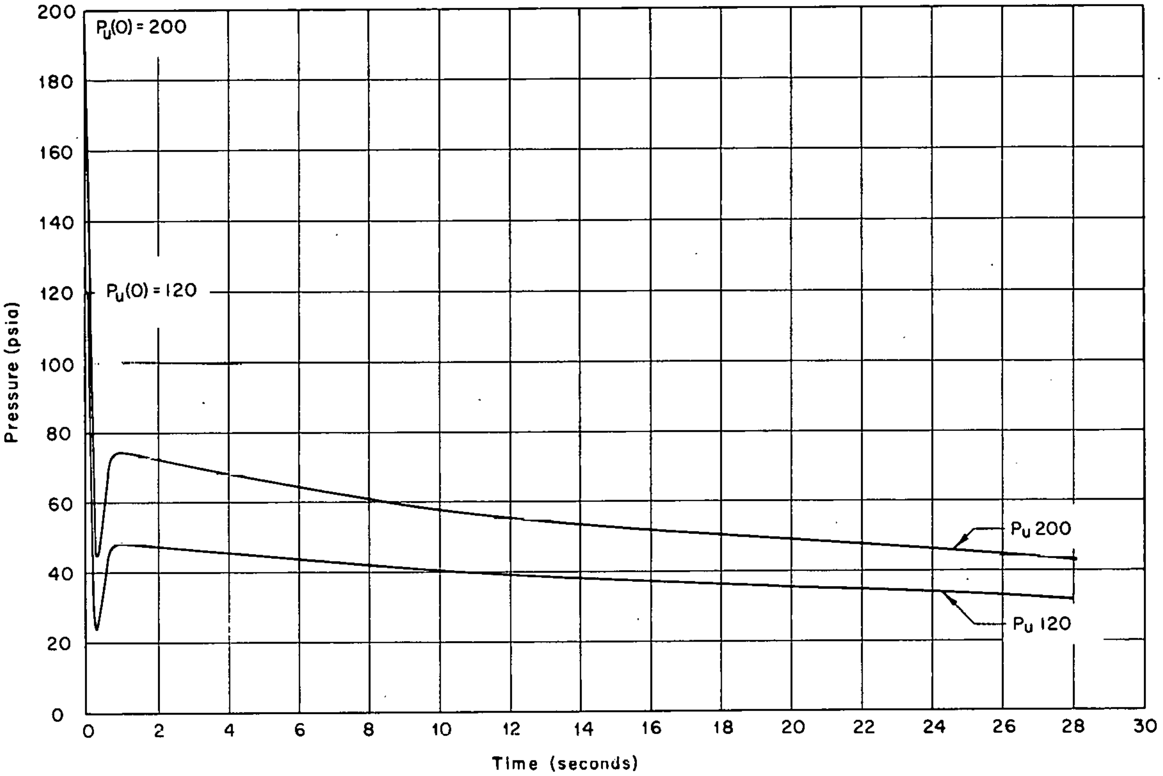

PPCo-B-7308

Fig. III-7 Comparison of pressure transients for $P_u(O)$ = 120 psia and $P_u(O)$ = 200 psia.

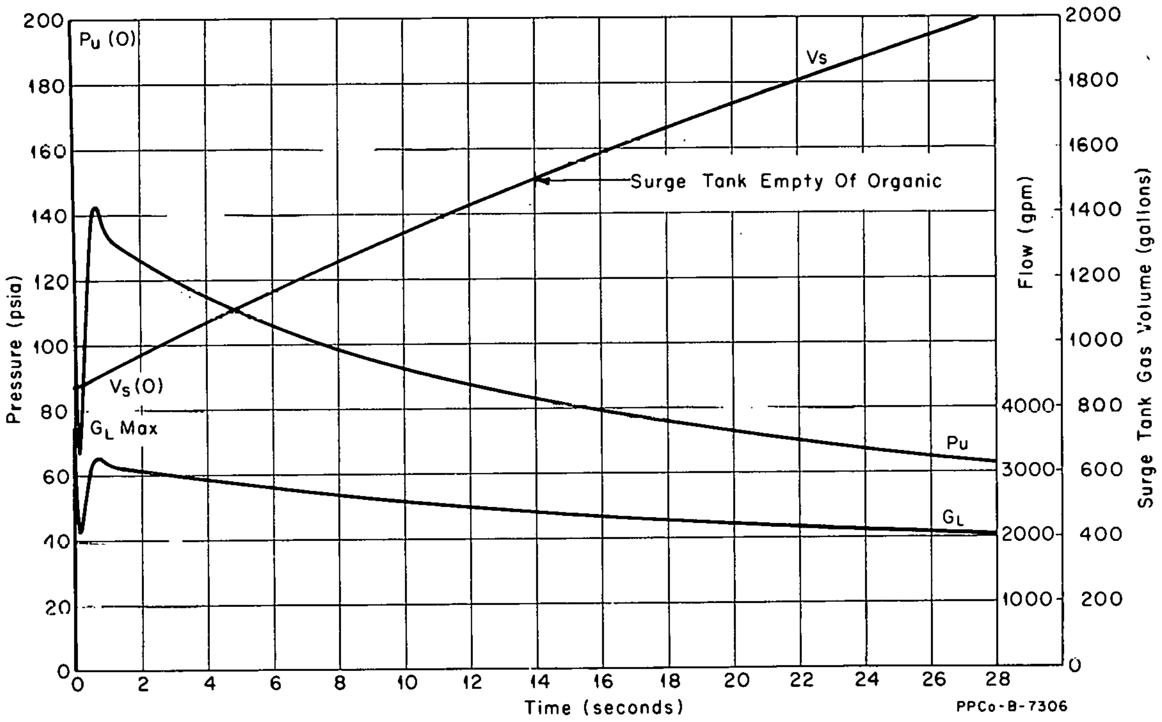

PPCo-B-7306

Fig. III-8 Transients for 4-inch surge tank connecting pipes.

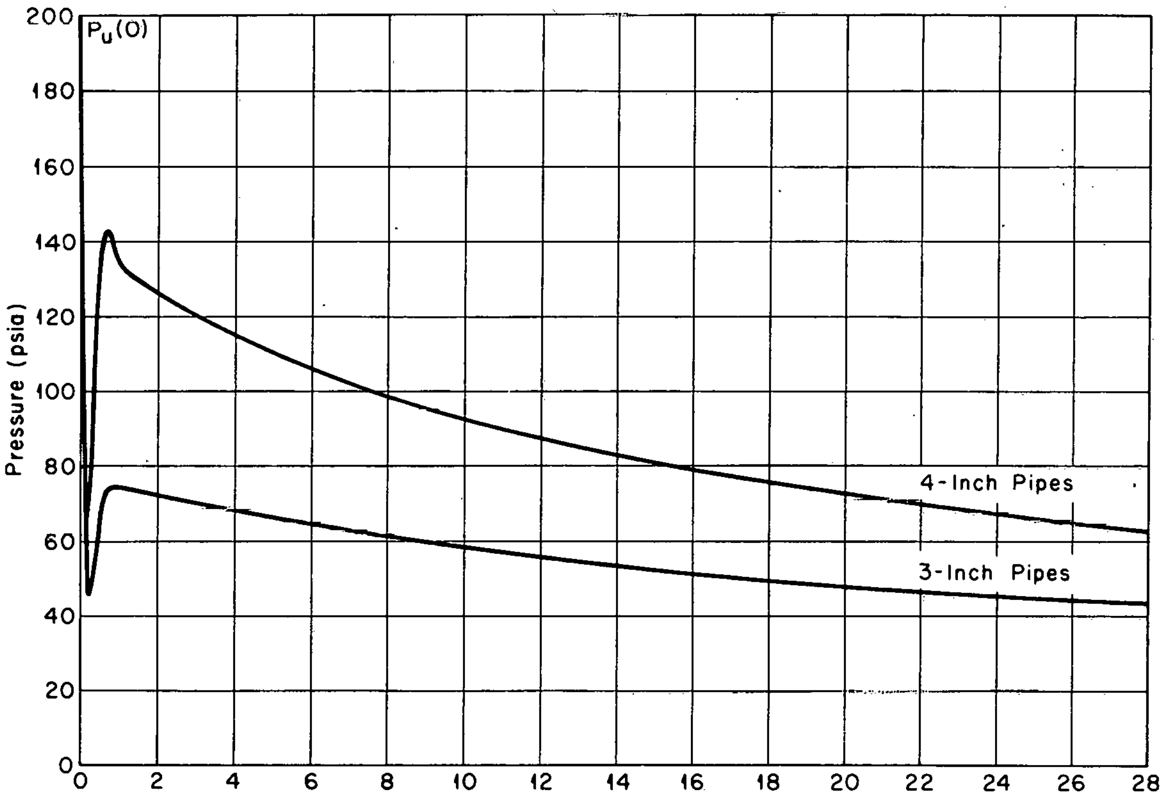

PPCo-B-7307

Fig. III-9 Comparison of pressure transients for 3- and 4-inch surge tank connecting pipes.

Figure III-6 shows the transients for an initial pressure of 200 psia and an initial gas volume of 870 gallons. The surge tank is empty at 19.8 seconds. The comparison of the pressure transients for the initial pressure of 120 psia and the initial pressure of 200 psia is shown in Figure III-7. The pressure drops to 46 psia at 0.25 second for $P_u(O) = 200$ psia; whereas, for $P_u(O) = 120$ psia, it drops to 24 psia at 0.25 second.

Figure III-8 shows the transients for $P_u(O) = 200$ psia and $V_S(O) = 870$ gallons with the diameters of the two surge tanks connecting pipes increased from 3 to 4 inches. The surge tank is empty at 14 seconds. The comparison of the pressure transients for the 3- and 4-inch pipes is shown in Figure III-9. For the larger pipes, the pressure transient drops to 67 psia at 0.25 second; whereas, for the smaller pipes, it drops to 46 psia at 0.25 second.

General Conclusions from the Preliminary Analysis: The pressure drops to 24 psia at 0.25 second for the nominal case. This pressure drop is caused by the flow out of the surge tank not being able to follow the flow out of the instantaneous rupture. The pressure can be kept from dropping as low by increasing the system pressure or increasing the size of the surge tank connecting pipes.

This pressure drop can also be kept from dropping as low by making the rupture a finite function of time instead of instantaneous. The configuration of a rupture as a function of time is questionable; therefore, an instantaneous rupture was used.

(2) Detailed Analysis. In this simulation, everything that was felt to have a significant effect on the transients caused by a rupture was included. The primary coolant system is shown in Figure III-10, and the flow diagram of the system is shown in Figure III-11.

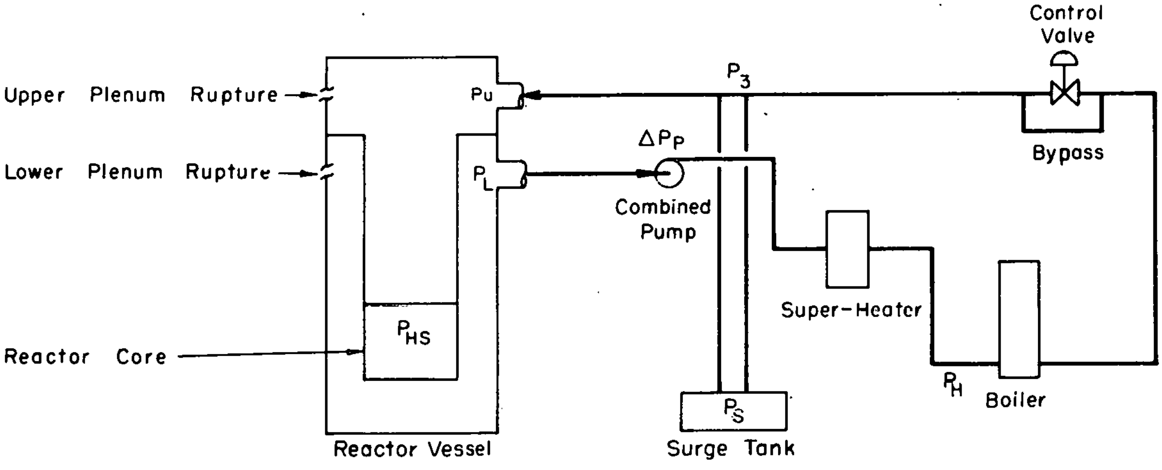

Fig. III-10 Primary coolant system.

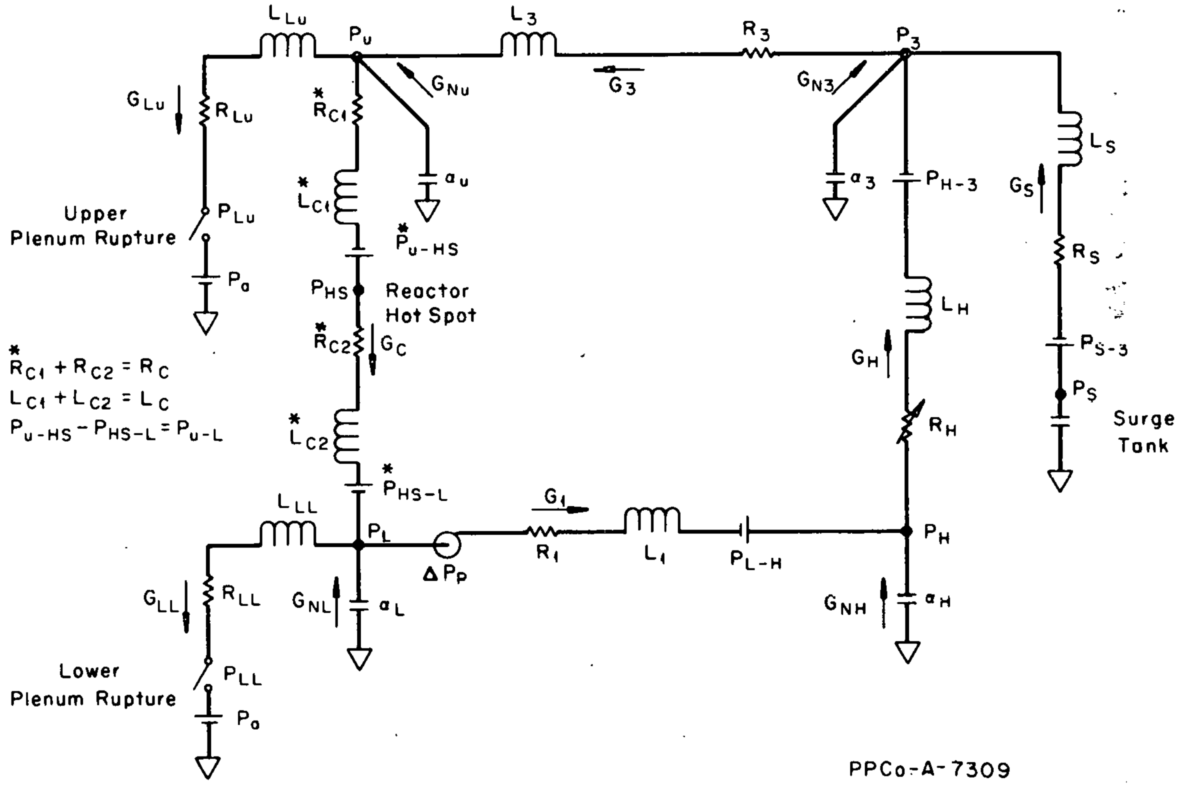

Fig. III-11 Flow diagram of primary coolant system.

The equations describing the pressure drops between nodes (see Section III-1.13, Appendix, for definition of terms) are the following:

$$P_3 = P_u - R_3G_3^2 + L_3\dot{G}_3 \tag{10}$$

$$P_u - P_{LU} = R_{LU}G_{LU}^2 + L_{LU}\dot{G}_{LU} \tag{11}$$

$$P_u + P_{U-L} - P_L = R_CG_C^2 + L_C\dot{G}_C \tag{12}$$

$$P_L + \Delta P_p + P_{L-H} - P_H = R_1G_1^2 + L_1\dot{G}_1 \tag{13}$$

$$P_L - P_{LL} = R_{LL}G_{LL}^2 + L_{LL}\dot{G}_{LL} \tag{14}$$

$$P_H - P_{H-3} - P_3 = R_HG_H^2 + L_H\dot{G}_H \tag{15}$$

$$P_s - P_{s-3} - P_3 = R_sG_s^2 + L_s\dot{G}_s^2 \tag{16}$$

For an upper plenum instantaneous rupture,

$$P_{LU} = P_a \tag{17}$$

and for a lower plenum rupture,

$$P_{LL} = P_a \; . \tag{18}$$

In Equation (15), the flow resistance ($R_H$) includes the control valve. For the first transients recorded, the valve was considered to be open during the transients, therefore, $R_H$ was held constant.

The equations for the pressures at the nodes are as follows:

$$P_3 = P_3(0) - \alpha_3 \int_0^t G_{N3}\, dt \tag{19}$$

$$P_u = P_u(0) - \alpha_u \int_0^t G_{Nu}\, dt \tag{20}$$

$$P_L = P_L(0) - \alpha_L \int_0^t G_{NL}\, dt \tag{21}$$

$$P_H = P_H(0) - \alpha_H \int_0^t G_{NH}\, dt \; . \tag{22}$$

The equations for the summation of the flows at the nodes are as follows:

$$G_H + G_s + G_{N3} = G_3 \tag{23}$$

$$G_3 + G_{Nu} = G_{LU} + G_c \; . \tag{24}$$

$$G_C + G_{NL} = G_1 + G_{LL} \tag{25}$$

$$G_1 + G_{NH} = G_H \ . \tag{26}$$

For the upper plenum rupture, $G_{LL} = 0$; and for the lower plenum rupture, $G_{LU} = 0$.

The equation for the surge tank pressure is

$$P_s = \frac{P_s(0)\ V_s(0)}{V_s(0) + \frac{1}{60}\int_0^t G_s\, dt} \ . \tag{27}$$

The equation used to calculate the reactor core hot-spot pressure is

$$P_{HS} = P_u + P_{u\text{-}HS} - R_{C1}G_C^2 - L_{C1}\dot{G}_C \ . \tag{28}$$

The equation for the developed pressure across the two primary coolant pumps, combined into an equivalent pump, is

$$\Delta P_p = f(G) \tag{29}$$

where f(G) is the combined pump head curve in Figure III-12.

The analog computer diagram used for the analog computer simulation of the above equations is shown in Figure III-13. Flow and pressure transients caused by the instantaneous seven-square-inch rupture for various conditions are shown in Figures III-14 through -16.

Figure III-14 shows the transients for a rupture in the upper plenum of the reactor vessel. The hot-spot pressure ($P_{HS}$) drops to 22 psia at 0.4 second, then

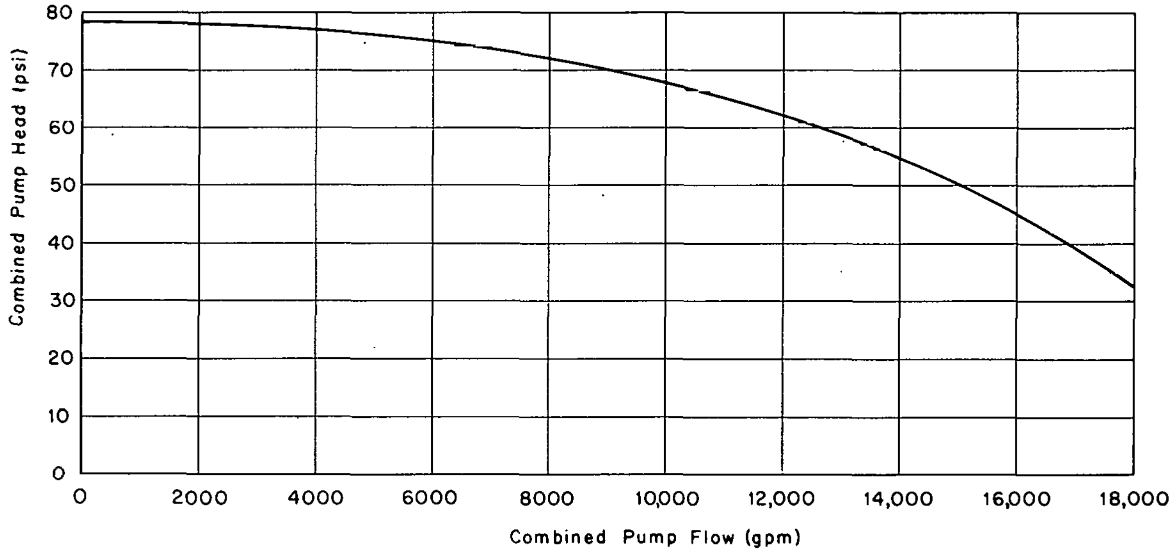

Fig. III-12 Pump curve for the two pumps combined into one equivalent pump.

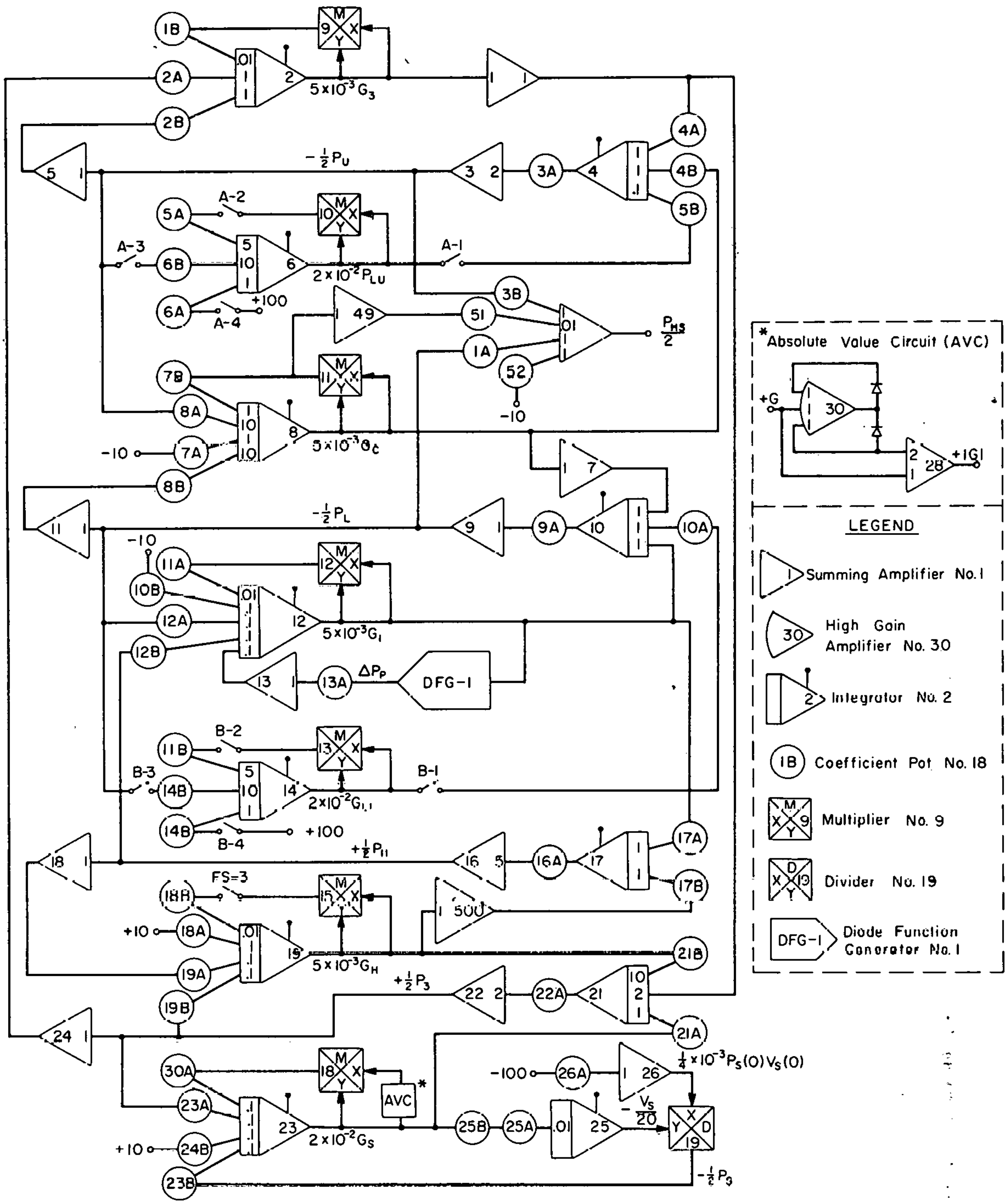

A Switches Closed For Upper Plenum Rupture
B Switches Closed For Lower Plenum Rupture
FS-3 See Note Figure III-18

NOTE: Solution Slowed Down By 100
See Appendix B For Pot Settings And
Integrator Initial Condition

PP Co-B-7460

Fig. III-13 Analog computer diagram of primary coolant system.

# COEFFICIENT POTENTIOMETER SETTINGS

TITLE Fig.III-13A Potentiometer Settings for Figure III-13 DATE

PROBLEM No.

| POT NO. | FORMULA | SETTINGS 1 | 2 | 3 | 4 | 5 | 6 | 7 | 8 | 9 |
|---|---|---|---|---|---|---|---|---|---|---|
| 1A | $L_{C1}/L_C$ | 0.7593 | | | | | | | | |
| 1B | $2x10^4 R_3/L_3$ | 0.1774 | | | | | | | | |
| | | | | | | | | | | |
| 2A | $1x10^{-4}$ $1/L_3$ | 0.5794 | | | | | | | | |
| 2B | $1x10^{-4}$ $1/L_3$ | 0.5794 | | | | | | | | |
| | | | | | | | | | | |
| 3A | $2.5\ \alpha_u$ | 0.7863 | | | | | | | | |
| 3B | $1-(L_{C1}/L_C)$ | 0.2407 | | | | | | | | |
| | | | | | | | | | | |
| 4A | Scale factor | 0.2 | | | | | | | | |
| 4B | Scale factor | 0.2 | | | | | | | | |
| | | | | | | | | | | |
| 5A | $10\ R_{LU}/L_{LU}$ | 0.6303 | | | | | | | | |
| 5B | Scale factor | 0.5 | | | | | | | | |
| | | | | | | | | | | |
| 6A | $2x10^{-6} P_a/L_{LU}$ | 0.1422 | | | | | | | | |
| 6B | $4x10^{-5} (1/L_{LU})$ | 0.1896 | | | | | | | | |
| | | | | | | | | | | |
| 7A | $5x10^{-6} P_{u-L}/L_C$ | 0.1695 | | | | | | | | |
| 7B | $2x10^{-2} R_C/L_C$ | 0.6918 | | | | | | | | |
| | | | | | | | | | | |
| 8A | $1x10^{-5}/L_C$ | 0.1695 | | | | | | | | |
| 8B | $1x10^{-5}/L_C$ | 0.1695 | | | | | | | | |
| | | | | | | | | | | |
| 9A | $\alpha_L$ | 0.5711 | | | | | | | | |
| | | | | | | | | | | |
| 10A | Scale factor | 0.25 | | | | | | | | |
| 10B | $5x10^{5} P_{L-H}/L_1$ | 0.2588 | | | | | | | | |
| | | | | | | | | | | |
| 11A | $2x10^{+4} R_1/L_1$ | 0.4290 | | | | | | | | |
| 11B | $10\ R_{LL}/L_{LL}$ | 0.6303 | | | | | | | | |
| | | | | | | | | | | |
| 12A | $1x10^{-3}/L_1$ | 0.6468 | | | | | | | | |
| 12B | $1x10^{-3}/L_1$ | 0.6468 | | | | | | | | |
| | | | | | | | | | | |
| 13A | $5x10^{-4}/L_1$ | 0.3234 | | | | | | | | |
| | | | | | | | | | | |

PPCo.-B-4336

# COEFFICIENT POTENTIOMETER SETTINGS

TITLE Potentiometer settings for Figure III-13 (contd.) DATE

PROBLEM No.

| POT NO. | FORMULA | SETTINGS 1 | 2 | 3 | 4 | 5 | 6 | 7 | 8 | 9 |
|---|---|---|---|---|---|---|---|---|---|---|
| 14A | $2x10^{-6} P_{LL}/L_{LL}$ | 0.1422 | | | | | | | | |
| 14B | $4x10^{-5}/L_{LL}$ | 0.1896 | | | | | | | | |
| 16A | $\alpha_H$ | 0.5956 | | | | | | | | |
| 17A | Scale factor | 0.2 | | | | | | | | |
| 17B | Scale factor | 0.2 | | | | | | | | |
| 18A | $5x10^{-5} P_{H-3}/L_H$ | 0.2982 | | | | | | | | |
| 18B | $2x10^{-4} R_H/L_H$ | 0.4380 | | | | | | | | |
| 19A | $1x10^{-3}/L_H$ | 0.5963 | | | | | | | | |
| 19B | $1x10^{-3}/L_H$ | 0.5963 | | | | | | | | |
| 21A | Scale factor | 0.5 | | | | | | | | |
| 21B | Scale factor | 0.2 | | | | | | | | |
| 22A | $0.25\ \alpha_3$ | 0.6328 | | | | | | | | |
| 23A | $4x10^{-3}/L_s$ | 0.2667 | 0.4740[a] | | | | | | | |
| 23B | $4x10^{-3}/L_s$ | 0.2667 | 0.4740[a] | | | | | | | |
| 24B | $2x10^{-4} P_{s-3}/L_s$ | 0.160 | 0.2844[a] | | | | | | | |
| 25A | Scale factor | 0.4167 | | | | | | | | |
| 25B | Scale factor | 0.1 | | | | | | | | |
| 26A | $2.5x10^{-6} P_s(0) V_s(0)$ | 0.1687 | | | | | | | | |
| 35A | $5x10^{+2} R_s/L_s$ | 0.3934 | 0.1722[a] | | | | | | | |
| 51 | $2x10^{+8}(\frac{L_{C1}}{L_C} R_C - R_{C1})$ | 0.3746 | | | | | | | | |
| 52 | $\frac{1}{20}(P_u - H_s - \frac{L_{C1}}{L_C} P_u - L)$ | 0.3124 | | | | | | | | |

[a] For 4-inch surge tank connecting pipes.

# COEFFICIENT POTENTIOMETER SETTINGS

TITLE Potentiometer settings for Figure III-13 (contd.) DATE

PROBLEM No.

| POT NO. | FORMULA | SETTINGS 1 | 2 | 3 | 4 | 5 | 6 | 7 | 8 | 9 |
|---|---|---|---|---|---|---|---|---|---|---|
| IC2 | $+5\text{x}10^{-3}\ G_3$ | +70 | | | | | | | | |
| 4 | $+0.1\ P_u(0)/\alpha_u$ | +42.93 | | | | | | | | |
| | | | | | | | | | | |
| 6 | $+2\text{x}10^{-2}\ G_{LU}$ | 0 | | | | | | | | |
| 8 | $+5\text{x}10^{-3}\ G_C$ | +70 | | | | | | | | |
| | | | | | | | | | | |
| 10 | $+1/2\ P_L(0)/\alpha_L$ | +84.9 | | | | | | | | |
| 12 | $+5\text{x}10^{-3}\ G_1$ | +70 | | | | | | | | |
| | | | | | | | | | | |
| 14 | $+2\text{x}10^{-2}\ G_{LL}$ | 0 | | | | | | | | |
| 17 | $-0.1\ P_H(0)/\alpha_H$ | -25.6 | | | | | | | | |
| | | | | | | | | | | |
| 19 | $+5\text{x}10^{-3}\ G_H$ | +70 | | | | | | | | |
| 21 | $-P_3(0)/\alpha_3$ | -53.46 | | | | | | | | |
| | | | | | | | | | | |
| 23 | $+2\text{x}10^{-2}\ G_s$ | 0 | | | | | | | | |
| 25 | $-V_c(0)/20$ | -22.9 | | | | | | | | |
| | | | | | | | | | | |
| | | | | | | | | | | |
| | | | | | | | | | | |
| | | | | | | | | | | |
| | | | | | | | | | | |
| | | | | | | | | | | |
| | | | | | | | | | | |
| | | | | | | | | | | |
| | | | | | | | | | | |
| | | | | | | | | | | |
| | | | | | | | | | | |
| | | | | | | | | | | |
| | | | | | | | | | | |
| | | | | | | | | | | |
| | | | | | | | | | | |
| | | | | | | | | | | |
| | | | | | | | | | | |
| | | | | | | | | | | |
| | | | | | | | | | | |
| | | | | | | | | | | |

PPCo.-B-4336

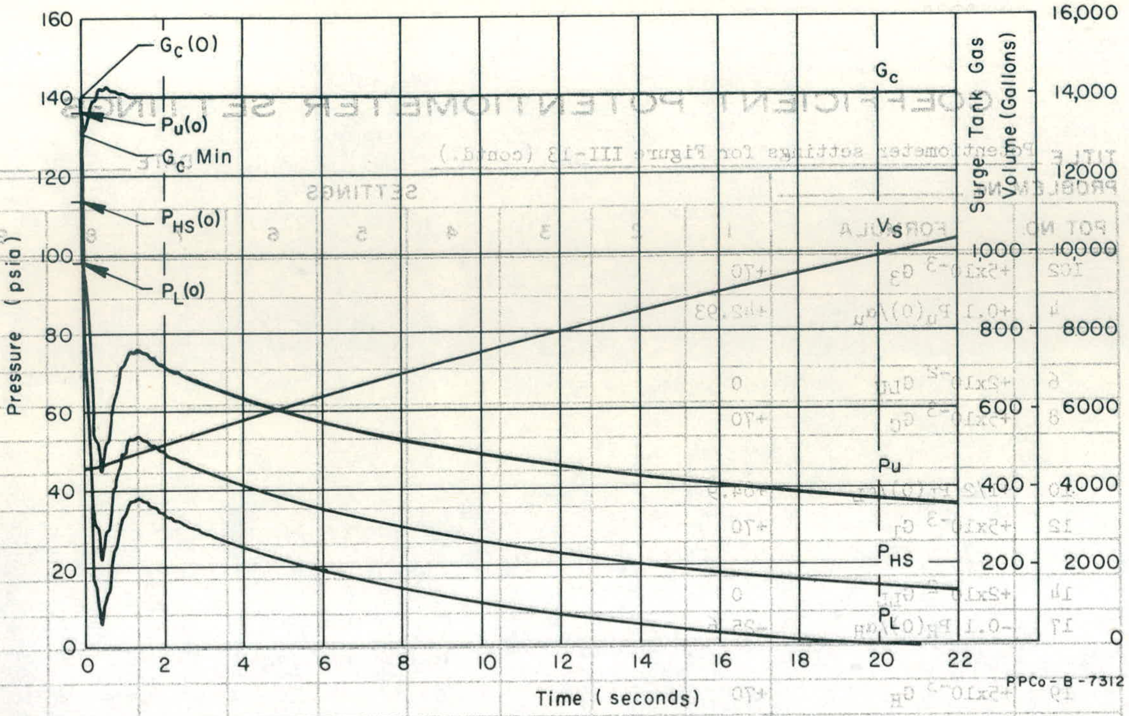

Fig. III-14 Transients for upper plenum rupture.

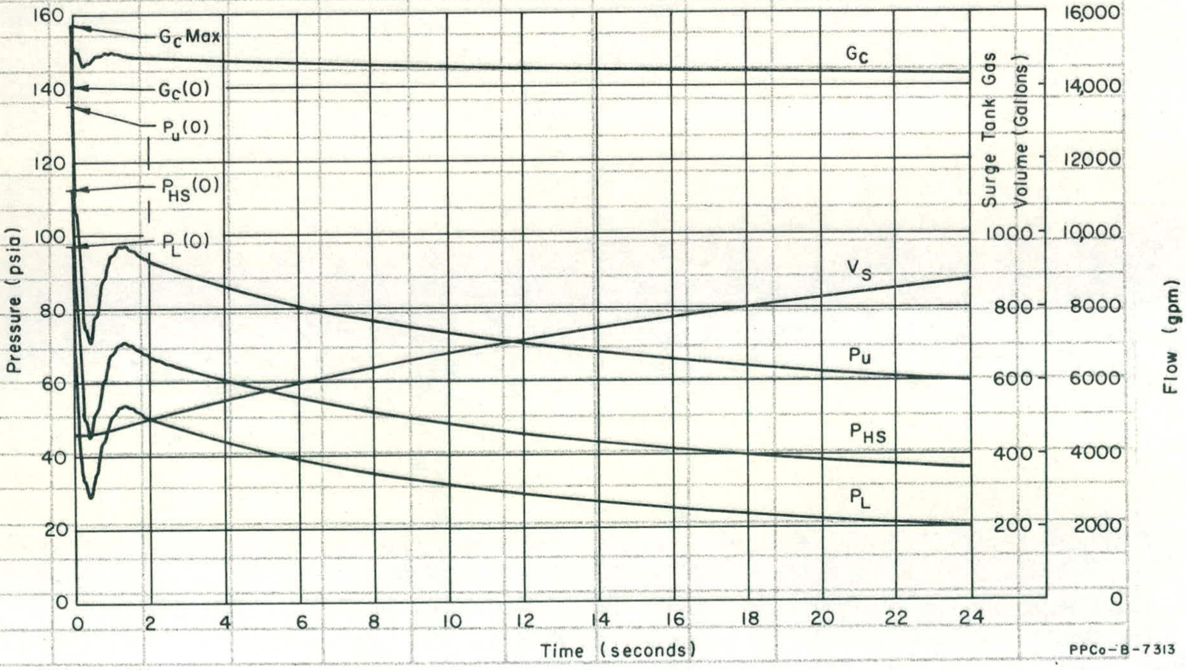

Fig. III-15 Transients for lower plenum rupture.

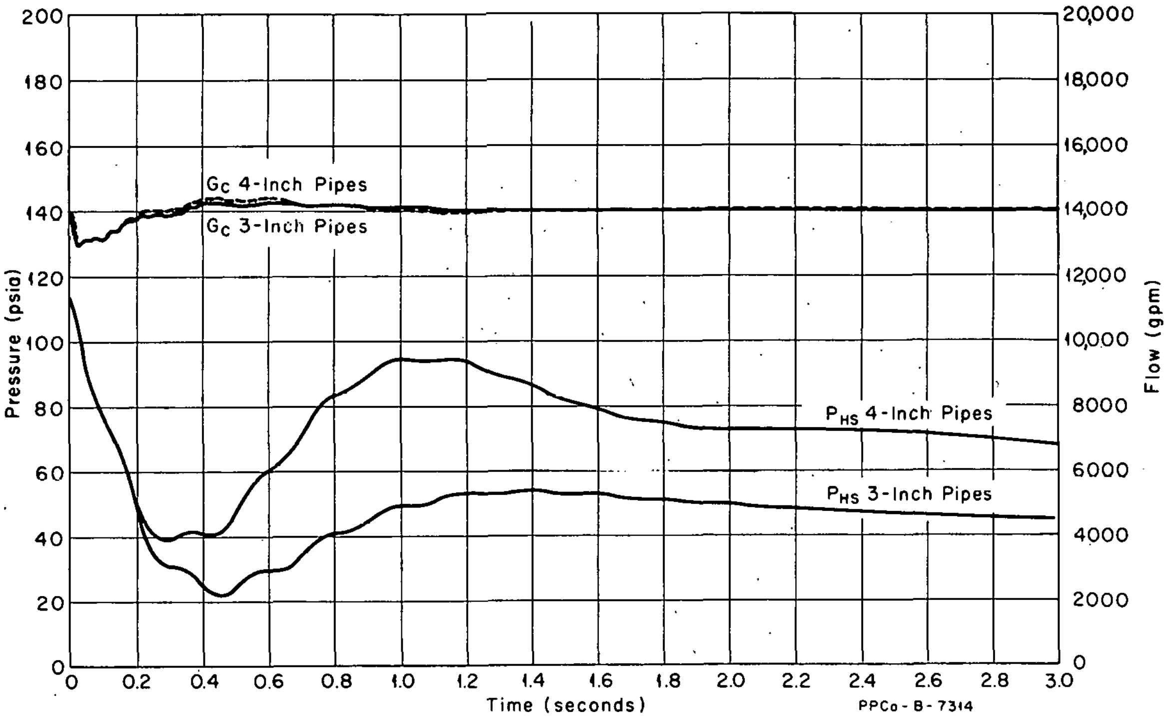

Fig. III-16 Comparison of transients for 3- and 4-inch surge tank connecting pipes.

goes up to 53.5 psia at 1.35 seconds. The lower plenum pressure ($P_L$) decays to zero at 18.8 seconds. The lower plenum pressure is approximately equal to the pump suction pressure; therefore, cavitation of the pump will occur when its suction pressure drops below a certain level. The cavitational characteristics of the pump were not included in the simulation. The cavitational effects would probably be insignificant when the pressure drops to 6 psia at 0.4 second because of the short time that the pressure is low, but, after the pressure decays toward zero, the effects would tend to reduce the flow through the pumps.

The transients for the lower plenum rupture are shown in Figure III-15. The hot-spot pressure drops to 45 psia at 0.4 second and goes to 70 psia at 1.35 seconds.

Figure III-16 shows the comparison of the transients for the two 3- and 4-inch surge tank connecting pipes. The hot-spot pressure drops to 22 psia for the 3-inch pipes; whereas, it only drops to 39 psia for the 4-inch pipes.

(a) Simulation of the Control Valve. In Equation (15), the flow resistance term ($R_H$) includes the resistance of the control valve and the bypass piping. In the previous analysis, the control valve was assumed to remain open during the transients.

In order to simulate the valve closing, an equivalent flow resistance of the valve and bypass was calculated. The equivalent resistance is

$$R_e = \frac{R_V R_B}{R_V + 2\sqrt{R_V R_B} + R_B} . \tag{30}$$

By assuming that the flow resistance of the valve is proportional to the reciprocal of the effective valve area squared, $R_V$ becomes

$$R_V = \frac{k}{A^2} \; . \tag{31}$$

Combining Equations (30) and (31) gives

$$R_e = \frac{k}{A^2 + 2A \dfrac{\sqrt{k}}{\sqrt{R_B}} + \dfrac{k}{R_B}} \; . \tag{32}$$

The total flow resistance then becomes

$$R_H = R_H' + \frac{k}{A^2 + 2A \dfrac{\sqrt{k}}{\sqrt{R_B}} + \dfrac{k}{R_B}} \; . \tag{33}$$

The value of $R_H$ as the valve closes has a range of over 3 decades (see Figure III-17). In order to cover this range, $R_H$, as a function of area, was simulated on three function generators with a switching arrangement. Figure III-18 shows the analog computer diagram of the arrangement used for the simulation of $R_H$.

The only information available on the control valve was that it would start closing 0.64 second after a rupture and be fully closed at 7 seconds. Therefore, the effective area of the valve was assumed to be directly proportional to time from 0.64 to 7 seconds. Figure III-18 shows the computer diagram for the simulation of the area.

Figure III-19 shows the transients recorded for the simulation of an upper plenum rupture with the control valve closing after the rupture. The hot-spot pressure ($P_{HS}$) transient shows that the valve has little effect until after 4 seconds. After this, $P_{HS}$ begins to increase from the transient without the valve closing (Figure III-14). The hot-spot pressure continues to increase as the valve closes and reaches a maximum of 75 psia at 7.1 seconds. After the valve is closed, the hot-spot pressure stays above the upper plenum pressure

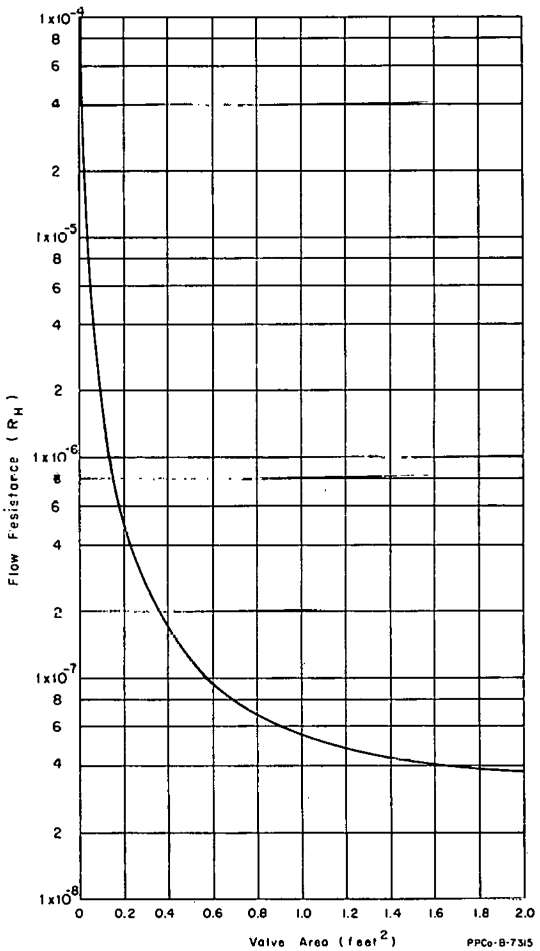

Fig. III-17 Flow resistance ($R_H$) as a function of valve area.

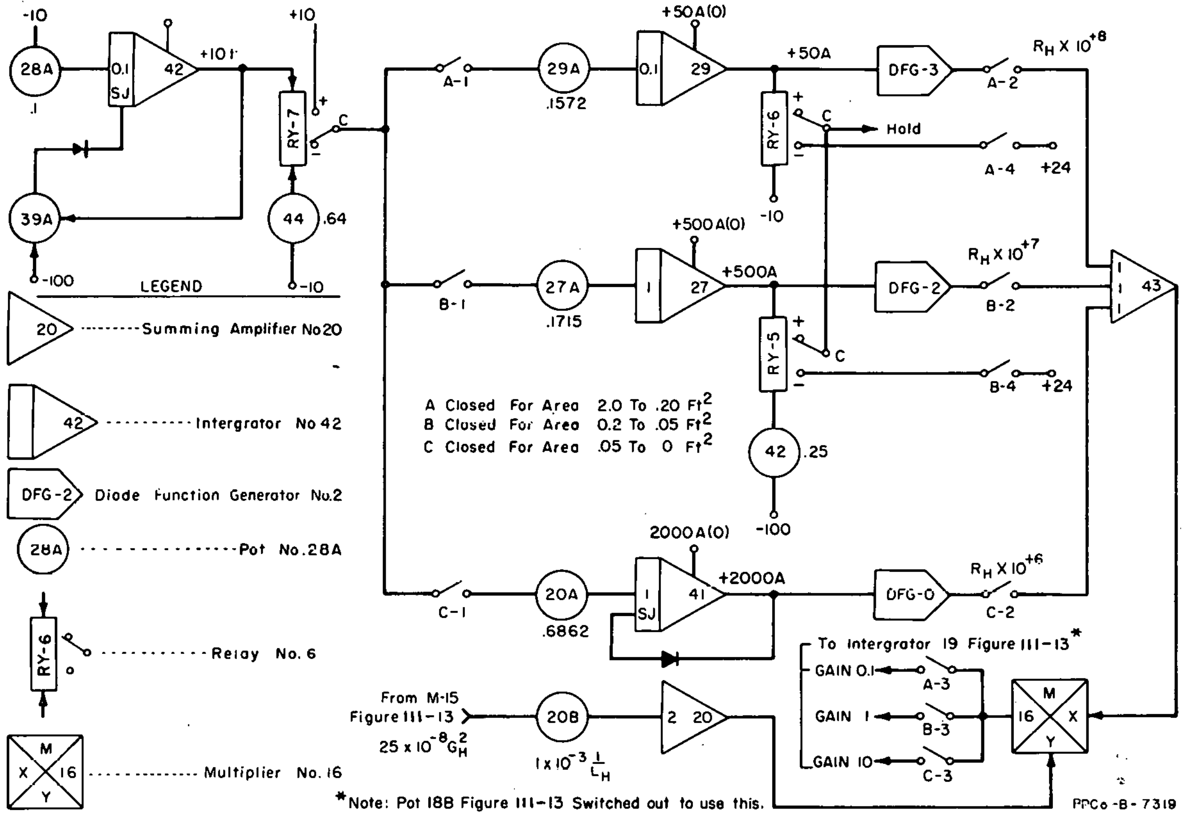

Fig. III-18 Analog computer diagram for simulation of control valve closing.

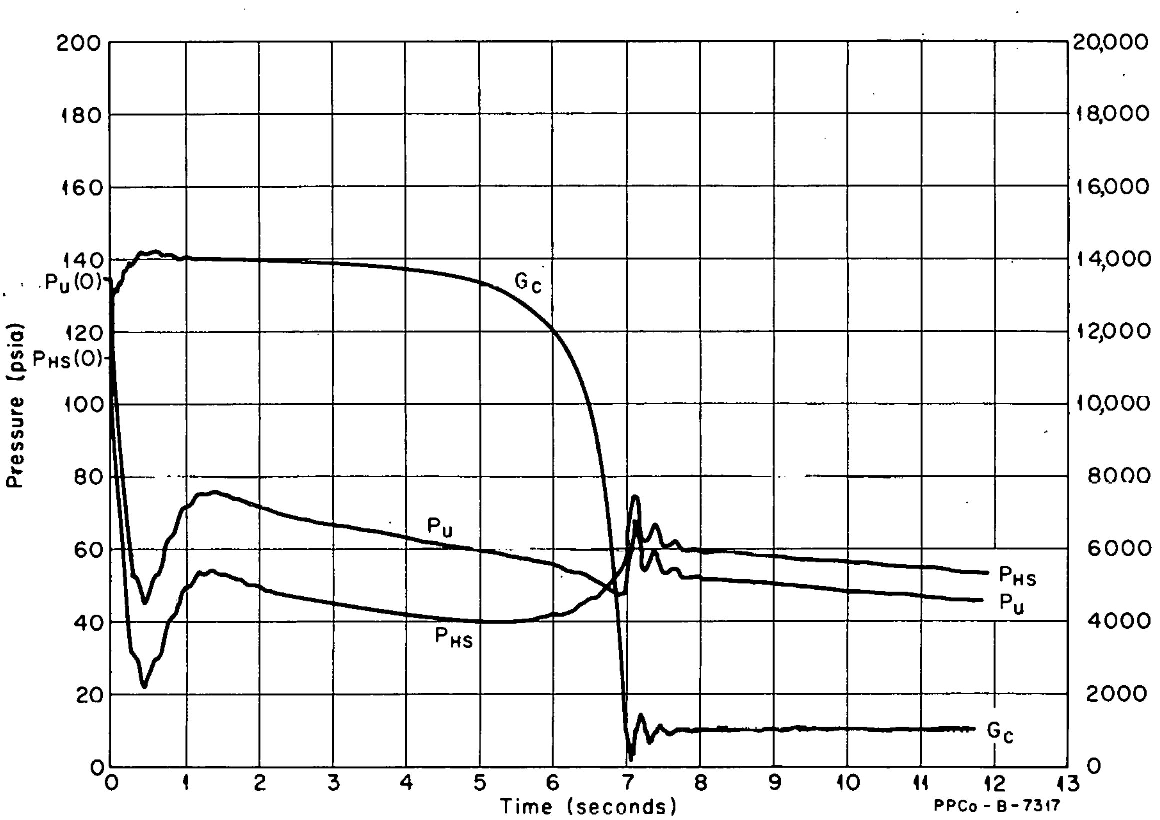

Fig. III-19 Transients with control valve closing after rupture.

because the flow loss is less than the elevation head between the two pressure points.

The reactor core flow ($G_C$) settles out at 1000 gpm after the valve closes because of the bypass around the control valve.

(b) General Conclusions from Detailed Analysis. Increasing the size of the surge tank connecting pipes from 3 to 4 inches keeps the hot-spot pressure from dropping as low at 0.4 second (see Figure III-16).

The comparison of Figures III-14 and -15 shows that an upper plenum rupture has more effect on the hot-spot pressure than a lower plenum rupture.

Closing the control valve does not change the pressure transient significantly until after 4 seconds. After this time, the closing of the valve brings the pressure up some, but the core flow decreases.

## 1.13 Appendix.

### (1) Definition of Terms for Preliminary Analysis.

$P_s$ = surge tank pressure [initial values, $P_s(O) = 120$ psia and $P_s(O) = 200$ psia]

$P_u$ = upper plenum pressure [initial values, $P_u(O) = 120$ psia and $P_u(O) = 200$ psia]

$G_s$ = flow out of surge tank (gpm)

$\dot{G}$'s = time derivatives of the flows ($\frac{\text{gpm}}{\text{sec}}$)

$R_s$ = flow resistance of combined surge tank connecting pipes (for 3-inch pipes, $R_s = 1.18 \times 10^{-5} \frac{\text{psi}}{\text{gpm}^2}$; for 4-inch pipes $R_s = 2.906 \times 10^{-6} \frac{\text{psi}}{\text{gpm}^2}$)

$L_s$ = fluid inertia in surge tank pipes (for 3-inch pipes, $L_s = 1.50 \times 10^{-2} \frac{\text{psi-sec}}{\text{gpm}}$; for 4-inch pipes, $L_s = 8.43 \times 10^{-3} \frac{\text{psi-sec}}{\text{gpm}}$)

$P_r$ = pressure at rupture (psia)

$R_L$ = flow resistance of rupture ($1.33 \times 10^{-5} \frac{\text{psi}}{\text{gpm}^2}$)

$L_L$ = fluid inertia in rupture region ($2.11 \times 10^{-4} \frac{\text{psi-sec}}{\text{gpm}}$)

$P_a$ = atmospheric pressure (15 psia)

$G_{Nu}$ = net flow out of upper plenum (gpm)

$\alpha_u$ = reciprocal of fluid capacitance in upper plenum ($0.318 \frac{\text{psi}}{\text{sec-gpm}}$)

$B$ = bulk modulus of the organic coolant (105,000 psi)

$V_u$ = fluid volume in upper plenum (5500 gal)

$V_s$ = surge tank gas volume [$V_s(O) = 870$ gal for Figure III-6; $V_s(O) = 435$ gal for Figure III-5; $V_s \max = 1500$ gal].

(2) Definition of Terms for Detailed Analysis.

$P_3, P_u, P_L, P_H$ = pressures at nodes defined in Figures III-10 and -11 [initial values $P_3(O) = 135.3$; $P_u(O) = 135$; $P_L(O) = 97$; $P_H(O) = 152.5$ psia]

$P_{LU}, P_{LL}$ = pressures at ruptures (psia)

$P_{U-L}, P_{L-H}, P_{H-3}$ = elevation heads between nodes defined in Figures III-10 and -11 ($P_{U-L} = 2$; $P_{L-H} = 8$; $P_{H-3} = 10$ psi)

$\Delta P_p$ = developed pump pressure (psi)

$P_s$ = surge tank pressure [$P_s(O) = 147.3$ psia]

$P_{u-3}$ = elevation head between surge tank and Node 3 (12 psia)

$P_a$ = atmospheric pressure (15 psia)

$R_3, R_C, R_1, R_H$ = flow resistances between nodes defined in Figures III-10 and -11 $\left[R_3 = 1.531 \times 10^{-9};\ R_C = 2.041 \times 10^{-7};\ R_1 = 3.316 \times 10^{-8};\ R_H \text{ (valve open)} = 3.673 \times 10^{-8} \frac{\text{psi}}{\text{gpm}^2}\right]$

$R_{LU}, R_{LL}$ = upper and lower plenum rupture resistances ($R_{LI} = R_{LL} = 1.33 \times 10^{-5} \frac{\text{psi}}{\text{gpm}^2}$)

$R_s$ = flow resistance of surge tank connecting pipes ($R_s = 1.18 \times 10^{-5} \frac{\text{psi}}{\text{gpm}^2}$ for 3-inch pipes; $R_s = 2.906 \times 10^{-6} \frac{\text{psi}}{\text{gpm}^2}$ for 4-inch pipes)

$L_3, L_C, L_1, L_H$ = fluid inertias between nodes ($L_3 = 1.726 \times 10^{-4}$; $L_C = 5.90 \times 10^{-5}$; $L_1 = 1.546 \times 10^{-3}$; $L_H = 1.677 \times 10^{-3} \frac{\text{psi-sec}}{\text{gpm}}$)

$L_{LU}$, $L_{LL}$ = fluid inertias for upper and lower plenum ruptures ($L_{LU} = L_{LL} = 2.11 \times 10^{-4} \frac{\text{psi-sec}}{\text{gpm}}$)

$L_s$ = fluid inertia in surge tank pipes ($L_s = 1.50 \times 10^{-2}$ for 3-inch pipes; $L_s = 8.43 \times 10^{-3} \frac{\text{psi-sec}}{\text{gpm}}$ for 4-inch pipes)

$G_3$, $G_C$, $G_1$, $G_H$ = flows between nodes [G(O)'s = 14,000 gpm]

$G_{LU}$, $G_{LL}$ = flows out of upper and lower plenum ruptures (gpm)

$G_s$ = flow out of surge tank (gpm)

G's = time derivatives of the flows ($\frac{\text{gpm}}{\text{sec}}$)

$P_a$ = atmospheric pressure (15 psia)

$G_{N3}$, $G_{NU}$, $G_{NL}$, $G_{NH}$ = net flow out of respective volumes (gpm)

$\alpha_3, \alpha_u, \alpha_L, \alpha_H$ = reciprocal of fluid capacitance in respective nodes ($\alpha_3 = 2.531; \alpha_u = 0.3145; \alpha_L = 0.5711; \alpha_H = 0.5956 \frac{\text{psi}}{\text{sec-gpm}}$)

$V_s$ = surge tank gas volume [$V_s(O) = 458$ gal; $V_s \max = 1500$ gal]

$P_{HS}$ = reactor core hot-spot pressure [$P_{HS}(O) = 111.4$ psia]

$P_{u\text{-}HS}$ = elevation head between upper plenum and hot spot (7.767 psi)

$R_{C1}$ = flow resistance from upper plenum to hot spot ($1.531 \times 10^{-7} \frac{\text{psi}}{\text{gpm}^2}$)

$L_{C1}$ = fluid inertia from upper plenum to hot spot ($4.48 \times 10^{-5} \frac{\text{psi-sec}}{\text{gpm}}$)

$R_e$ = equivalent flow resistance of valve and bypass ($\frac{\text{psi}}{\text{gpm}^2}$)

$R_v$ = valve flow resistance ($\frac{\text{psi}}{\text{gpm}^2}$)

$R_B$ = bypass flow resistance (7.803 x $10^{-5} \frac{\text{psi}}{\text{gpm}^2}$)

k = constant (2.469 x $10^{-8}$)

A = effective area of valve ($A_{max} = 2$ ft$^2$)

$R_H'$ = flow resistance excluding valve and bypass (3.163 x $10^{-8} \frac{\text{psi}}{\text{gpm}^2}$).

## 1.2 Modified ETR Water Loop Transient Analysis (J. W. Sielinsky, F. K. Hyer)

1.21 Introduction. The purpose of this analysis was to determine the transients in the modified ETR water loop system caused by a 3/8-inch rupture in the piping (Figure III-20). The transient of most importance is the burnout ratio in the water loop test section. Transients were recorded for both instantaneous and 10-msec ruptures with initial loop flows of 100, 125, and 150 gpm.

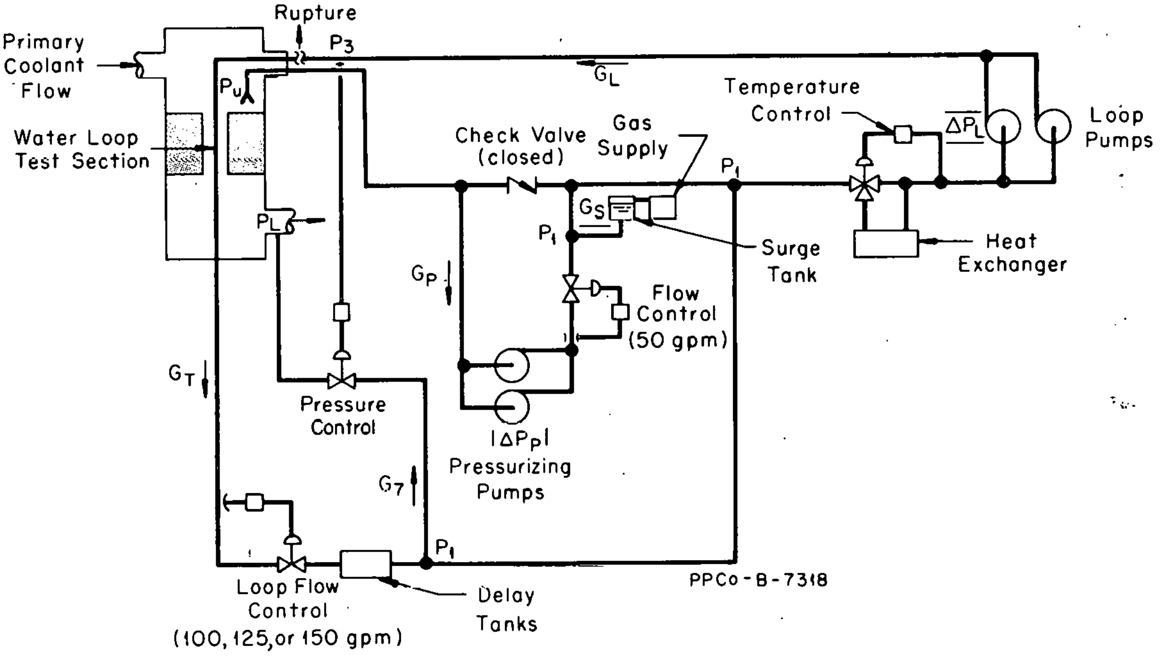

Fig. III-20 Modified ETR water loop system.

1.22 Analog Computer Simulation. The drawing of the modified ETR water loop system is shown in Figure III-20. The flow diagram representing the system is shown in Figure III-21.

The assumptions made in the simulation are:

(1) The pressure in the reactor primary coolant system is not disturbed by the rupture in the water loop

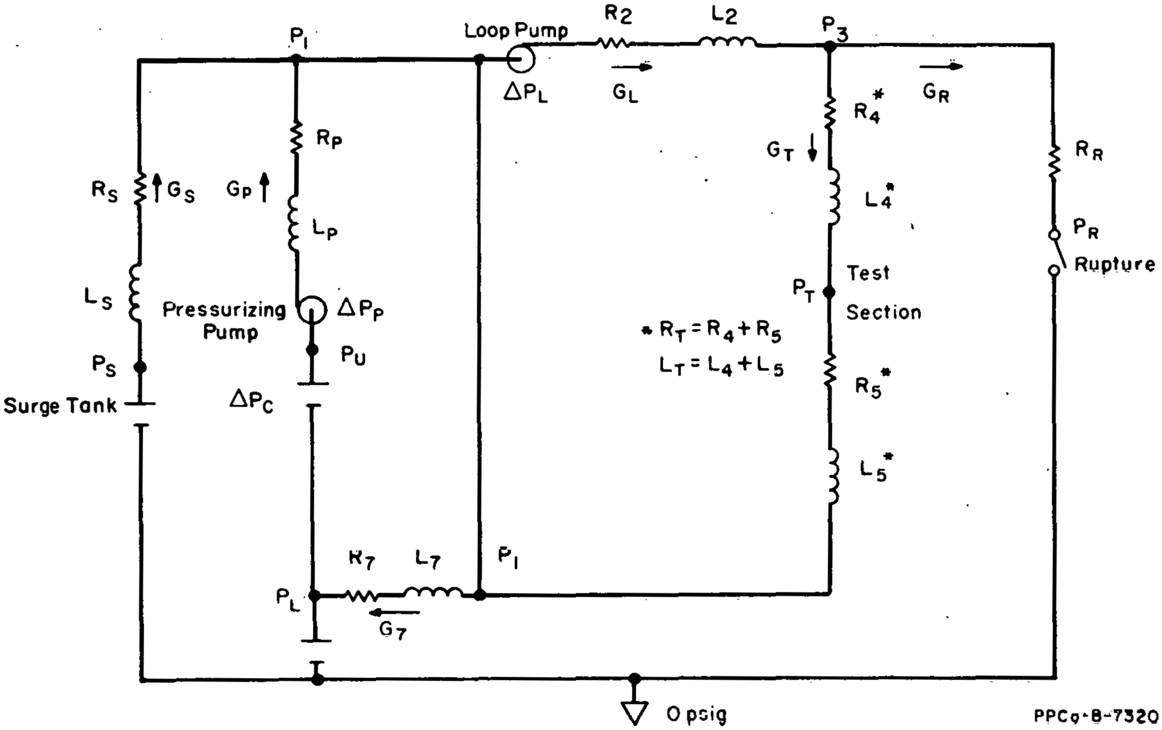

Fig. III-21 Flow diagram of system.

(2) The pressure in the surge tank is held constant by the regulated gas supply

(3) The control valves in the system do not change during the time that is of interest

(4) The compressibility effect of the fluid can be neglected

(5) The fluid inertia effect in the region of the rupture is small compared to the flow resistance effect.

The equations describing the fluid dynamics in the system (see Figure III-21 and Section III-1.23, Appendix) are as follows:

$$P_s - P_1 = R_s G_s^2 + L_s \dot{G}_s^2 \tag{34}$$

$$P_L + \Delta P_c + \Delta P_p - P_1 = R_p G_P^2 + L_p \dot{G}_P \tag{35}$$

$$P_1 + \Delta P_L - P_3 = R_2 G_L^2 + L_2 \dot{G}_L \tag{36}$$

$$P_3 - P_R = R_R G_R^2 \tag{37}$$

$$P_3 - P_1 = R_T \dot{G}_T^2 + L_T \dot{G}_T \tag{38}$$

$$P_1 - P_L = R_7 G_7^2 + L_7 \dot{G}_7 \qquad (39)$$

$$G_L = G_s + G_P + G_T - G_7 \qquad (40)$$

$$G_L = G_R + G_T \ . \qquad (41)$$

The equation for the calculation of the test section pressure is

$$P_T = P_3 - R_4 G_T^2 - L_4 \dot{G}_T \ . \qquad (42)$$

The developed pressure across the pressurizing pumps is

$$\Delta P_p = \Delta P_{po} - R'_p G_P^2 \ . \qquad (43)$$

This equation was calculated from a curve fit of the predicted pump performance curve.

The developed pressure across the loop pumps calculated from the pump curve is

$$\Delta P_L = \Delta P_{Lo} - R_L G_L \ . \qquad (44)$$

For a rupture,

$$P_R = P_{atmosphere} \ . \qquad (45)$$

For the instantaneous ruptures, the rupture flow resistance ($R_R$) is held constant. For the time constant ruptures, $R_R$ is a function of time. The resistance is proportional to the reciprocal of the rupture area squared, or

$$R_R = \frac{k}{A_R^2} \qquad (46)$$

and the area is assumed to open up on a first-order time constant,

$$A_R = A_{max} \ (1 - e^{t/\tau}) \qquad (47)$$

where $\tau$ is defined as the time constant.

The equations used for the calculations of the test section burnout ratios are (see Section III-1.23 Appendix, for definition of terms):

$$R_{B.O.} = \frac{q/A \ (B.O.)}{q/A \ (max)} \qquad (48)$$

$$q/A(max) = q/A \ (nominal \ max) \ f' \ (q/A) \qquad (49)$$

$$q/A(B.O.) = 1.8 \left[0.6h_{(B.O.)}\right] \left[T_{W_{(B.O.)}} - T_b\right] \tag{50}$$

$$h(B.O.) = 10{,}890 \left\{ \frac{D_e(\text{min})}{D_e(\text{min}) + D_i(\text{max})} + \frac{48V(\text{min})}{[D_e(\text{min})]\ 0.6} \right\} \tag{51}$$

$$T_{W_{(B.O.)}} = 57 \ln P - 54(P/P + 15) - V(\text{min})/4 \tag{52}$$

$$T_b = \frac{1}{1.8} \left(T_{in} + 3 + \Delta T_b F_b - 32\right) \tag{53}$$

$$\Delta T_b = \frac{(q/A)A}{W_N C_P} \quad . \tag{54}$$

The above equations were simulated on the analog computer, and transients were recorded for various conditions (Figures III-22 through -27). The transients that were recorded are the test section pressure, ($P_T$), the test section flow, ($G_T$), the rupture flow, ($G_R$), and the test section burnout ratio, (R).

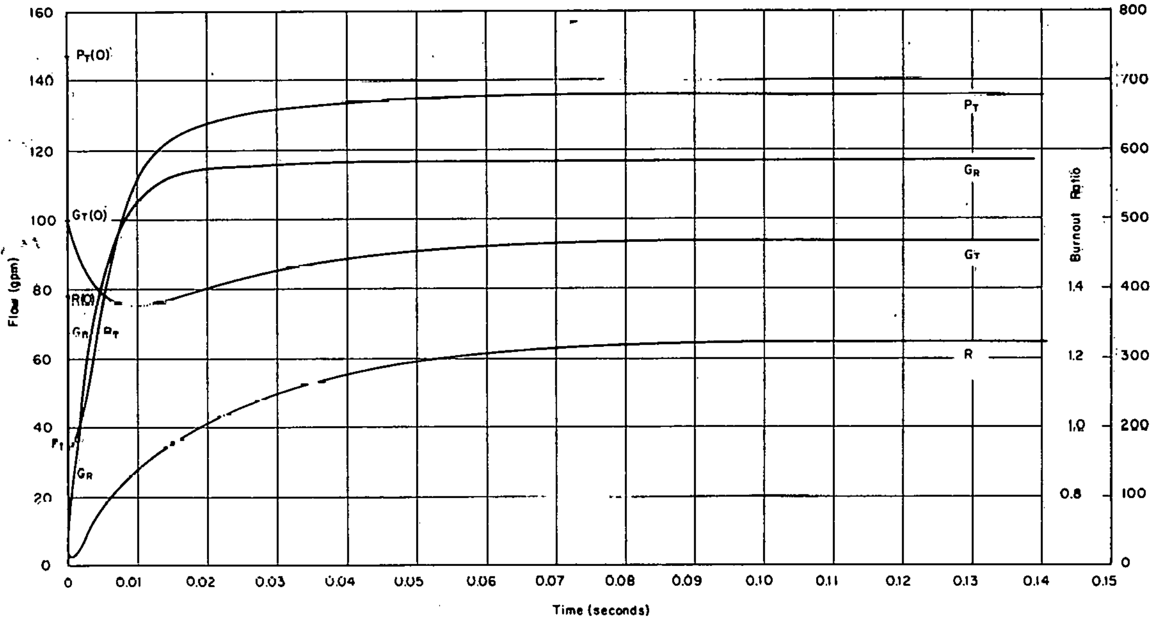

Fig. III-22 Instantaneous rupture at $G_T(O)$ = 100 gpm.

Figure III-22 shows the transients for an instantaneous rupture with the initial flow at 100 gpm. The burnout ratio drops to 0.62 at 0.5 msec and then goes above one at 19 msec. The reason the burnout ratio drops during the first part of the transient is that the flow from the surge tank is not able to keep up with the flow out of the rupture. The burnout ratio then increases as the surge tank flow increases.

Figure III-23 shows the transients for a 10-msec rupture with the initial flow at 100 gpm. The burnout ratio drops slightly below one at 11 msec then increases above one at 19 msec. The burnout ratio does not drop as low for the 10-msec rupture because the surge tank flow is able to follow the rupture flow better.

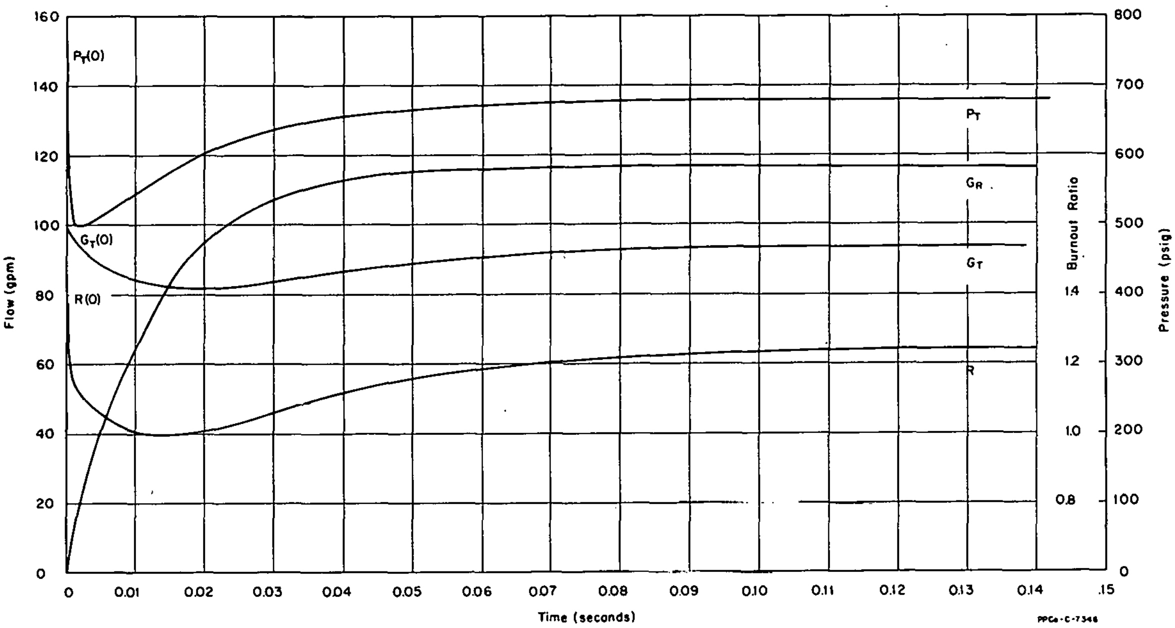

Fig. III-23 10-msec rupture at $G_T(O)$ = 125 gpm.

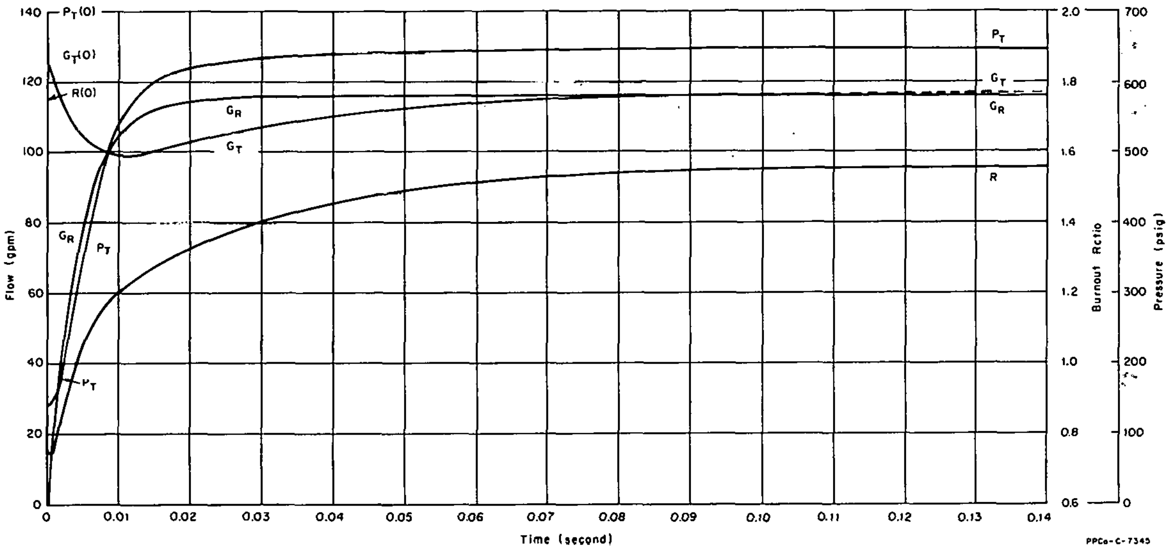

Fig. III-24 Instantaneous rupture at $G_T(O)$ = 125 gpm.

Figures III-24 and -25 show the transients for the instantaneous and 10-msec ruptures, respectively, with the initial flow at 125 gpm. For the instantaneous rupture, the burnout ratio goes above one at 4 msec. For the 10-msec rupture, it only drops to a minimum of 1.32.

Figures III-26 and -27 show the transients for the instantaneous and 10-msec ruptures, respectively, with the initial flow at 150 gpm. For the instantaneous rupture, the burnout ratio goes above one at 2.2 msec; and for the 10-msec rupture, it drops to a minimum of 1.62.

For the higher initial flows, the burnout ratio does not drop as low because the higher flow is able to remove more heat from the test section than the lower flow can remove.

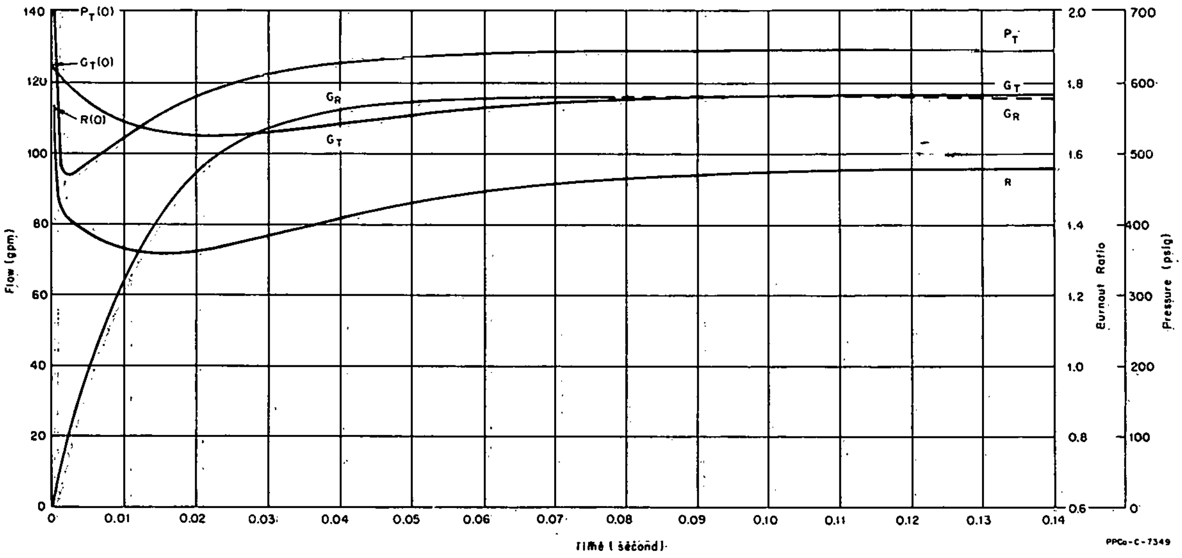

Fig. III-25. 10-msec rupture at $G_T(0)$ = 125 gpm.

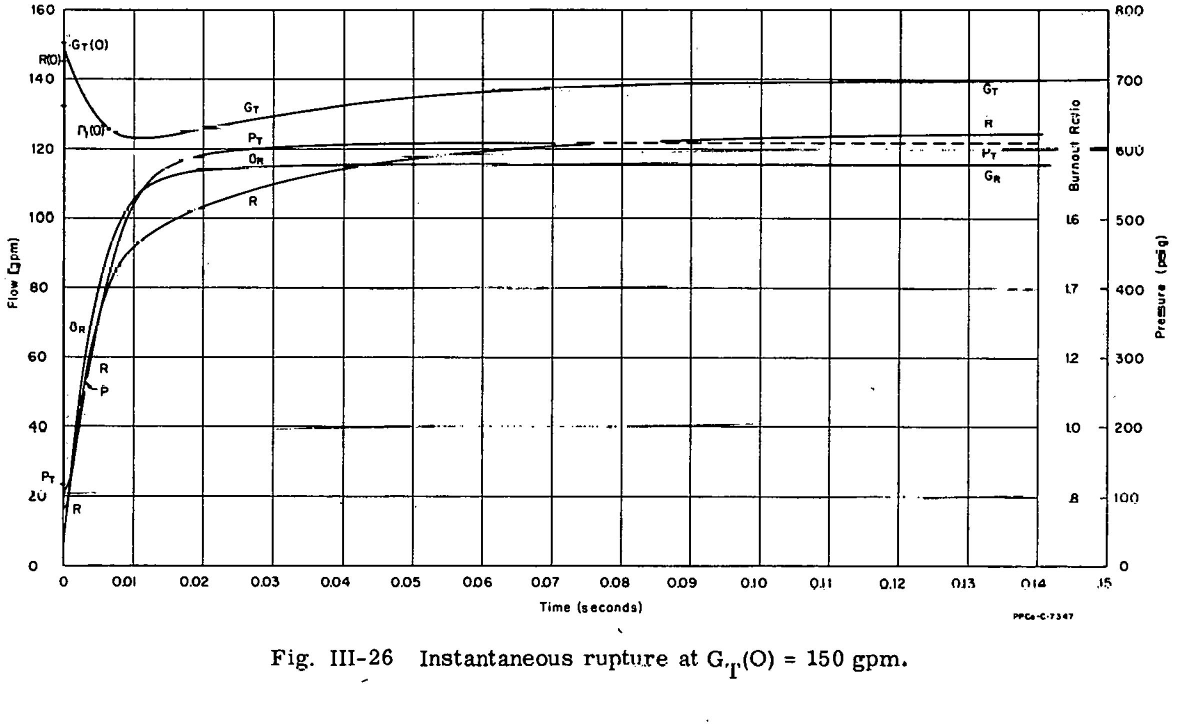

Fig. III-26 Instantaneous rupture at $G_T(0)$ = 150 gpm.

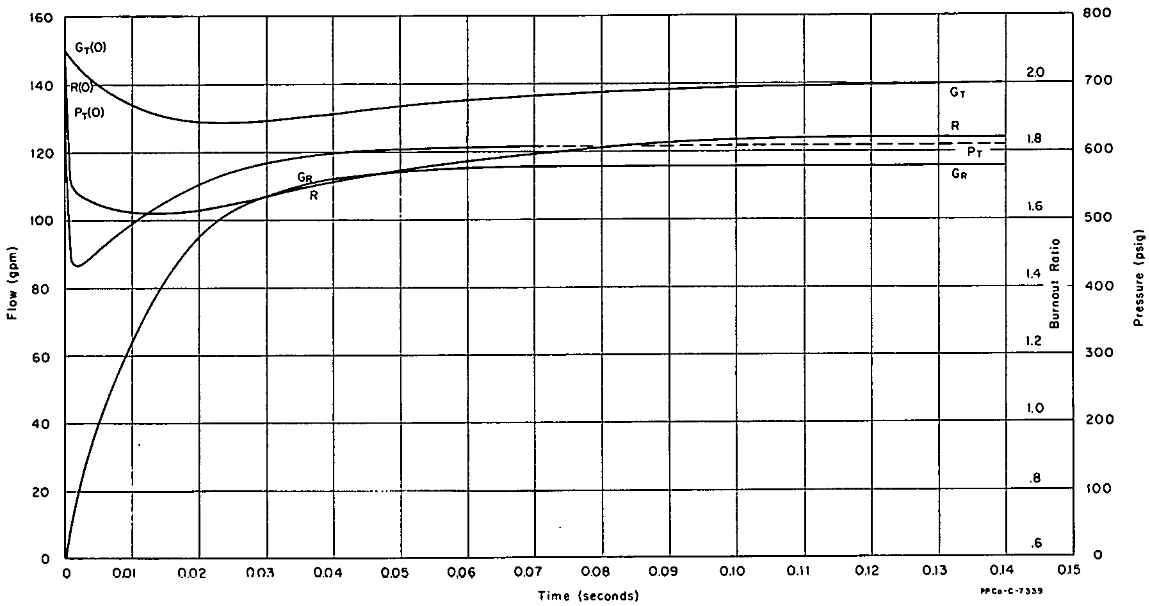

Fig. III-27 10-msec rupture at $G_T(O)$ = 150 gpm.

### 1.23 Appendix.

#### (1) Definitions for Fluid Dynamics Equations.

$P_3$ = surge tank pressure (478 psig)

$P_1$, $P_L$, $P_3$ = pressures at respective nodes in Figures III-20 and -21 (psig)

$\Delta P_c$ = pressure drop across reactor core (65 psi)

$\Delta P_p$ = developed pressure across pressurizing pumps

$\Delta P_{po}$ = no flow developed pressure across pressurizing pumps (293.5 psi)

$\Delta P_L$ = developed pressure across loop pumps

$\Delta P_{Lo}$ = no flow developed pressure across loop pumps (331.6 psi)

$P_R$ = pressure at region of rupture

$P_L$ = reactor vessel lower plenum pressure (135 psig)

$P_T$ = water loop test section pressure

$R_s$ = surge tank connecting pipe flow resistance ($3.2 \times 10^{-3} \frac{\text{psi}}{\text{gpm}^2}$)

$L_s$ = surge tank connecting pipe fluid inertia ($2.17 \times 10^{-2} \frac{\text{psi-sec}}{\text{gpm}}$)

$R_P, R_2, R_T, R_7$ = flow resistances between nodes in Figure III-21 ($R_P = 1.0 \times 10^{-2}$; $R_2 = 5.4 \times 10^{-4}$; $R_T = 3.5 \times 10^{-2}$ for initial flow of 100 gpm; $R_T = 1.935 \times 10^{-2}$ for initial flow of 125 gpm; $R_T = 1.304 \times 10^{-2}$ for initial flow of 150 gpm; $R_7 = 1.38 \times 10^{-1} \frac{\text{psi}}{\text{gpm}^2}$)

$L_P, L_2, L_T, L_7$ = fluid inertia between nodes in Figure III-22 ($L_P = 8.178 \times 10^{-2}$; $L_2 = 3.65 \times 10^{-2}$; $L_T = 8.19 \times 10^{-2}$; $L_7 = 4.95 \times 10^{-2} \frac{\text{psi-sec}}{\text{gpm}}$)

$R_R$ = rupture flow resistance ($5.32 \times 10^{-2} \frac{\text{psi}}{\text{gpm}^2}$) for instantaneous rupture; variable from infinity to $5.32 \times 10^{-2} \frac{\text{psi}}{\text{gpm}^2}$ for time constant rupture)

$R_4$ = flow resistance from node 3 to test section ($5.0 \times 10^{-3} \frac{\text{psi}}{\text{gpm}^2}$)

$L_4$ = fluid inertia from node 3 to test section ($3.46 \times 10^{-2} \frac{\text{psi-sec}}{\text{gpm}}$)

$R_p'$ = equivalent flow resistance for pressurizing pumps ($5.2 \times 10^{-3} \frac{\text{psi}}{\text{gpm}^2}$; $R_p'$ is included in $R_p$)

$R_L$ = equivalent flow resistance for loop pumps ($1.66 \times 10^{-1} \frac{\text{psi}}{\text{gpm}^2}$; $R_L$ is included in $R_2$)

$G_s$ = flow from surge tank (gpm)

$G_P, G_L, G_T, G_7$ = flow between nodes in Figure III-21 (initial value for $G_P$ and $G_7$ is 50 gpm; initial values for $G_L$ and $G_T$ are 100, 125, or 150 gpm)

$G_R$ = flow out of the rupture (gpm)

G's = the derivatives of the respective flows $(\frac{gpm}{sec})$

k = proportionality constant $(3.126 \times 10^{-8})$

$A_R$ = effective area of the rupture $(A_{max} = 7.666 \times 10^{-4}\ ft^2)$.

(2) Definitions for Burnout Equations.

$R_{B.O.}$ = burnout ratio

q/A(B.O.) = heat flux which would cause burnout $(\frac{Btu}{hr\text{-}ft^2})$

q/A(max) = maximum existing heat flux in hot channel $(3.175 \times 10^{+6} \frac{Btu}{hr\text{-}ft^2})$

q/A(nominal max) = maximum existing heat flux in nominal channel

f'(q/A) = conversion factor from nominal channel to hot channel (1.27)

$h_{(B.O.)}$ = heat transfer coefficient

$T_{W_{(B.O.)}}$ = burnout temperature of test section wall

$T_b$ = temperature of coolant

$D_e$(min) = equivalent diameter of the minimum area test section channel (0.0148 ft)

$D_i$(max) = heated perimeter of test section channel divided by $\pi$ (0.0529 ft)

V(min) = minimum fluid velocity in test section channel $(V_{min} = 0.415\ G_T \frac{ft}{sec})$

P = test section pressure in absolute units $(P_T = P + 12.5;$ $57 \ln P - 54 \frac{P}{P + 15}$ was simulated on a function generator)

$T_{in}$ = temperature of inlet coolant (250°F)

$\Delta T_b$ = bulk temperature rise across test section (°F)

$F_b$ = hot channel factor (1.68)

$A$ = test section cross-sectional area (0.24 $ft^2$)

$W_N$ = flow through nominal channel ($W_N = 75\ G_T\ \frac{lb}{hr}$)

$C_P$ = specific heat of coolant (1.0 $\frac{Btu}{lb\text{-}°F}$).

## 2. DETECTOR DEVELOPMENT
(S. D. Anderson)

### 2.1 ATR Fuel Plate Deflection Test (R. L. Kindred, A. W. Hauf, R. P. Morrell)

A test was made in the ATR hydraulic flow loop facility on an ATR fuel element to determine fuel plate vibration amplitudes and frequencies at 150°F and at various flow rates up to 1100 gal/min. The vibration was measured with Microdot weldable strain gages. The gages were spot-welded to the fuel plates in the lateral direction with center of the gage on the longitudinal center line.

The instrumented fuel element is shown in Figure III-28. Two special Microdot, Type SG-113/1-2A-10-6061T6, integral-lead, weldable strain gages can be seen installed on plate No. 19. These gages consist of the basic temperature-compensated Microdot gage for aluminum with 10 feet of 0.062-inch-diameter, 3-conductor, MgO-insulated, stainless steel sheathed cable attached to the gage by a stainless steel tube coupling section. The lead cables were fastened to the plates with 3/16-inch-wide, 0.003-inch-thick, gold-alloy brackets spaced about 2 inches apart. The cables were then cemented to the plate with Stycast-2651 epoxy. This type gage is suitable for installation on plate No. 19 only, due to the limitation of the length of the coupling section which makes the

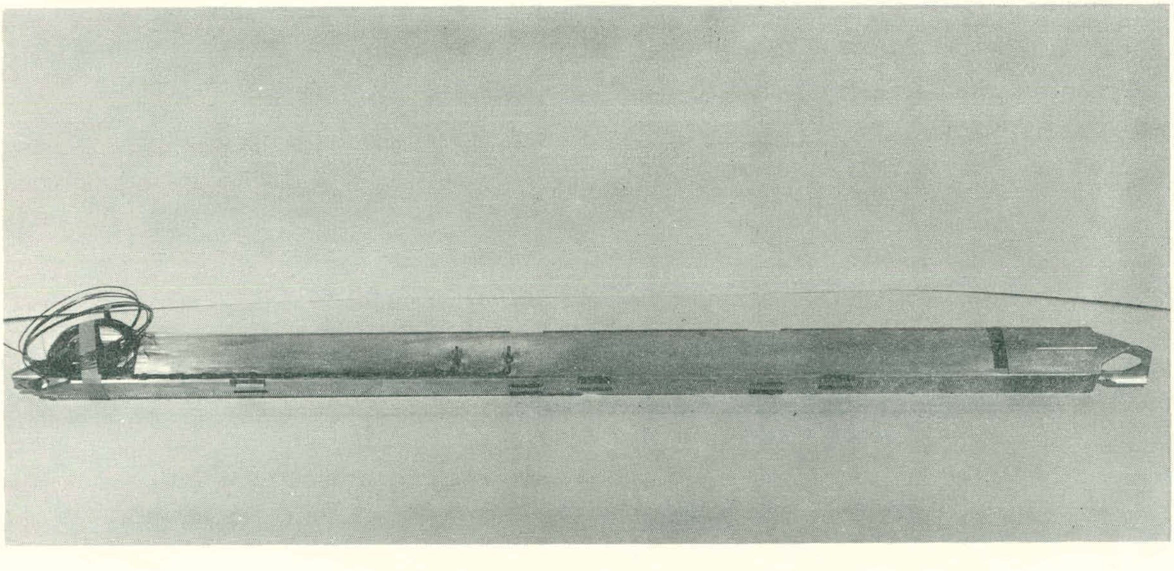

Fig. III-28 Instrumented fuel element.

total length of the gage installation too long to install in a lateral direction on the internal plates.

Internal plates Nos. 18, 17, and 2 were instrumented with two Microdot weldable strain gages each. These were the basic gages mentioned above. Three ten-foot lengths of 0.020-inch diameter, single-conductor, Teflon-insulated, stainless steel sheathed cable in a three-wire configuration were used for lead wires for each gage. They may be seen at the bottom edge of the element in Figure III-28. The lead cables were fastened along the edge of the plates in the same manner as the cables on plate No. 19 except that the brackets were about 4 inches apart. Clearance was left along the edges of the plates for the later swaging operation to insert the plates in the element. EPY-400 was used to cement the cables to the plate. After the gages and lead wire tabs were installed and connected to the cables, the connection and gages were waterproofed with General Electric, RTV-20, silicon rubber. A special vacuum chamber was used to evacuate the air bubbles from the silicon rubber. After evacuation, the installations were oven-cured at about 300°F. A 0.003-inch-thick, gold-alloy shield was welded over the installation. More RTV-20 silicon rubber was applied and the gage installation was again evacuated and oven-cured. Nominal thickness of the gage and lead wire installations was limited to 45 mils due to the channel thickness of 70 mils.

Electronic test equipment used for the flow test included an electronic console containing ten channels of low-level dc amplifiers and galvanometer drivers. Other equipment used for the flow test were a Honeywell Visicorder oscillograph; eight operational amplifiers; an Ampex, Type CP-100, tape recorder; a ten-channel, strain-gage, bridge-completion unit; and two dual-pen, strip-chart recorders. A block diagram of the electronic test equipment is shown in Figure III-29.

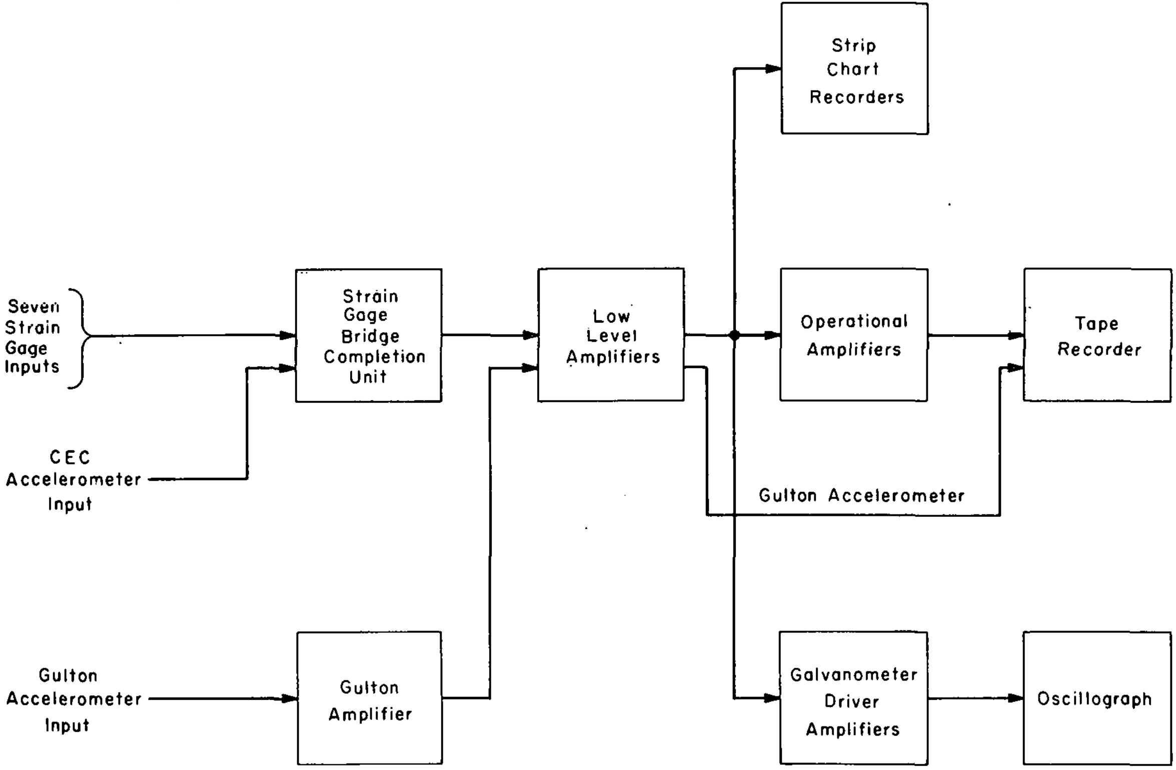

Fig. III-29 Block diagram of electronic test equipment.

The strain gage signals were amplified by the low-level amplifiers and simultaneously fed to the operational amplifiers, the Visicorder driver amplifiers, and the strip-chart recorders. The operational amplifiers utilized a high-pass filter to eliminate the static dc signal and to allow the tape recorder to receive a high-level dynamic signal. Various operational and low-level amplifier gains were used to maintain the high-level input for all flows. The strip-chart recorders were used to measure the static plate deflection signals. The Visicorder was used to monitor all of the signals including two accelerometers. The accelerometers were mounted on the flow loop at approximately the level of the test element to measure the loop equipment vibrations.

The flow test was made principally for measuring the vibration of the plates. In the interest of accomplishing this purpose, the flows were held at each flow rate only long enough to set amplifier gains and record the vibration. Then the flow was increased to the next higher flow rate. To measure static plate deflection accurately, the flow should be reduced to zero after each flow level to check the dc offset and rezero the bridges. This procedure subjects the strain gauges to greater stress during the testing period and, therefore, was not used for this test. Measurements of static plate deflection on two plates were obtained.

The flow was run at intervals of 200, 400, 600, 700, 800, 850, 900, 950, 1000, 1100, and back to 740 gpm. The 740-gpm flow corresponds to 100-psi drop across the element. The data on the Visicorder and the strip-chart recorders were continuous. Data were recorded on the magnetic tape recorder at zero flow, pump on and pump off, and at each flow rate given above.

The magnetic tape recorder data for strain gage No. 4 on plate No. 18 and the two accelerometers for zero flow, pump on and pump off, 200-, 400-, 600-, 700-, 900-, 1100-gpm flow rates were analyzed with a General Radio, Type 1900-A-Wave Analyzer. The strain gage spectra showed that the pertinent information was in the region below 4 kc/sec and that the principal peak frequency was linearly proportional to flow rate. This relationship with flow rate also may be seen in the spectra of the accelerometers; however, it is not as easily defined because the spectra are more complex. These data agree fairly well with frequency information obtained from the strain gage peak-to-peak amplitude data discussed later.

Figure III-30 shows the portion of the strain gage spectra of interest for zero flow, pump off, 200-, 400-, 700-, 900-, and 1100-gpm flow rates. The shaded area of the spectra shows the linear relationship of the principal frequency peak to the flow rate. The amplitudes shown in Figure III-30 are not absolute values since they were not adjusted for the system amplifier gains. The spectra were run with a 50 cycles/sec bandwidth. The smaller peaks at frequencies above 5 kc/sec remain approximately the same in frequency and amplitude for zero flow, pump off, and all flow rates. This indicates that these peaks are not vibration information, but are due to interference pick-up in the electronics from some unknown source.

Peak-to-peak plate vibration versus flow rate curves are shown in Figure III-31. Peak-to-peak amplitudes of strain were obtained from the tape recording. These values were then converted to peak-to-peak fuel plate vibration by multiplying the transverse plate deflection per lateral strain conversion constants. The constants were determined during previous tests in which a correlation

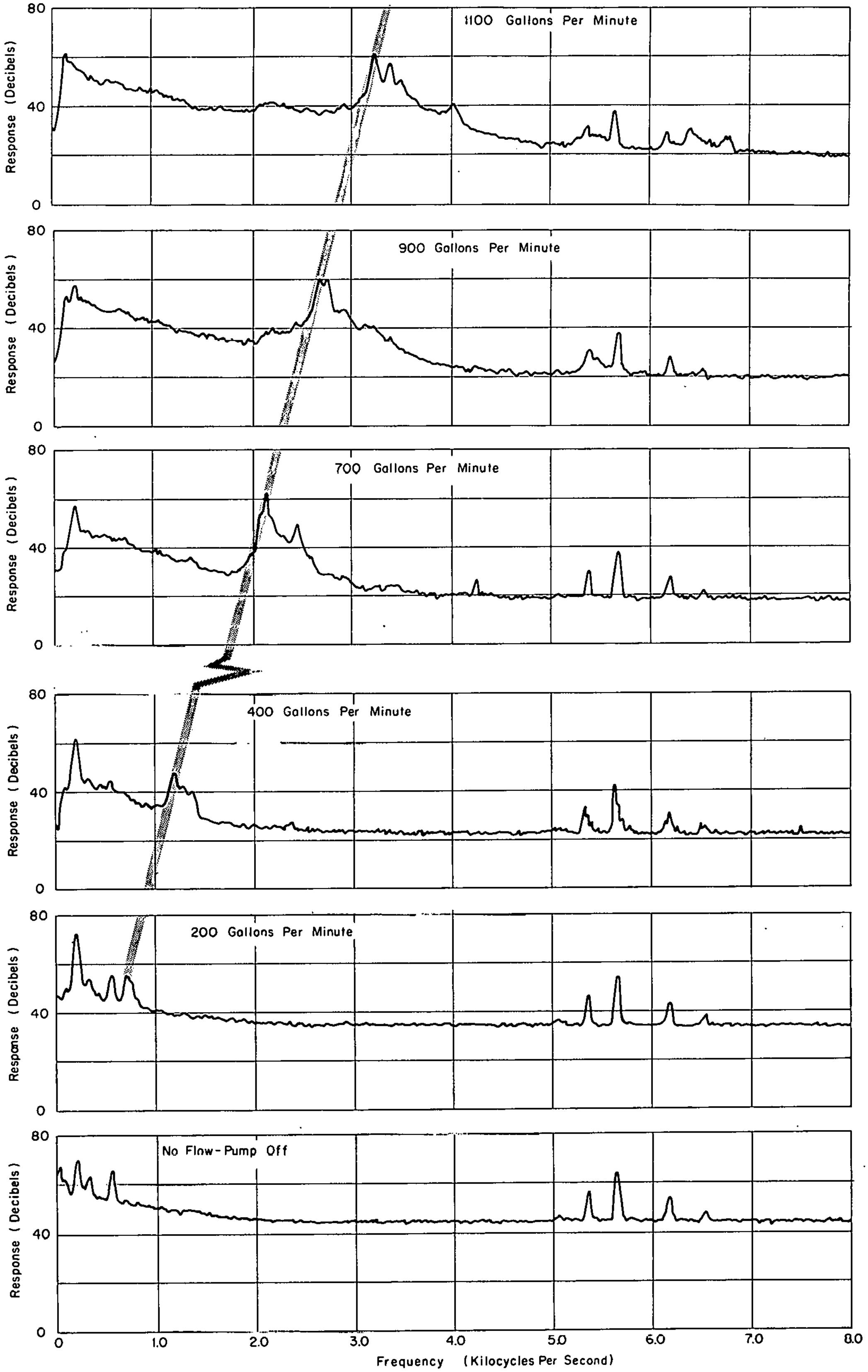

Fig. III-30 Strain gage spectra for several flow rates.

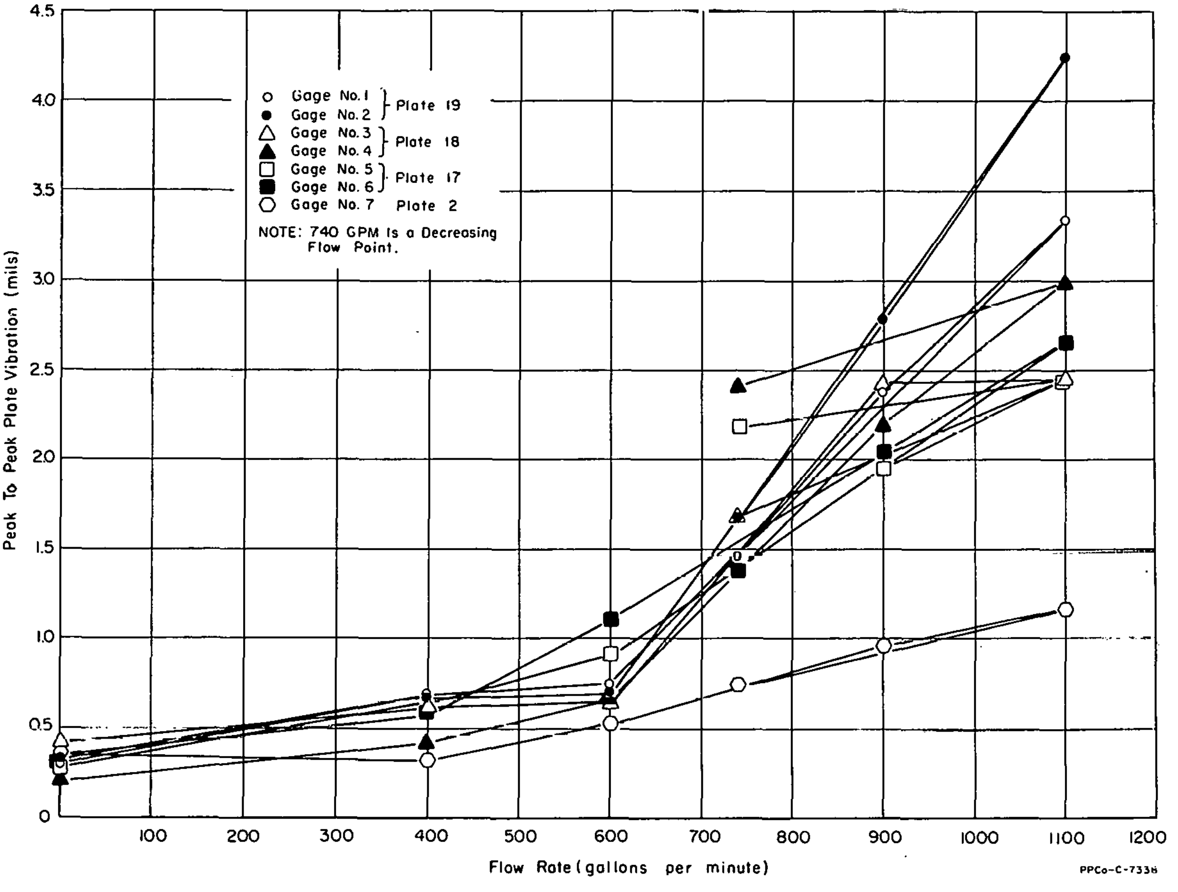

Fig. III-31 Peak-to-peak flow vibration versus flow rate.

between transverse plate deflection dial gage measurements and lateral strain measurements were obtained by applying internal pressure to an element. This method of obtaining the conversion constants for plates Nos. 1 and 19 has been previously reported [1].

The principal frequencies were less than 4 kc which are much lower then the theoretically calculated natural plate vibration frequencies. There is a possibility that the vibration of the plates may be due to some driving source such as valve flutter of the bypass valve.

## 2.2 Autoclave Material Tests (W. A. Niethammer)

A search for suitable electrical insulations for use in high-temperature steam and water environments is currently being conducted. Insulating materials are being evaluated that will withstand steam-water environment at greater than 400°F with special emphasis on finding a material that will withstand the 600°F environment of LOFT. Specific applications are insulation of two-phase conductivity probes, waterproofing of conventional and flame-sprayed strain gauges, and survey of high-temperature insulated wires for water immersion.

Short-term tests were conducted in a saturated water autoclave. Except for the insulated wires, the insulations tested thus far have been those which can be applied by spraying, dipping, or brush methods because of their ease of application and wide utility. However, other techniques such as pressure molding and melting of fused glass and ceramics are being considered.

To date no insulation material, except extruded Teflon, has exceeded 550°F. The materials tested which have obtained success at greater than 400°F are given in Table III-1. These materials were used to coat the end of an MgO-insulated, Type 304 stainless steel sheathed cable or to coat the length of a solid Type 304 stainless steel rod. Insulation resistance was measured between the cable wire or rod and the autoclave wall. A resistance less than one megohm was recorded as failure. The insulated wires were simply looped in and out of the autoclave; the same resistance measurement was made.

TABLE III-1

ELECTRICAL INSULATING MATERIALS
FOR TEMPERATURES GREATER THAN 400°F

| Insulation | Company | Temperature (°F) |
|---|---|---|
| Pyroceram No. 95 | Corning Glass | 450 |
| Epoxylite No. 813-9 | Epoxylite | 420 |
| RTV-106 | General Electric | 485 |
| Pyre-M.L. RC-5060 | DuPont | 450 |
| Pyre-M.L. RK-692 | DuPont | 475 |
| Pemco S-910 | Glidden | 470 |
| Wire-Silastic 1601 | Dow Corning | 430 |
| Wire-Silastic 1602 | Dow Corning | 530 |
| Wire-Teflon | DuPont | 600 |
| Wire-H Firm (Pyre-M.L. 692) | Haveg - Super Temp | 540 |

Several other materials have yet to be tested. Further tests on Pemco and Pyre-M.L. materials, fabricated by different techniques, will be conducted to determine if satisfactory performance can be obtained at higher temperatures. Spray coating of Teflon and pressure molding of Teflon and Silastic 1602 are being considered. Fused glasses from Corning Glass and fused ceramincs and potting compounds from Physical Sciences are scheduled for testing. Further insulated wire tests of Teflon and H-Film (Pyre-M.L. base) from other suppliers are included.

In summary, no electrical insulation material has yet been found that is applicable to the 600°F environment of LOFT. Extruded Teflon is suitable as an electrical wire insulation for the nonnuclear LOFT tests, but cannot be used in the nuclear test because of its radiation-damage characteristics.

## 2.3 Drag Disk Flow Meter (W. A. Niethammer)

A drag disk flow meter has been developed for use in the LOFT program. The device, shown in Figure III-32, is a circular disk at the end of a cantilever beam. Strain gages mounted on the beam measure the force on the disk due to drag, which is related to flow rate.

The drag disk is a point-velocity measurement device rather than one that averages flow rate across the channel. However, when it is calibrated, it does measure total flow with reasonable accuracy and does provide reproducible results. The drag disk has better dynamic response than does a differential pressure device such as an orifice. The meter meets requirements for durability primarily because of its strength and the absence of moving parts.

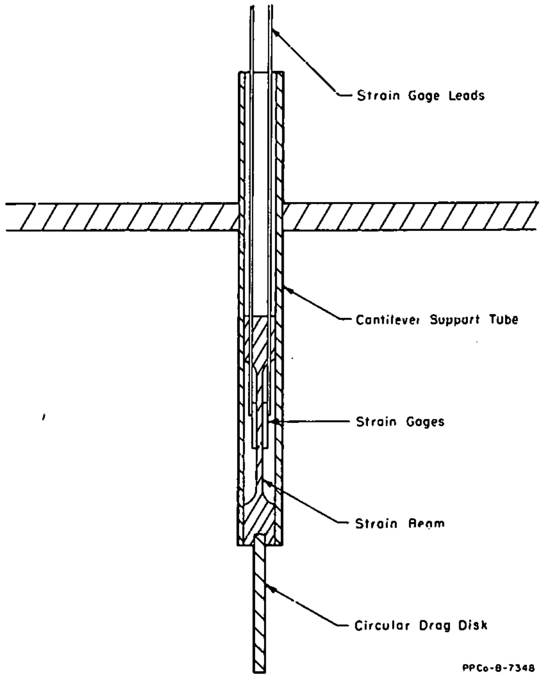

Fig. III-32 Drag disk flow meter.

Few reports of such a drag disk meter have been written. A related device has been briefly mentioned in connection with vane-type and ultrasonic flow meters which utilize the deflection principle. Gibson[2] and his co-workers used a drag disk meter with good results.

The drag force caused by flow around a submerged body is given by the equation [3]

$$F_D = \frac{C_D A_P \rho V^2}{2g_c}$$

where

$F_D$ = drag force, $lb_f$

$C_D$ = drag coefficient, dimensionless

$A_P$ = projected area normal to flow, $ft^2$

$\rho$ = fluid density, $lb_m/ft^3$

$V$ = fluid velocity, ft/sec

$g_c$ = acceleration constant, $32.2 \frac{ft\text{-}lb_m}{lb_f\text{-}sec^2}$.

For a circular disk normal to the flow direction, the drag coefficient remains constant for Reynold's numbers greater than $10^3$. Consequently, the drag force and, thus, strain in the cantilever support beam is predicted to be directly proportional to the square of velocity.

Prototypes of the drag disk were constructed by Detector Development for testing in the laboratory flow loop. These first devices consisted of a stainless steel circular disk welded to stainless steel shim stock. Foil strain gages were mounted on opposite sides of the shim stock with EPY-400 cement and waterproofed with RTV-60 silicon. Three disk diameters, 0.562, 0.75, and 0.931 inch, were used. The pipe diameter of the loop was 2.5 inches ID.

Static weight tests were conducted to determine the strain output in relation to the drag force. Results were within five percent of values predicted by cantilever beam theory. Flow tests were conducted to verify the drag-force theory. Flow rates were measured by a Foxboro, square-edged, concentric orifice. All three meters deviated from the predicted theory by 15 to 20 percent at a flow rate of 40 gpm. This deviation from theory was expected for two reasons: (a) the influence of the pipe wall creates a velocity profile different than the uniform velocity of an infinite medium on which the theory is based, and (b) the drag coefficient undoubtedly deviates from that of a circular disk or flat plate in a true infinite medium and possibly varies with Reynold's number. The calibration of flow rate against strain output gave a linear log-log plot for all three disks with very little scatter. The slope varied from 1.86 and 1.93 in all tests regardless of whether the disks had square or rounded edges. Theory for flow in an infinite medium predicts a slope of 2.0.

The effect of angle of incidence of flow direction on the disk also was studied by Detector Development. It was found that the results followed the cosine curve up to an angle of 40 degrees as measured from the normal position. That is, the projected area, $A_P$, becomes $A_{Disk}\cos(\theta)$. Fage and Johansen [4] found similar results for a flat plate initially normal to flow although their results were expressed as a change in drag coefficient. It is believed that beyond 40 degrees, deviation in the cosine trend is accounted for by changes in drag coefficient due to lift forces similar to an aerodynamic wing. It was concluded that for small angles of incidence, up to 8 degrees, the correction factor can be neglected since the error is less than 1 percent.

Protection of the strain gauges from the high temperature and pressure water environment of LOFT has been solved by mounting them on a beam inside a stainless steel tube as shown in Figure III-32. A model of this device was tested by Detector Development in the flow loop. Because of the increased stiffness, the flow range was 65 to 178 gpm. The strain output was low, as expected, but the log-log plot of output against flow rate was linear with minimum scatter and with a slope of 1.77. A comparison of the results and theoretical calculations based on flow rates of 100 and 160 gpm are shown in Figure III-33. The resonance frequency of the device was measured in air and water and was found to be 680 and 450 Hz, respectively.

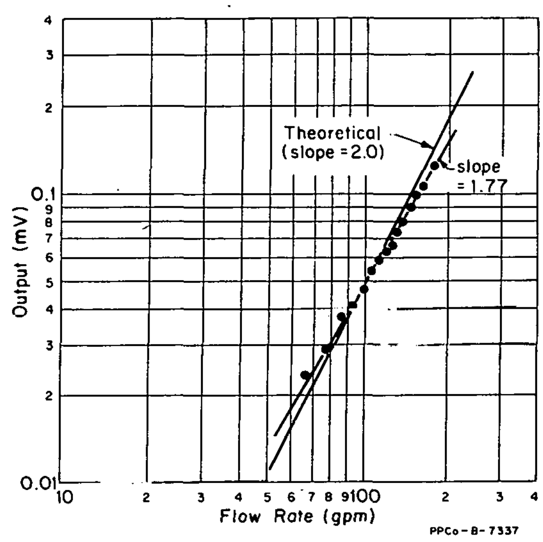

Fig. III-33 Drag disk flow meter output versus flow rate.

A similar drag disk flow meter will be constructed for use in the semiscale blowdown tests. The sizes of the cantilever support tube and beam and the circular disk will be dictated by the expected forces and the location. The type of strain gages and bonding materials to be employed depend on the expected temperature. The applicability of the drag disk flow meter in LOFT with regard to two-phase flow and the expected decompression wave must be determined in the semiscale tests. The drag disks use in liquid flow has already proved acceptable.

## 3. INSTRUMENT COMPONENT AND SYSTEMS DEVELOPMENT

(T. J. Boland)

### 3.1 An Improved Log-Count-Rate Circuit for Determining Beta-to-Alpha in a Constant Air Monitor (K. F. Smith, J. B. Colson)

An improved circuit for measuring the ratio of beta-to-alpha count rates in a constant air monitor has been developed. The previous circuit [5] was found to be difficult to maintain since drift in the vacuum tube voltmeter required continued recalibration. This calibration was made by adjustment of 13 interdependent potentiometers. The new circuit uses solid-state operational amplifiers in place of the vacuum tube voltmeters and has reduced the number of calibration potentiometers to four. These four pots are completely independent of each other, and the calibration may be performed in approximately 20 percent of the time previously required. The operational amplifiers have improved the stability of the system such that repeated recalibration is not required.

The new circuit is shown in Figure III-34. The outputs of the two operational amplifiers are proportional to the log of the alpha count rate and the log of the beta count rate and are used to drive a meter and a recorder for each count rate. The operational amplifier outputs also are subtracted from each other to give a meter and a recorder reading equal to the log of the beta-to-alpha ratio.

The beta and alpha count rates cover a three-decade range from 50 to 50,000 cpm on both the recorder and the beta and alpha meters. The beta-to-alpha ratio covers a four-decade range of 0.01 to 100 on the beta-to-alpha meter and a three-decade range on the recorder. The four potentiometers which are used in the calibration are $R_1$, $R_2$, $R'_1$, and $R'_2$. $R_1$ and $R'_1$ are set to provide the necessary offset for an operational amplifier output of zero volts with 50 cpm into the log integrator. $R_2$ and $R'_2$ are set to give an operational amplifier output of 10 volts with 50,000 cpm input. Since the zero calibration is independent of the gain, the potentiometer adjustments are independent of each other.

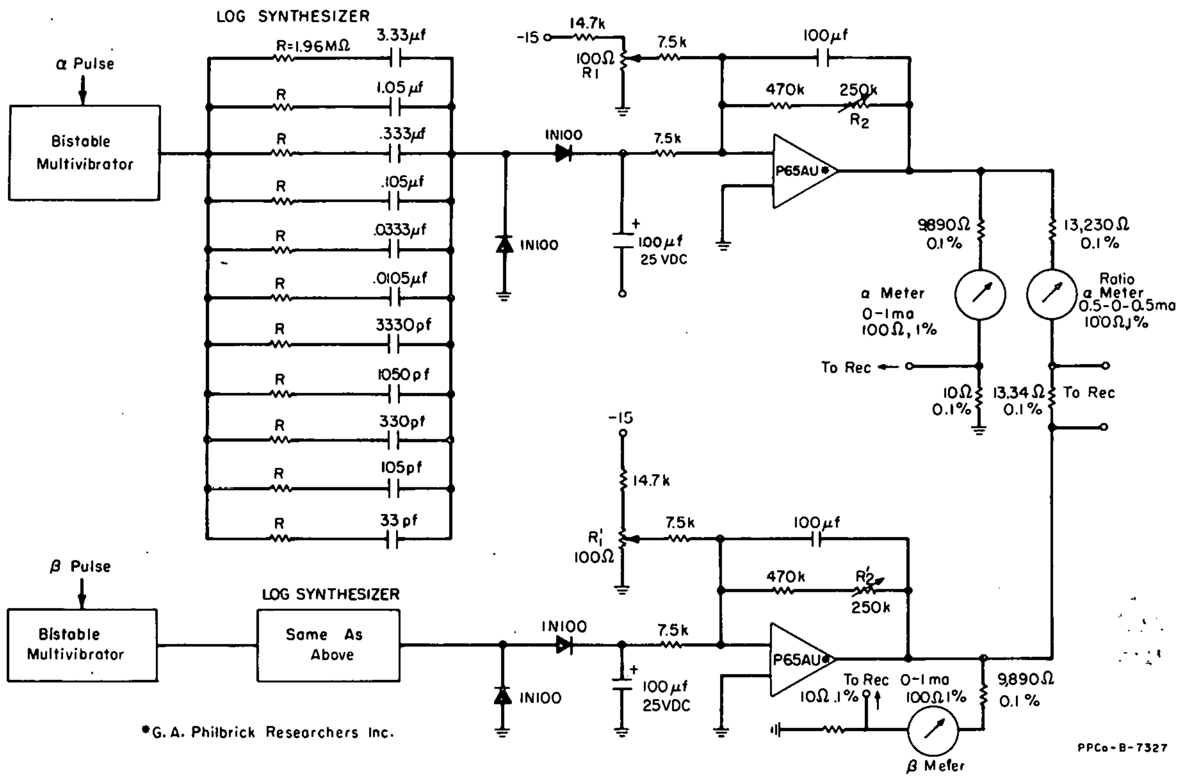

Fig. III-34 Schematic drawing of log-count-rate circuit.

The log circuits are modified versions of the Lichenstein [6] log integrator. Use of precision resistors and capacitors in the log integrators provides a stable, drift-free output which has a linearity of better than one percent of the maximum output. The recorder is a three-point, 0- to 10-mV, potentiometer recorder and is connected across the 10-ohm, 0.1 percent resistors in the output circuit.

### 3.2 Automatic Wire Scanner (C. L. Gibbons, F. A. Meichle)

Nuclear reactor flux levels are measured by positioning small wires in the reactor core lattice. These wires are periodically removed from the reactor, and the induced radioactivity is measured throughout the length of the wire. By placing a number of wires throughout the reactor core, a plot of the vertical and horizontal flux distribution can be obtained from the measurement of the activity induced in the wires.

Because of the large number of wires required to obtain useful mapping of the reactor flux, an automatic wire scanner was designed and constructed. Instrument Development's participation was the design and construction of the control, readout, and electrical drive of the scanner. These functions were integrated into the mechanical portion of the scanner. The automatic wire scanner will provide automatic scanning over a length of 48 inches in adjustable steps of 0.1 inch and adjustable counting time from 0 to 999 seconds in steps of 1 second. The counting scaler has a capacity of 999,999 counts. The counting data is recorded on punched paper tape and/or by a typewriter. The record will contain sample number (0 to 999), count time, elapsed time, counts, wire position, and the proper format on the paper tape for later data processing.

The automatic wire scanner counting and control functions consist basically of a radiation detector and counting unit, controls for positioning and timing, and readout. A block diagram of the scanner is shown in Figure III-35. The crystal detector, photomultiplier, high-voltage power supply, preamplifier, and amplifier are commercial units. The remaining counting, timing, and control units are constructed around commercial solid-state modular logic units.

Scanning is accomplished by clamping the wire in the carriage which is initially in the setup limit. Sample number, count time, and step size are entered into the control unit by means of switches. Actuation of the "clear" switch will normalize all control circuits and reset the scalers. The mode switch is positioned in the "auto" position. The "index" switch is then actuated, and the carriage moves up to the index position. The indexing operation ensures that the carriage always starts from the same position and moves in the same direction in order to eliminate the error due to backlash. Actuation of the "start" switch begins counting of the wire which continues until the selected count time has elapsed. When the counting has stopped, the readout operation begins. After the readout is finished, the carriage will move the preselected distance, stop, and start another count and readout cycle. The count, readout, and positioning cycle will continue until the carriage actuates the end-of-travel limit switch, which again returns the carriage to the setup position, normalizes all control circuits, and resets the scalers. The "scanned" wire is then removed, and the scanner is ready for the next wire.

Additional manual controls are available for manual control of the count scaler, readout, and positioning of the carriage and stop. A stepping motor, which is energized by a pulsed input, is used to drive the carriage. The frequency

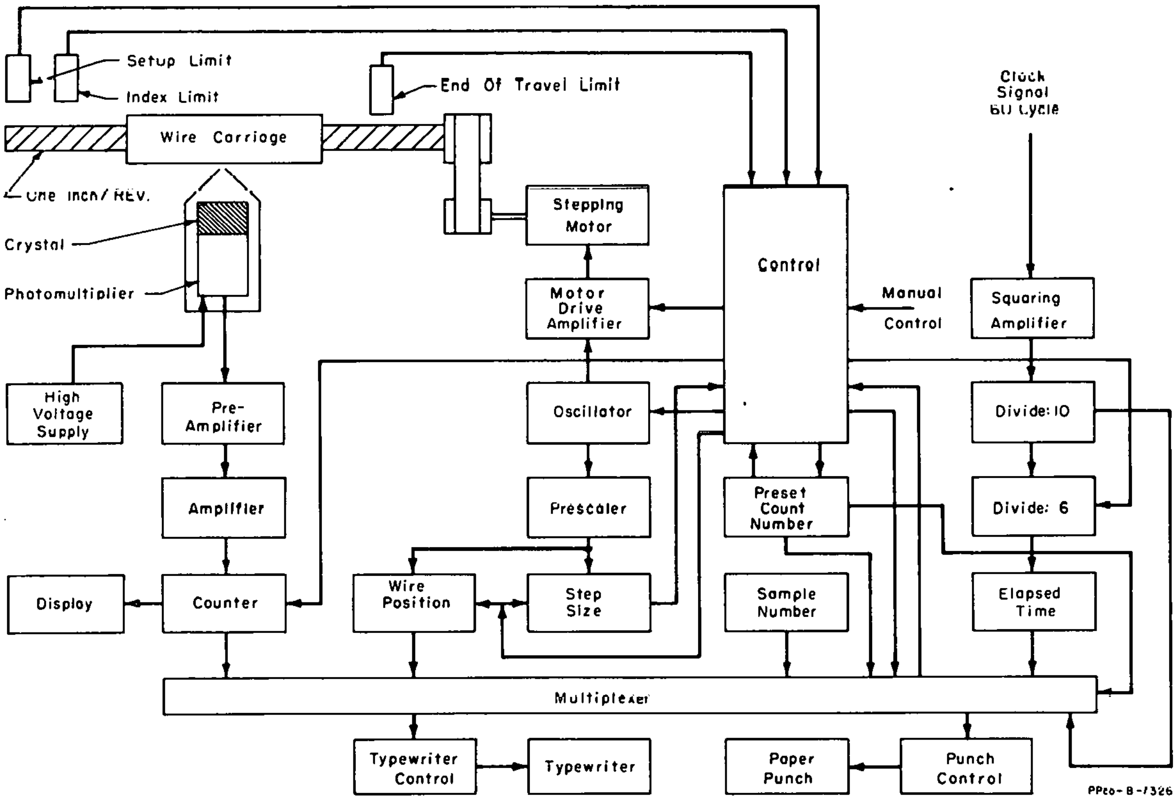

Fig. III-35 Automatic wire scanner.

of the pulses to the motor can be varied by the "rate" control which determines the travel speed of the carriage.

### 3.3 ETR Pneumatic Rabbit Control System (W. Wong, F. A. Meichle)

Irradiation of samples having short half-life requires rapid insertion and removal from the source of radiation. To meet these requirements, a pneumatic sample irradiation facility is being installed in the Engineering Test Reactor (ETR). The facility, shown in Figure III-36, consists of a pneumatic insertion and removal system and a control unit for operating the pneumatic system. The samples are enclosed in plastic capsules (rabbits) which are transported from a cask into the reactor, irradiated for a selected time interval, and then returned to the cask.

Instrument Development was responsible for the design and construction of the control system which was integrated into the pneumatic system. Figure III-37 shows the flow diagram of the control system. The interface between the control system and the pneumatic system is through the use of solenoid-operated valves.

Depressing the "cool" switch turns on the control system. While the system is on and when a capsule is in the reactor, cooling air flows through the reactor test loop. The insertion of a capsule takes about five seconds.

Irradiation time is manually adjustable to 25 hours. Two motor-driven timers provide a timing accuracy of 0.5 percent of full range. One timer

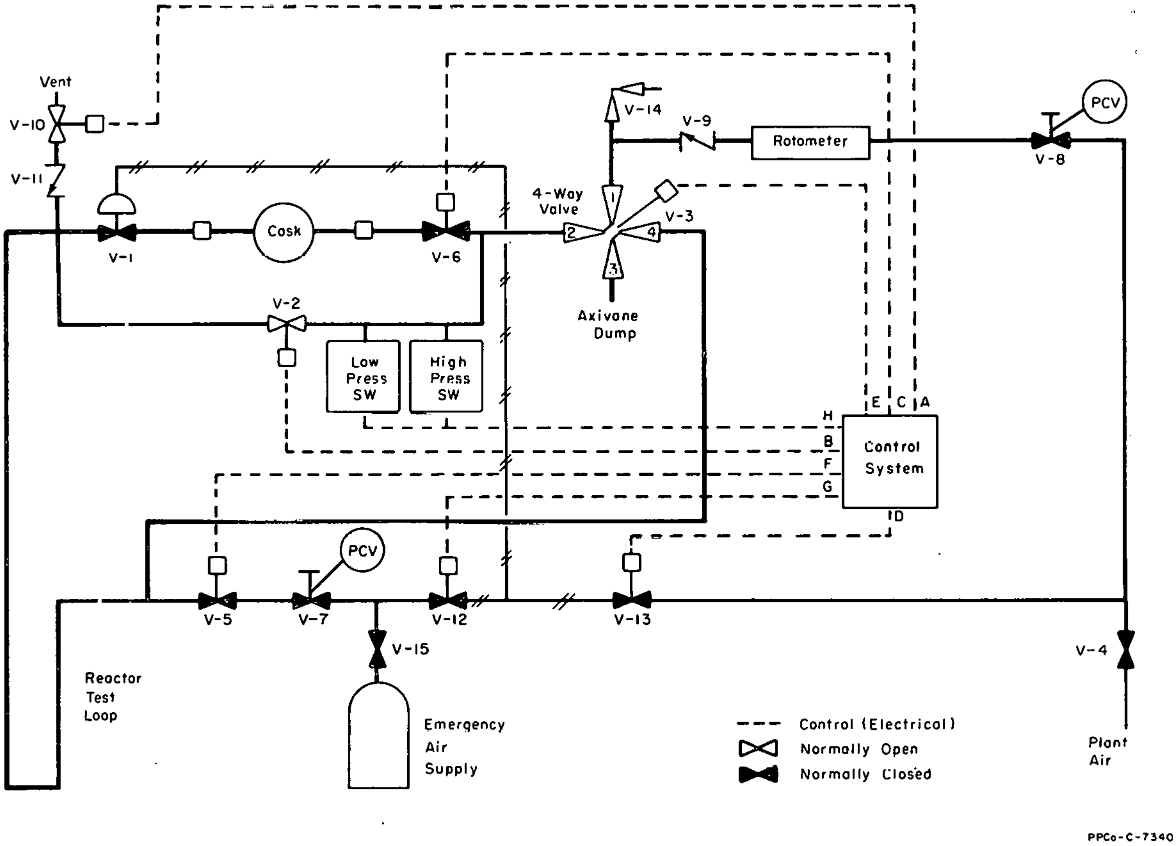

Fig. III-36 ETR pneumatic rabbit facility.

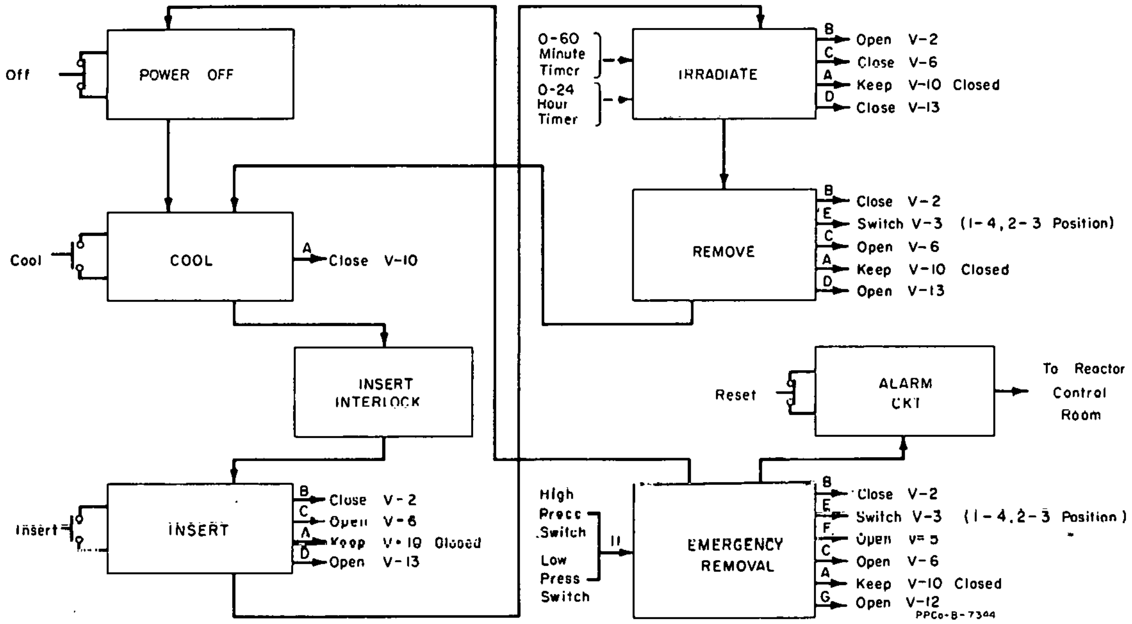

Fig. III-37 Flow diagram of ETR pneumatic rabbit control system.

has a range from 0 to 60 minutes and is used for short irradiation periods of one hour or less. The second timer has a maximum range of 24 hours with 30-minute divisions. The timers are connected so that each timer can be used independently or in combination with the 24-hour timer actuating the 60-minute timer when the former times out. The capsule is automatically removed from the reactor at the completion of the irradiation period.

Electrical interlocks require that at least one timer be preset before capsule insertion can be initiated. Additional interlocks prevent the control system from being inadvertently turned off during insertion, irradiation, or removal of the capsule.

To prevent a capsule meltdown in the reactor due to a loss of plant air, the capsule is automatically removed by means of an emergency air supply. The control system shuts itself off after the emergency removal of the capsule has been completed. Alarm annunciation to indicate abnormal air pressure is provided on the pneumatic rabbit control panel and in the ETR control room. The possibility of capsule meltdown due to electrical power interruption is minimized by connecting the control system to the reactor failure-free power source.

## 4. REFERENCES

1. G. E. McGlothin, "ATR Fuel Plate Deflection Test", MTR-ETR Technical Branches Quarterly Report, October 1 - December 31, 1963, IDO-16977 (1963).

2. H. G. Gibson, W. T. Abel and G. E. Fasching, "Meter for Determining Mass Flow of Solids in Multi-Phase Fluids", N. J. Lipstein (ed.), Multi-Phase Flow Symposium, Philadelphia: The American Society of Mechanical Engineers, (1963) pp 49-54.

3. J. G. Knudsen and D. L. Katz, Fluid Dynamics and Heat Transfer, New York: McGraw-Hill Book Company, Inc., 1958.

4. A. Fage and F. C. Johansen, "Flow of Air Behind an Inclined Flat Plate of Infinite Span", Roy. Soc. Proc., (London), 116A (September 1927) pp 170-197.

5. J. B. Thompson and K. F. Smith, "Alpha-Beta Air Monitor", MTR-ETR Technical Branches Quarterly Report, January 1 - March 31, 1962, IDO-16781 (1962).

6. R. M. Lichenstein, "Random Interchange of Circuits with Applications to Counting Rate Meters and Function Generators", J. Appl. Phys., 28, No. 9 (September 1957) pp 984-989.

# IV. MATHEMATICAL ANALYSIS AND MACHINE COMPUTATIONS

## 1. PERSONNEL REPORTS--PPCO 40.0391

(A. T. Reddish)

The audit of the initial loading of Phillips Petroleum Company Personnel Master Tape has been completed, and all corrections have been made. The COBOL program for changing and updating the file each week is functioning smoothly.

Additional COBOL programs have been written to produce numerous statistical and informational reports for Phillips Petroleum Company and AEC management. These programs are also functioning well and have been combined so as to produce all of the needed reports in only two passes through the personnel master tape. The reports, requested on a monthly basis, are as follows:

(1) AED Technical Report

(2) Monthly Report of Employee Turnover

(3) Monthly Service Report

(4) Monthly Blue Cross Report

(5) Monthly AEC Report of Contract Placement

(6) Personnel Branch Progress Report

(7) Monthly Benefit Reports

(8) Fund C Participating Report.

## 2. INTERNAL SORT SUBROUTINE, SORT--PPCO 40.0574

(Stephen E. Nugent)

This is a general subroutine which will sort blocks of information internally in the 7040. The subroutine may be called from MAP, COBOL, or FORTRAN. These blocks may be of any specified length, and there may be as many of these blocks as the user desires. The user can specify any word within the blocks as the sort control word, that is, the word on which the blocks of information are to be sorted. The user can specify whether this word contains BCD or binary information. Sorting may be done in either ascending or descending order. Presently this routine uses only the 7040 machine collating sequence.

## 3. CALCULATION OF STANDARD DEVIATION AND MEAN VALUE--PPCO 40.0502

(Dennis Speas)

This program was written specifically for analyzing data collected at the ETRC facility, but effort was made to keep it general in application. Several items are computed using each data point. Then the data values may be grouped into subgroups after which the calculation is repeated, treating the average value of each subgroup as an individual data point. The following items are part of the output: number of points per average, total number of points, mean value, standard deviation, percent standard deviation, sum of all points, sum of squares of all points, maximum value, and minimum value. Options are available for printed lists or plots of the data values.

## 4. MA AND MC BRANCH PROGRAMS CATALOG--PPCO 40.0445

(G. A. Jayne)

Using input cards punched from the SHARE PROGRAM CATALOG form, program CACOFONY keeps an updated, SHARE-compatible catalog of the Mathematical Analysis and Machine Computations Branch IBM 7040 computer programs.

Updating of this master tape allows the omitting of records, the addition of new records, and the altering and omitting of portions of any given record. (A record here refers to an abstract of one program.)

From the master tape can be obtained five listings:

(1) Complete abstracts in order of ascending program number and installation code

(2) One line entries, in the same order as (1)

(3) Printout of input, by author, for editing purposes

(4) Keyword index

(5) Abbreviated abstract listing.

## 5. COMPUTATION OF POTENTIAL RADIOLOGICAL HAZARDS FROM REACTOR ACCIDENTS--PPCO 40.0075

(R. L. Coates, N. R. Horton)

The selection of sites for nuclear power plants, as well as the design of the plants themselves, must take into consideration the radiological hazards which could exist in the event of a nuclear accident. The doses, resulting from such an accident, can be estimated by hand calculational techniques. However, if a rigorous mathematical analysis is desired, it is necessary to resort to the capabilities offered by a computer. To provide the degree of flexibility required for a complete parametric study of the radiological hazards, Phillips Petroleum Company has developed an IBM 7040 computer program which is divided into the five major categories:

(1) Curie -- calculates the fission product inventory for any set of operating conditions

(2) Fractionation and Release -- applies the desired fractionation to Curie and releases the radioactive materials to the atmosphere

(3) Inhalation -- calculates the inhalation dose to eight critical organs

(4) Cloud Gamma -- calculates the external dose received as a consequence of exposure to airborne radioactive materials

(5) Deposition Gamma -- calculates the external dose received as a consequence of exposure to deposited fission products.

## 5.1 Curie

The first category of the RSAC program deals with the calculation of the fission product inventory. This inventory can be determined for any combination of the following operating conditions:

(1) Steady-state operation -- reactor operation at a given power level for a sustained period of time.

(2) Transient operation -- reactor operation at a given power level for a short period of time.

(3) Cyclic operation -- reactor operation at a given power level for a given period of time, followed by a specified shutdown period which is subsequently followed by another transient or steady-state operating history. This type of operation can be repeated as many times as desired.

(4) Refueling -- refueling is simulated by removal of a certain fraction of the fission product inventory which may have been generated by any of the above three types of operating histories. Following the refueling process, a new inventory can be calculated which will be based upon the inventory remaining after refueling as well as the inventory generated by a new set of operating conditions.

The method used to determine the fission product inventory is based upon a simple parent-daughter decay scheme as formulated by Rubinson[1]. The RSAC program, as presently coded, determines the inventory for 90 decay chains with a maximum of 5 isotopes per chain.

The data required for the calculation and print-out of the fission product inventory are as follows:

(1) Atomic number of isotopes considered

(2) Atomic weight of isotopes considered

(3) Half-life of isotopes considered

(4) Symbol and units of half-life

(5) Fission yield of isotopes considered

(6) Operating history

(7) Element group

  (a) Noble gases

  (b) Halogens

  (c) Cesiums

  (d) Solids.

Numerical values and symbols for the first five groups (atomic number through fission yield) were obtained from References 2, 3, 4, and 5.

## 5.2 Fractionation and Release

The second category of the RSAC program deals with the fractionation and release of the fission products generated under Category (1). The purpose of fractionating the fission products into four different groups is to allow for different removal mechanisms, such as washout, plateout, fallout, etc, which may occur during the transport of the fission products to the containment shell and ultimately to the atmosphere. Three ways by which the RSAC program can fractionate the inventory are as follows:

(1) Fractionate a certain percentage of the total fission product inventory

(2) Fractionate by element group

  (a) A percent of the noble gases

  (b) B percent of the halogens

  (c) C percent of cesiums

  (d) D percent of the solids

(3) Fractionate by individual elements up to a maximum of 20 elements and fractionate the remaining inventory by a specified percentage.

The second phase of the fractionation and release category is concerned with the release of the fractionated fission products to the atmosphere. This release can occur as an instantaneous release or as a continuous release. For both the continuous and instantaneous release, the basic continuous point-source diffusion equation, as formulated by Sutton, is used in calculating the airborne activity.

Sutton's basic equation has been modified to account for cloud depletion due to fallout or rainout, fission product fractionation, decay or buildup of the source term, and also for a decreasing or increasing leakage-rate function.

Cloud depletion due to fallout or rainout is based upon Chamberlain's mathematical model[6] which has been included as part of the standard data deck.

Allowance for a variable leakage rate is provided in the RSAC program. This leakage rate is expressed as a series of exponential approximation for which up to 10 approximations can be used.

The meteorological parameters needed for the diffusion and cloud depletion equations and those parameters which are entered as input variables are as follows:

(1) The average wind velocity in meters per sec

(2) The stack height or height of release in meters

(3) The horizontal and vertical diffusion coefficients in meters$^{(N/2)}$

(4) The horizontal and vertical stability parameters

(5) The deposition velocities for each of the four-element groups in meters per sec.

### 5.3 Inhalation

The third category of the RSAC program is concerned with the calculation of the internal or inhalation dose. This dose, which is received as a consequence of inhaling airborne radioactive materials, is determined for eight critical organs, which are:

(1) Bone -- 48 contributing isotopes

(2) Kidney -- 39 contributing isotopes

(3) Liver -- 42 contributing isotopes

(4) Lung -- 58 contributing isotopes

(5) Muscle -- 5 contributing isotopes

(6) Testes -- 7 contributing isotopes

(7) Thyroid gland -- 15 contributing isotopes

(8) Total body -- 58 contributing isotopes.

The method for calculating the above inhalation doses essentially consists of two steps:

(1) Determine the concentration of radioactive materials in a particular organ as a function of inhalation and exposure time.

(2) Integrate the concentration function to determine the total number of disintegrations which have occurred. After the total number of disintegrations has been calculated, the inhalation dose is determined by applying an appropriate conversion factor to convert disintegrations to dose.

The types of output which can be obtained from the inhalation dose calculation are the following:

(1) The total dose from all elements to each organ for each downwind and crosswind detector position

(2) The contribution from each element for each downwind detector positions as well as the total dose at that position from all contributing elements

(3) The contribution from each element for each downwind and crosswind detector position as well as the total dose from all contributing elements at that position.

## 5.4 Cloud Gamma

The fourth category of the RSAC program is concerned with the calculation of the cloud gamma dose which is received as a consequence of exposure to airborne radioactive materials.

The method of calculating the cloud gamma dose is as follows:

(1) Determine the concentration function of an incremental volume of the airborne materials and then perform the necessary integration to determine the total number of disintegrations which have occurred within the incremental volume

(2) Calculate a radius vector from the incremental volume to the detector position and determine the dose contribution from that volume of cloud

(3) Perform the necessary integrations over the entire cloud to determine the total gamma dose at a given downwind and crosswind detector position.

Due to the large number of isotopes and gamma energies considered, it has been found necessary to group the energies into 10 distinct gamma energy groups. The gamma energy range covered by the 10 groups is 0 to 6 MeV.

## 5.5 Deposition Gamma

The fifth and final category in the RSAC program deals with the determination of the deposition gamma dose which is received as a consequence of exposure to deposited fission products. The deposition gamma dose in concerned primarily with the dose contributions from the halogens and solids; therefore, the capabilities for entering different deposition velocities for these elements are provided in the program.

The method of calculating the deposition gamma dose is as follows:

(1) Determine the concentration of radioactive materials on the ground as a function of deposition and decay time

(2) Follow the same procedure as in the cloud gamma dose calculations except perform the integration over the horizontal plane only.

## 6. REFERENCES

1. W. Rubinson, "The Equations of Radioactive Transformation in a Neutron Flux", J. Chem. Phys., 17 (June 1949) pp 542-7.
2. S. Katcoff, "Fission-Product Yields from Neutron-Induced Fission", Nucleonics, 18 No. 11 (November 1960) pp 201-8.
3. J. O. Blomeke and M. F. Todd, "Uranium-235 Fission-Product Production as a Function of Thermal Neutron Flux, Irradiation Time, and Decay Time. 1. Atomic Concentrations and Gross Totals, ORNL-2127 (Pt. I, Vol. 1) (August 1957).
4. J. F. Perkins and R. W. King, "Energy Release From the Decay of Fission Products", Nucl. Sci. Eng., 3 (June 1958) pp 726-46.
5. G. P. Kenfield et al, Curie-Dose-Thunderhead -- A Digital Computer Program for External and Internal Radiation Dose Calculations, NAA-SR-8884 (June 1965).
6. A. C. Chamberlain, Aspects of Travel and Deposition of Aerosol and Vapour Clouds, AERE-HP/R-1261 (September 1953).

PHILLIPS
PETROLEUM
COMPANY

ATOMIC ENERGY DIVISION